Topographic Constraints on Rotating Stratified Throughflows Across Large Amplitude Topography

Miguel Angel Jiménez-Urias

A dissertation
submitted in partial fulfillment of the
requirements for the degree of

Doctor of Philosophy

University of Washington

2019

Reading Committee:

Luanne Thompson, Chair

Peter Rhines

Charles Eriksen

Program Authorized to Offer Degree:
School of Oceanography

University of Washington

Abstract

Topographic Constraints on Rotating Stratified Throughflows Across Large Amplitude Topography

Miguel Angel Jiménez-Urias

Chair of the Supervisory Committee:
Professor Luanne Thompson
School of Oceanography

The Atlantic inflow of warm saline waters that flow into the Nordic Seas is strongly steered by the Greenland-Scotland Ridge (GSR). Such flow is associated with the lateral exchange of watermasses between the North Atlantic and the Arctic Mediterranean and is part of the large scale overturning circulation of the ocean. This thesis examines, through the use of idealized, process-based modelling, aspects of the topographically locked Atlantic inflow that flows across the Iceland-Faroe Ridge, the widest and shallowest gap of the GSR.

The effects of bottom topography on the instability, eddy-driven heat flux and overturning of a topographically locked top to bottom front is examined in Chapter 2. Central to this study is that the surface expression of the front presents lateral shear within the mixed layer, typical of wintertime conditions. We find the initial growth of surface mixed layer eddies is insensitive to topographic variations but during the finite amplitude phase of mixed layer instability, we find faster development of mesoscale eddies and stronger cross-front eddy heat flux in the cases where the frontal jet experiences the most destabilizing bottom topography of the three cases tested, with values comparable to the heat flux associated with the mean flow. Therefore, eddy dynamics over the IFR frontal region are important contributors to the heat exchanges between the North Atlantic and Nordic Seas, with bottom the topography playing a key role in determining the largest heat fluxes, whether the initial growth is dominated by

mixed layer eddies, or mesoscale eddies.

Chapter 3 examines the leading order balance that determine the transport pathways associated with throughflows across a symmetric, large amplitude ridge. The equilibrated circulation across the ridge is characterized by an anticyclonic boundary current associated with northward upslope transport and a cyclonic boundary current associated with northward downslope transport, with a strong near bottom stratification associated with the anticyclonic boundary current and low stratification associated with the cyclonic boundary current. Such along-stream stratification implies a nearly the northward upslope transport experiences little resistance by the ridge, and a cyclonic boundary current that requires a stronger inertial recirculation to promote downslope northward transport. The observed difference in baroclinic behavior across the ridge crest may explain the preferred cyclonic circulation and strong along-slope topographic steering experienced by Atlantic waters as they flow north of the Greenland Scotland Ridge.

Chapter 4 examines the baroclinic structure of throughflows across a finite amplitude ridge. We find that bottom Ekman dynamics localized to lateral boundary currents restratify the bottom boundary layer, resulting is strongly stratified front (thus a high PV anomaly) along the anticyclonic boundary current, and a low stratified (vanishingly low PV) mixed layer front localized to the cyclonic boundary current. These PV anomalies are advected by both the mean flow and eddies that result from baroclinic instability of the mean flow, resulting in a spatial distribution where high PV is concentrated along the ridge, and low PV is advected into the interior, mid depth ocean downstream from the ridge. Using a framework of volume integrated PV conservation which incorporates the net fluxes associated with bottom topography we conform this approximate integral balance between the injection of low PV from the bottom boundary layer downstream from the ridge and net advective across the ridge. Implications of these findings for understanding the interplay between large scale and bottom boundary dynamics are discussed.

TABLE OF CONTENTS

LIST OF FIGURES

ACKNOWLEDGMENTS

The author wishes to express sincere appreciation to the School of Oceanography, and the department of Applied Mathematics, where he started his graduate education as a Masters student. Graduate school was a place for deep learning, creative thinking, life lessons, with many great teachers and mentors. To my advisor Prof. Luanne Thompson, an amazing scientist, a detailed reviewer and persistent encourager. You gave me the freedom to find my path along the ups and downs of the PhD marathon. Thank you for constantly having faith in me. In addition, I would like to express my deepest gratitude to Prof. Peter Rhines and the Geophysical Fluid Dynamics Laboratory (GFDLab), a place for constant teaching and learning, where the *math became alive*, and where many of the ideas for this thesis were *spun up*-ed, and subsequently *adjusted* thanks to *unbalanced* secondary overturning circulations.

Sincere appreciation to all my colleagues within the University of Washington. Many shared lessons and personal growth late nights at College Inn, the *First Fridays* first as an outsider and later as an organizer. A great appreciation for the 2012 ocean cohort *oceans eleven*, as well as the cohorts above and below with whom I had the pleasure to share a moment, a drink or a friendship. Thanks to Zoka Coffee Roasters and Cafe Solstice for providing the required caffeine to do basic science. Special gratitude to the *Latona Founding Fathers*: Mauricio Del Razo Sarmina, Daniel McCoy, Rodrigo Solinis-Casparius, Daniel Shapero and of course Sappho. I could not have asked for better housemates throughout the years. To the later *Latona Family* members James Kessler, Gabriel Seufitelli and Danielle Pascoli, thank you also. You guys made living in Seattle much easier. To the *Seattle Fandango Project*, for giving me a family away from home, and lastly, to Ms. James Kessler and family, for their constant support through this endevour.

DEDICATION

A mis padres y hermanos por darme todo lo pude pedir, una infancia humilde y llena de felicidad y a mis sobrin@s, por dejarme ser uno de ellos.

Chapter 1

INTRODUCTION

Large scale differential solar heating on the surface of the Earth sets up a large scale overturning circulation of the Earth's atmosphere and oceans. Due to continental boundaries and rotational effects on the ocean at planetary scales ($L \sim O(1000)$km), deep convection and watermass transformation in the oceans takes place only at a handful of locations where the upper ocean stratification is preconditioned for deep convection as it experiences atmospheric (wintertime) surface cooling (*e.g.* a layer of salty warm water above a layer of relatively fresher colder water). Given the small aspect ratio of the ocean at planetary scales $H/L \ll 1$ where $H \approx 6km$, planetary scale convection is characterized by localized downwelling that sets up a broad, planetary scale (nearly) horizontal flow. The Nordic seas, one of a handful of locations where deep convection occurs, represents a unique site given that the Greenland-Scotland Ridge (GSR), a large-scale large amplitude topography, greatly constrains the lateral exchange of watermasses between subpolar North Atlantic and the nordic basins (Fig.1.1). There, a local modification of horizontal flows by mesoscale ($L \sim O(10-100)$km) or submesoscale ($L \sim O(1-10)$km) processes, as Atlantic waters navigate across the shallow waters of the GSR, can exert a control on the patterns of deep convection and watermass transformation.

This thesis addresses the question of how a throughflow, the flow that connects ocean conditions across a sill or a strait, can be locally modified as it navigates large amplitude topography, through the use of idealized, process-based models that represent distinct features of the flow of Atlantic waters across the Iceland-Faroe Ridge (IFR), the widest and shallower gap of the GSR.

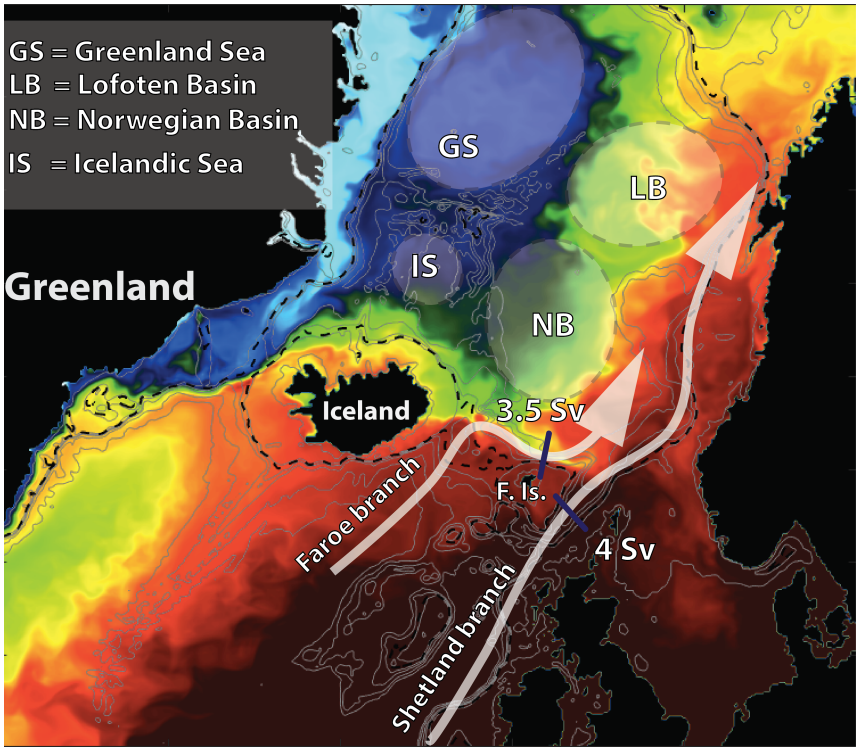

Figure 1.1: Surface potential temperature (warm is red) at a depth 250m below the surface. White arrows show the pattern of circulation of the Atlantic inflow into the Arctic Mediterranean by the two main branches: The Faroe branch and the Shetland branch. The 500m isobath is represented by dashed black contours. The upper 2000m isobaths are shown every 200m the upper 1000m, and then at every 500m. Also shown are the convective sites (interior ocean basins) where Atlantic water is transformed by destabilizing surface forcing. Data used from POPv2, a global ocean model with horizontal resolution of 0.10°Lat and monthly output [Small et al., 2014]

This thesis considers two different idealized models. First, an initial value problem of a top-to bottom temperature front that resembles recent observations of the temperature distribution of temperature and zonal (along-slope) velocity [Beaird et al., 2016]. The Atlantic inflow is modeled as a zonally symmetric (re-entrant) baroclinic current, and the meridional exchange is through surface intensified baroclinic eddies and bottom Ekman transport. The second approach is that of channel model where the Atlantic inflow across the IFR is represented by a source-sink driven throughflow across a symmetric ridge that intersect

topography. The objective is to analyze the along-stream modification of the equilibrated, continuously stratified flows across large amplitude topography, which leads to a change in character of the baroclinicity of the current and has the potential to exert a control downstream, given that the flow must balance large scale constraints associated with the conservation of mass, energy, momentum and potential vorticity.

In the second approach, the throughflow represents the topographically steered component of the Atlantic inflow that flows across the IFR. While lacking the sub-surface frontal expression of the Iceland-Faroe Front, maintained by a combination of the topographic steeering of the Atlantic inflow and the confluence of Atlantic waters with the East Icelandic Current, the equilibrated throughflow is able to reproduce basic features for the Atlantic inflow as it navigates the IFR: A standing anticyclonic meander atop the ridge crest that results in upwelling of cold deep overflow waters from south of the ridge crest [Prater and Rossby, 2005], and, lastly, that the Atlantic inflow downstream from the ridge becomes greatly topographically steered, an apparent change on the baroclinic structure of the flow after navigating across the GSR.

1.1 Atlantic Water through the Greenland-Scotland Ridge

The Atlantic inflow carries roughly 8.5 Sv (1Sv=$10^6 m^3 s^{-1}$) of warm and saltier waters into the Nordic Seas, corresponding to about 90% of the total volume flux into the region [Dickson et al., 2008, Rossby and Flagg, 2012], while the rest is supplied by freshwater flux from runoff and precipitation at a rate of 0.2 Sv [Aagaard and Carmack, 1989], and 0.8 Sv through the Bering Strait [Coachman and Aagaard, 1988, Roach et al., 1995], leading to an estimated import of 310 TW (1 TW=10^{12} W) of heat (relative to 0°C)[Hansen et al., 2008, Rhines et al., 2008]. The GSR reaches above the surface at Iceland and again at the Faroe Islands, splitting the Ridge into three gaps: The Denmark Strait, with a maximum depth of 620m, the Iceland-Faroe Ridge (IFR) with a depth around 400-500m and lastly, the Faroe-Shetland Channel (east of the Faroe Islands) with a maximum depth of 840m at the Faroe Bank Channel (Figure 2). As a result, the inflow bifurcates into three branches: The Icelandic

branch, that crosses the GRS to the west of Iceland, the Faroe branch that flows through the IFR, and lastly the Shetland Branch that flows through the Faroe-Shetland Channel (Fig. 1.1). From all the Atlantic inflow branches into the Nordic Seas, for which estimates indicate it supplies no less that 50% of its waters directly to overflow water formation ([Hansen et al., 2008] estimates up to 71%), the Atlantic inflow flowing through the IFR is considered to be the greatest contributor of Atlantic waters that leads directly to the formation of overflow waters [Hansen et al., 2008], and responsible for the greatest *net* heat flux into the Nordic Seas [Rossby and Flagg, 2012].

The Atlantic inflow crosses the IFR generally as a broad flow along its entire length ($\sim$ 300km), and through almost all of the depth of the water column [Jakobsen et al., 2003, Rossby et al., 2009, Hansen et al., 2010] (Figure 3). The warm Atlantic water adopts an anticyclonic meandering pathway feeding the Faroe Current, which is a response to the steep topography, both from vortex squashing as it encounters the ridge, and in feeding the cyclonic boundary current system of the Nordic Seas [Beaird et al., 2016]. There are, however, two main dominant pathways for Atlantic water to cross the IFR: A pathway close to Iceland and a broader *fast track* pathway, possibly stronger, that lies closer to the Faroe Shelf and most likely associated to a cyclonic Faroe-shelf circulation [Maskell et al., 1992, Rossby and Flagg, 2012]. The branch closer to Iceland feeds the topographically locked, top to bottom Iceland-Faroe Front (IFF) that modulates the exchange between Nordic and Atlantic waters, concentrating much of the inflow along a narrow region $O \sim (100)km$ [Allen et al., 1994, Maskell et al., 1992, Beaird et al., 2013]. Thus, frontal processes such as eddy stirring, as well as surface forcing that can lead to dissipation and watermass transformation, can lead to a local modification of the density structure. The eventual fate of the waters above the IFR is northwards, given the strongly barotropic Atlantic inflow. But changes of the stratification, dissipation, as well as the presence of eddy variability can lead to a modification and preconditioning of the downstream behavior on the Nordic Seas [Beaird et al., 2016].

1.2 Seasonality of the Stability of the Iceland-Faroe Front

Away from the influence by coastal shelfbreaks, the Atlantic inflow is nearly parallel to f/H contours, and has a vertical density frontal structure that outcrops to the north of the ridge crest, and extends to the south of the IFR crest, where the isopycnals run parallel to the sloping topography. During winter, recent observations show an additional watermass that results from freshwater intrusions associated with mixed layer water from the Nordic Sea side of the front. These anomalies extend across the IFR crest, likely the result of the combined action of the convective homogenization of the front that deepens the mixed layer, and subduction by baroclinic instability [Beaird et al., 2016]. Thus, there are two possible mechanisms that promote eddy-driven exchange across the IFF. The first is owing to classic mesoscale baroclinic instability ($L \sim O(10-100)km$) whenever mixed layers are shallow, typical of summer conditions. The second when baroclinic instability within the mixed layer is at work, when sufficiently deep mixed layers also have strong horizontal density gradients.

The evolution of baroclinic instability associated with quasigeostrophic flows, describes mesoscale flows with typical lengthscales $L \sim (10-100)$km that grow at typical advective timescales $t \sim O(L/U)$[Pedlosky, 2013a], and where bottom sloping topography can modify the instability depending on the ratio between (frontal) isopycnal slopes to topographic slopes. Given the frontal structure of the IFF with respect to sloping bottom, the sloping IFR south of the ridge provides a stabillizing effects on the near bottom flow, while the north side of the IFR has a frontal structure that is always unstable to mesoscale baroclinilc instability.

At the submesoscales, characterized by length scales $L \sim O(1-10)km$ the timescale of the instability is $t \sim O(f^{-1})$, and the instability departs greatly from the mesocale case, being confined within a mixed layer front with vanishingly small vertical stratification and a lateral density gradient that is in thermal wind balance, such that $N^2_{ML} \sim S^4_{ML}/f^2$, or in terms of non-dimensional parameters

$$Ri_{_{ML}} = \frac{N^2_{_{ML}} f^2}{S^4_{_{ML}}} \sim O(1) \tag{1.1}$$

where $N^2_{_{ML}} = g\alpha T_z$ and $S^2_{_{ML}} = -g\alpha T_y$ represent the vertical and lateral stratification within the mixed layer.

In chapter 2 we investigating different frontal configurations that incorporate both mesoscale and mixed layer frontal instabilities, in which the frontal isopycnal of the IFF, experiences different stabilizing effects by the sloping bottom topography. While we observe that in the linear development, mixed layer eddies do dominate the eddy growth and are insensitive to bottom topography slopes, during nonlinear eddy growth, eddies associated with the most unstable topographic slopes promote stronger meridional heat fluxes within an advective timescale typical of a watermass navigating the extent of the IFR.

1.3 Throughflows Across Large Amplitude Topography

Throughflows are usually represented by narrow channels with uniform potential vorticity, such that Kelvin wave dynamics determine the pressure field [Gill, 1976, Pratt, 1983, 1984, Whitehead, 1995], thus neglecting Rossby wave dynamics that can significantly change the pressure field and flow pattern beyond that determined by Kelvin waves [Hermann et al., 1989].

Under a *wide* channel geometry where the cross-sectional width of the channel is much greater than the deformation radius, an equilibrated flow in the f-plane that forced by up-stream and downstream lateral inflow/outflow conditions, will reflect the influence of topographic Rossby waves given the absence of β-plane dynamics and surface wind stress. Under such assumptions, the throughflow will be characterized by a bottom intensified anticyclonic boundary current upstream of the ridge crest where topography slopes upward, and a bottom intensified cyclonic boundary current downstream from the ridge crest, where topography slopes downward. Boundary currents provide a required torque (recirculation) that promote flow up the slope.

The leading order scale analysis associated with mean transport across a slope, derived in chapter 3, is

$$\frac{Qf}{H} \sim \frac{A_{_H} U}{L} \tag{1.2}$$

where Q is the cross slope transport, H depth, f uniform Coriolis parameter, $A_{_H}$ represents dissipation by a boundary current and U/L the cross-stream relative vorticity. Thus, (1.2) implies that a reduction of H (shallow water) while keeping the transport constant, implies an increase in the relative vorticity $Ro = U/L$ of the mean flow, with $A_{_H}$ fixed. If the relative vorticity is fixed instead, then dissipation of momentum must increase, by a thicknenning of a boundary layer. The mean flow can then become unstable to hydrodynamic instabilities even for relatively small Ro values. In the limit $Ro \sim O(1)$ dynamics within the bottom boundary layer have the potential to induce rapid re(de)-stratification of the interior flow outside the bottom boundary layer [MacCready, 1994, Benthuysen and Thomas, 2012] and thus exert a control on the mean circulation, given that the throughflow must still conserve global constrains on mass, momentum and circulation.

In chapter 3 we look at the localized modification of the troughflow by bottom Ekman transport that result in asymmetry on the torque across the ridge crest, an asymmetry on the horizontal (barotropic) behavior of the circulation across ridge topography.

Chapter 4 examines the vertical structure (*i.e.* the potential vorticity of the flow) of the throughflow across the ridge, and the modification of the vertical structure (pv) of the flow downstream due to the asymmetries on the stratification associated with boundary currents and bottom Ekman dynamics.

Chapter 2

IDEALIZED STUDY ON THE EFFECT OF BOTTOM TOPOGRAPHY ON THE SEASONALITY OF THE STABILITY OF THE ICELAND-FAROE FRONT

2.1 Introduction

The Greenland-Scotland Ridge mediates the exchange of water between the warm and salty subpolar North Atlantic and the cold and relatively fresh Nordic Seas. About half of the total Atlantic inflow into the Nordic Seas takes place between Iceland and the Færæ Islands [Hansen et al., 2008], where it flows mostly along topographic contours and is associated with the surface to bottom Iceland-Færæ Front (IFF) [Hansen and Meincke, 1979]. The front outcrops to the north of the Iceland-Færæ Ridge (IFR) crest, the Nordic flank, and provides a pathway for warm and salty Atlantic water to flow along the ridge (Fig.2.1). This water then feeds the Færæ *Current*, a major branch of the Atlantic inflow that contributes to preconditioning the Nordic Seas for deep convection and the formation of deep overflows, the deepest branch of the Atlantic Meridional Overturning Circulation Quadfasel and Käse [2013]. The front extends to the south of the IFR crest, the Atlantic flank, where the frontal isopycnals approach the bottom running parallel to the sloping topography. There, the gently sloping isopycnals are maintained by the along-slope gravity current originated from the deep overflow from the Faroe-Bank Channel overflow and fed by intermittent cross-IFR overflow [Beaird et al., 2013].

On the Nordic flank of the IFR, away from the Icelandic and Færæ shelves, the mean location of the Iceland-Færæ Front (IFF) is largely constrained by the convergence of the North Atlantic Current with the East Icelandic Current, and by the strong topographic steering, despite the presence of strong eddy variability [Hansen and Meincke, 1979, Fox and

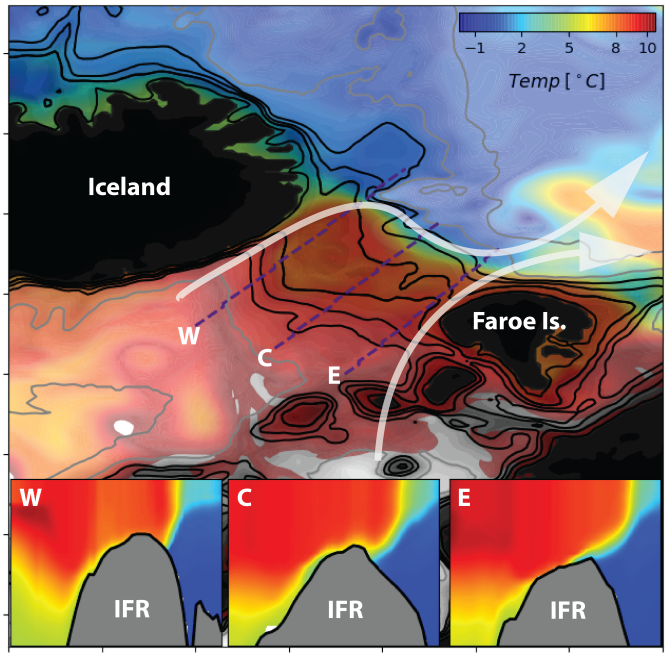

Figure 2.1: Potential temperature at a depth of 200m from a muti-year, global ocean simulation with 0.10° horizontal resolution [Small et al., 2014]. White arrows represents surface (Atlantic water) pathways of the mean flow into the Nordic Seas across the IFR. The mostly along-ridge isotherms promote an along-ridge geostrophic flow into the Nordic Seas. Dark contours represents topographic contours every 100m until 1000m, and then every 500m until a depth of 2500 m. W, C and E represent the location of across-ridge sections, each displayed at the bottom of the figure.

Maskell, 1996]. The IFF strongly meanders, shedding both cold and warm core eddies that are associated with the nonlinear stages of baroclinic instability [Allen et al., 1994, Miller et al., 1995]. The IFF is composed largely of two watermasses during summertime, when the majority of the historical observational sampling have taken place [Rossby and Flagg, 2012]: The warm and salty Atlantic water lies atop the front with the colder and relatively fresher Nordic sea water lying underneath. During winter, recent observations show an additional watermass that results from freshwater intrusions associated with mixed layer water from the Nordic Sea side of the front. These anomalies extend across the IFR crest, likely the result of the combined action of the convective homogenization of the front that deepens

the mixed layer, and subduction by baroclinic instability [Beaird et al., 2016]. Thus, there are two possible mechanisms that promote eddy-driven exchange across the IFF. The first is owing to classic mesoscale baroclinic instability whenever mixed layers are shallow, typical of summer conditions. The second when baroclinic instability within the mixed layer is at work, when sufficiently deep mixed layers also have strong horizontal density gradients.

Theoretical arguments suggest that when present, MLEs dominate the initial growth and thus the later nonlinear stages as well [Callies et al., 2016]. However, the behavior of MLEs in the presence of destabilizing bottom topography, both in the linear and nonlinear phases of MLE instability is unclear. This is important for the topographically locked IFF in which along-front variations of topography, the front slopes steeper towards Iceland than it does towards the Faroes [Maskell et al., 1992], may determine localized regions where destabilizing effects on mesoscale instability are greatly enhanced and as a result, can determine complex pathways for eddy-driven exchange and spread of watermasses across the frontal region.

In this study we examine the evolution of the instability of an idealized representation of the Iceland-Færæ Front that reproduces the basic observed features of the region with different representations of the surface front in summer and winter. We build on previous studies of baroclinic instability of ocean fronts in the presence of bottom topography by including a mixed layer front in the presence of variable topography, barotropic shear, and a continuous cross-ridge frontal structure. The paper is organized as follows: first we introduce the theoretical framework used within our study, namely classical results from linear baroclinic instability such as ageostrophic and topographic effects in the growth of unstable wave modes. Then we provide a description of the model and describe the two sets of experiments that focus on the seasonality of the stability. We examine topographic effects on the initial growth of the instability associated with each experiment and identify the dominant mechanism of the instability. We then examine the resulting eddy-driven overturning for two contrasting initial configurations of the front, and finally we discuss the implications for seasonality of eddy-driven exchange across the Iceland-Færæ Front.

2.2 Theoretical Framework

The classical theory that describes the evolution of baroclinic instability is that of quasi-geostrophic flows, which describes mesoscale flows with typical lengthscales $L \sim (10-100)$km that grow at typical advective timescales $t \sim O(L/U)$ [Pedlosky, 2013a]. Baroclinic instablity extracts available potential energy from the mean flow by relaxing the otherwise (upward) tilting isopycnals of a background state in thermal wind balance. In recent years, significant developments have taken place that incorporate non-quasigeostrophic effects on the instability process, which we present a short outline below.

We begin with a description on the effects bottom topography has on the mesoscale baroclinic instablity. In both the canonical Eady and (bottom) Charney models [Vallis, 2017], sloping bottom topography can modify the instability when the depth scale of influence of the unstable modes is large enough so that Rossby waves are able to mutually reinforce in the first place [Lozier and Reed, 2005, Pedlosky, 2013b]. For the Eady model, Blumsack and Gierasch [1972] derived the growth rates for unstable modes that incorporates the effects of (linearly) sloping bottom topography and found that, given $\gamma = \frac{-h_y}{\bar{\rho}_y/\bar{\rho}_z}$, the ratio between topographic slopes and (mean) isopycnal slopes, $\gamma \geq 1$ stabilizes the system to baroclinic instability. Sloping topography with a negative slope parameter $\gamma < 0$ (tilting in opposite direction to the isopycnal tilt), on the other hand, always promotes a destabilizing effect (Fig. 2.2). Furthermore, bottom topography destabilizes a flow (compared to the flat bottom case) when $0 < \gamma < 1$, *i.e.* isopycnals slope in the same direction as bottom topography. This situation resembles that of the Atlantic side of the IFR (south of the crest), although this region is characterized by having slope ratio $\gamma \approx 1$ [Beaird et al., 2013]. The range $\gamma < 0$ is more stable (compared to the flat bottom case) and resembles that of coastal upwelling shelf break fronts, and the outcropping front north of the IFR crest [Flagg and Beardsley, 1978, Barth, 1989, Maskell et al., 1992, Lozier and Reed, 2005, Isachsen, 2011, Beaird et al., 2013, 2016].

Concerned about the limiting quasigeostrophic scalings, Boss et al. [1996] studied the

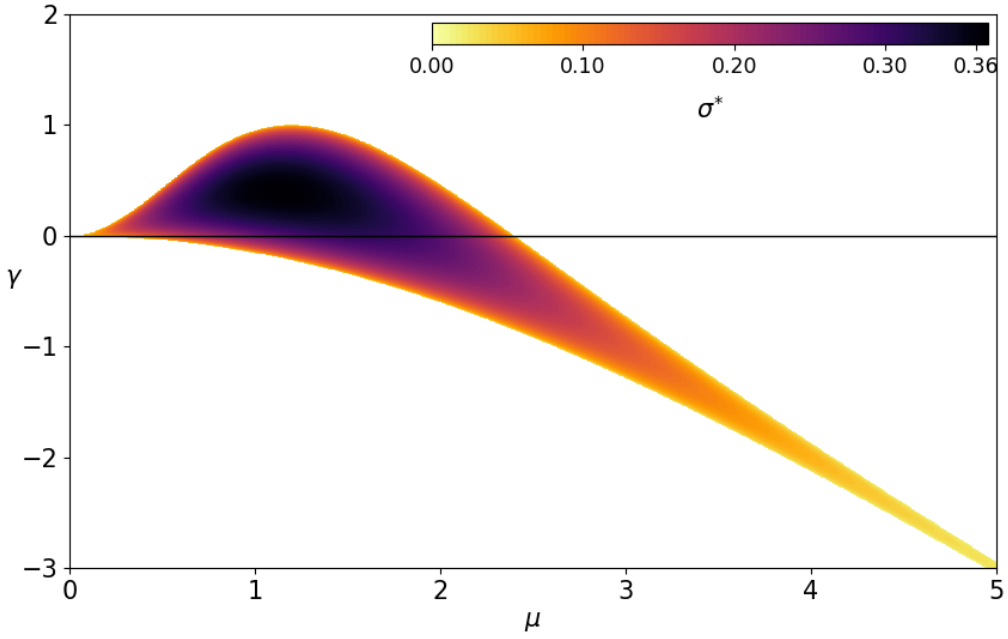

Figure 2.2: Theoretical growth rate for Eady model as a function of topographic parameter γ. $\gamma > 0$ represents the case where bottom topography slopes similarly as isopycnals, and $\gamma < 0$ when topography slopes in opposite direction as isopycnals. From Hetland [2017].

stability of outcropping density fronts using the formalism of potential vorticity fronts in two layers, allowing to cast the instability growth rate as a function of the ratio of layer stratification. They calculates growth rate of baroclinic instability for any two-layer, shallow-water model with a jet of finite horizontal extent and found that the layer thickness ratio greatly affects the most unstable modes it gets reduced by changes in layer thickness with respect to the total bottom depth. In addition, they also found evidence of a surface trapped ageostrophic baroclinic instability that results from a resonant interaction between surface gravity wave and a Rossby wave, but found that quasigeostrohic results, within their study, was robust and that the outcroping of layer PV fronts was consistent with the quasigeotrophic interpretation of PV delta sheets.

In recent years, there has been a shift of attention towards the submesoscales, character-

ized by length scales $L \sim O(1-10)km$ and timescales $t \sim O(f^{-1})$, motivated by wintertime mixed layers fronts that become unstable to baroclinic instability [Boccaletti et al., 2007]. This regime greatly departs from the QG by the vanishingly small vertical stratification and a lateral density gradient in thermal wind balance, such that $N^2_{_{ML}} \sim S^4_{_{ML}}/f^2$, or in terms of non-dimensional parameters $Ri_{_{ML}} = N^2_{_{ML}} f^2/S^4_{_{ML}} \sim O(1)$, where $N^2_{_{ML}} = g\alpha T_z$ and $S^2_{_{ML}} = -g\alpha T_y$ represent the vertical and lateral stratification (QG requires Ri¿¿1). Such conditions arise from the gravitational adjustment of a lateral density gradient within the mixed layer, promoted from either (or both) a laterally inhomogeneous, destabilizing surface forcing [Tandon and Garrett, 1994, 1995], or a homogeneous surface forcing in the presence of a preexistent lateral temperature gradient, *e.g.* a large-scale surface front.

Surface mixed layer fronts usually rest atop a tilting pycnocline (*e.g.* the sloping IFF), that acts as a lower boundary with similar destabilizing effect on the instability as sloping topography at the mesoscales [Boccaletti et al., 2007]. Nonetheless, the growth rates and lengthscales of the most unstable modes are largely determined by the mixed layer Richardson and Burger numbers $Bu_{_{ML}} = (Rd_{_{ML}}/L_{_{ML}})^2 << 1$ [Stone, 1966, Eldevik and Dysthe, 2002], given respectively by

$$\sigma = f\left(\frac{5/54}{1 + Ri + Ri \cdot Bu}\right)^{1/2} \tag{2.1}$$

with the most unstable lengthscale given by

$$\lambda = \phi_0 Rd\left(1 + \frac{1}{Ri} + \frac{Bu}{2}\right)^{1/2} \tag{2.2}$$

with $\phi_0 = 4\pi/\sqrt{10}$. Most recently, it has been shown that bottom topography can suppress bottom mixed layer baroclinic instability, in particular when the width of the plume isnarrow compared the deformation radius [Hetland, 2017], and further pushing towards non-QG effects, weakly stratified bottom boundary layers can support mixed layer baroclinic instability, which can lead to enhanced cross-slope transport through the boundary layer [Wenegrat et al., 2018].

2.3 Model Configuration

We use the Regional Ocean Modeling System (ROMS) [Shchepetkin and McWilliams, 2005] that solves the primitive equations using a terrain-following sigma coordinate. The vertical coordinate stretching results from the presence of a topographic ridge $h = h(y)$ such that the maximum depth is 1000 m away from topography and the minimum is 500 m at the crest of the ridge (see Appendix A for analytical configuration). This promotes a vertical resolution Δz that varies between 2 m and 15 m atop the ridge, with the higher resolution near the top and bottom boundaries. The channel domain has horizontal dimensions of $L_x = 250$ km in the zonal (x, or equivalently along ridge) direction, and by $L_y = 600$ km in the meridional (y, or equivalently cross ridge) direction. The horizontal resolution is $\Delta x \approx \Delta y \approx 1\ km$. We use a horizontal (harmonic) viscous dissipation on both temperature ($\kappa_h = 15\ m^2 s$) and momentum ($\nu_h = 25\ m^2 s$), and vertical diffusitivites $v_v = 3 \times 10^{-3} m^2 s$ and $\kappa_v = 10^{-5} m^2 s$.

Throughout all the experiments we use the f-plane approximation with $f = 1.25 \times 10^{-4} s^{-1}$ and use the linear equation of state with density given by $\rho = \rho_0 \left(1 - g\alpha(T(x, y, z, t) - T_0)\right)$, where T is the temperature and T_0 a reference (constant) value, $g = 9.81 m s^{-2}$ is gravity and $\alpha = 1.7 \times 10^{-4}\ {}^{\circ}K^{-1}$ is the coefficient for thermal expansion. All the simulations are unforced in order to focus on the initial development of baroclinic instabilities and their effect on the mean flow.

The initial conditions are characterized by a zonal jet in thermal wind balance with a temperature front $T(y, z)$ (see Appendix for analytical configuration). The temperature front is characterized by the presence of a top to bottom outcropping thermocline $\theta(y, z)$, defined as the temperature range where the magnitude of the temperature gradient is maximum at each point (y, z). For all simulations, the initialization is done in two steps. First, the initial configuration of a flow in thermal wind balance $u = u(y, z)$ is spun-up for a period of 30 days in order to develop an Ekman flow due to the model's no-slip bottom boundary condition. Secondly, we take the time-average of the horizontal velocities and temperature over the second half of the spun-up period, and we add to the temperature unbalanced small

amplitude (spatially) random perturbations with amplitude $T_p = \pm 0.2°C$.

We perform two sets of simulations each consisting of 3 experiments. In the first set, with experiments denoted as $\{A, B, C\}$, we focus on the instability of the jet in thermal wind balance with a large scale temperature front described in the previous paragraph (Fig. 2.3). In this configuration, eddies that grow from the instability of the jet can adiabatically flux heat across the front, a direct eddy-driven exchange between the cold Nordic waters and the warm North Atlantic. The main difference between the three experiments is that the initial jet in thermal wind balance with the temperature front is progressively shifted towards deeper waters, *i.e.* we vary the position of the jet along the topographic slope. The slope of the frontal thermocline z_θ remains fixed, but the different topographic slope below the jet results in different slope parameter, *i.e.* γ_{NO} becomes less negative from C to B, and again from B to A (see Table2.1) [1]. The differing values of γ_{NO} represent the observed change in tilt of the IFF from more negative values near Iceland where IFF slopes steeper, to less negative values near the Færæ Islands where the front slopes more gently.

The surface jet represents the component of the Færæ branch that is fed by the Iceland-Færæ Front, with transport given by $Q_{FB} = \int\int_{A_{NO}} u(y,z) dA_{NO}$ (the area A_{NO} represents the cross sectional area bounded meridionally by the contours where the surface jet is at least 10% of its maximum, and depths shallower than $z = z_\theta$). Q_{FB} is nearly constant for all the experiments (see Table 2.1).

The second set of simulations, denoted by $\{A_{ML}, B_{ML}, C_{ML}\}$ (Fig. 2.3), represents a variation of the above initial conditions where the warm upper frontal layer (with $T \geq \theta$) has vertical shear and lateral stratification typical of mixed layer fronts. To introduce a mixed layer front that exists on the warm side of the outcropping polar front, we add a lateral temperature gradient, on depths shallower that z_θ, to the temperature distribution in experiments $\{A, B, C\}$. Analytically the frontal structure is given by

---

[1] The subscript $_{NO}$ indicates that γ is averaged over a region where the near-bottom velocity is at least 75% of its maximum value, on the Nordic flank of the ridge

Table 2.1: Parameters of the frontal jet in thermal wind balance with the temperature front.

Experiment	$Q_{_{OV}}$ $[Sv]$	$Q_{_{FB}}$ $[Sv]$	$N^2_{_{NO}}[10^{-6}]$	$u_{max_{_{NO}}}$ $[m/s]$	$\lvert Ro\rvert_{max}$	$h_{y_{NO}}$ $[10^{-3}]$	$\gamma_{_{NO}}$	$\sigma[d^{-1}]$
A	3.05	2.85	10.2	0.6	0.12	-3.48	-0.74	0.386
B	3.05	2.95	9.02	0.42	0.075	-4.16	-0.88	0.223
C	2.7	3.19	6.42	0.34	0.04	-4.85	-1.04	0.139
$A_{_{ML}}$	4.1	2.87	10.03	0.48	0.16	-2.94	-0.75	0.45
$B_{_{ML}}$	4.2	3.02	8.72	0.34	0.1	-4.85	-0.84	0.42
$C_{_{ML}}$	3.9	3.34	6.11	0.33	0.07	-5.47	-0.98.	0.432

$_{NO}$: Means the variable has been averaged on the *Nordic* flank of the ridge, over the whole vertical column but with a lateral extension determined by the condition on the bottom flow: $\overline{u} \geq 0.75 u_{max}$ (except u_{max} which represents the max velocity over such area).

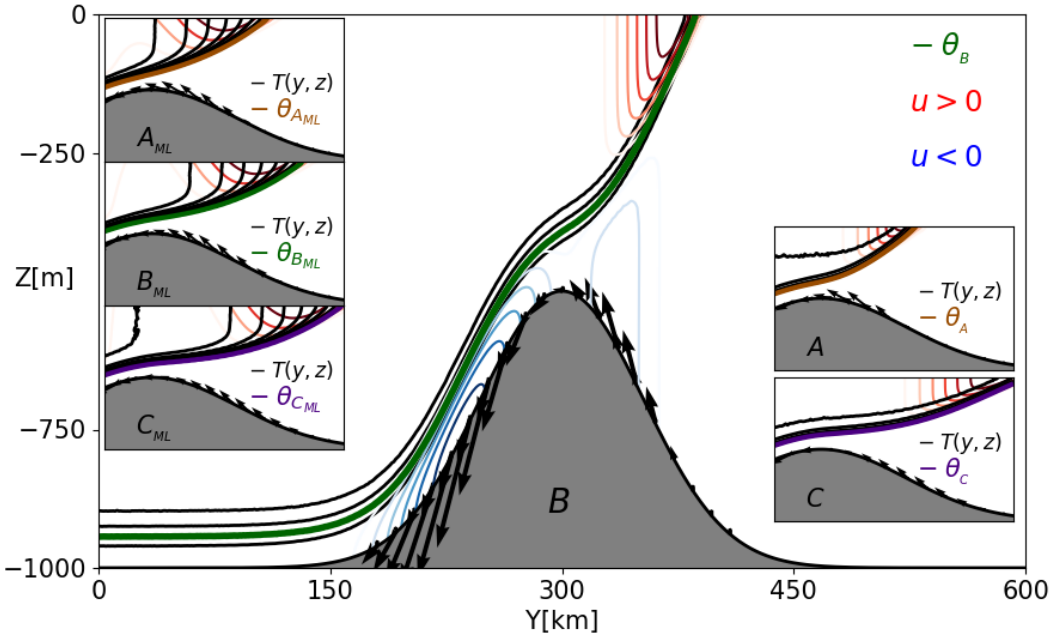

Figure 2.3: Initial distribution of zonal velocity (red and blue contours) and temperature (black contours) for experiments with no mixed layer front $\{A, B, C\}$, and those with mixed layer front $\{A_{ML}, B_{ML}, C_{ML}\}$. The (outcroping) thermocline θ for each experiment is shown as a thick colored contour, and its spatial range and location with respect to the bottom topography is identical in experiments A and A_{ML} (θ_A, gold contour), in B and B_{ML} (θ_B, green contour) and in experiments C and C_{ML} (θ_C, purple contour). Temperature contours are plotted every 0.5°C, and the black arrows represent the cross-ridge frictional bottom transport V_{EK}.

$$T(y,z)_{ML} = T(y,z) - \Delta T_{ML} \tanh\left(\frac{y - y_{ML}}{L_{ML}}\right)\mathcal{H}(z - z_\theta) \tag{2.3}$$

where $T(y,z)$ is the temperature distribution that defines the experiments $\{A, B, C\}$. ΔT_{ml} represents half the temperature jump associated with the lateral temperature gradient that results in the mixed layer front before gravitational adjustment. y_{ml}, L_{ml} represent a centering parameter for the mixed layer front and the deformation scale of the mixed layer front, respectively. $\mathcal{H}(z - z_\theta)$ represents the Heaviside function applied at a varying depth

level z_θ. The frontal temperature distribution, as given by (2.3), represents an outropping polar front with a lateral temperature gradient and vanishing vertical stratification above and near the outcropping thermocline that results from convective homogenization of the upper mixed layer, thus representing winter conditions.

The important parameters that control the structure of the mixed layer front in experiments $\{A_{ML}, B_{ML}, C_{ML}\}$ are the mixed layer Richardson number $Ri_{ML} \sim O(1)$, the mixed layer deformation radius $Rd_{ML} = N_{ML}H_{ML}/f$, with H_{ML} being the depth of the mixed layer, and the mixed layer Burger number $Bu_{ML} << 1$ (see Table 2.2). The (theoretical) growth rate and wavelength for the most unstable wave, given a $Ri_{ML} \approx 1.9$ using (2.1) and (2.2) for the three simulations $\{A_{ML}, B_{ML}, C_{ML}\}$ is $\sigma^{-1} \approx 0.5$ days and $\lambda \approx 5$km. The mixed layer frontal region is located on the anticyclonic flank of the jet, within a background barotropic anticyclonic shear that introduces a strong barotropic flow within the mixed layer front $U_{bt_{ML}}$, such that the ratio $U_{bc_{ML}}/U_{bt_{ML}} << 1$.

As in experiments $\{A, B, C\}$, we vary the location of the jet with respect to the ridge crest, thus varying the slope parameter γ_{NO}, but the mixed layer parameters that are set by a local adjustment of purely vertical isotherms experience little modification between experiments. Thus, the first set of experiments $\{A, B, C\}$ can be thought of control cases for $\{A_{ML}, B_{ML}, C_{ML}\}$, respectively, and the presence of the mixed layer frontal region, characterized by $Ri_{ML} \sim O(1)$ within the Atlantic side of the main front (warm temperature classes $T \geq \theta$), allows us to consider experiments $\{A_{ML}, B_{ML}, C_{ML}\}$ as representing wintertime conditions, and therefore allows us to test whether topography and mesoscale instability can have an effect on mixed layer instability.

For all the simulations we use quadratic bottom drag, with drag coefficient $C_D = 2.5 \times 10^{-3}$. The bottom flow below the main thermocline θ is westward, resulting in *upwelling* conditions within a thin bottom Ekman layer on the Nordic flank of the ridge and *downwelling* conditions on the Atlantic flank (see Fig. 2.3). This represents a crude approximation to cross-ridge bottom overflow. The bottom intensified gravity current on the Atlantic flank is in thermal wind balance with the gently sloping frontal isotherms that connect to the

Table 2.2: Relevant parameters for the mixed layer front, averaged over the width of mixed layer front.

Experiment	$N^2_{ML}[10^{-7}]$	$S^2_{ML}[10^{-8}]$	H_T	$H_{ML}[m]$	$U_{bt_{ML}}[m/s]$	$U_{bc_{ML}}[m/s]$	Ri_{ML}	Rd_{ML} $[km]$
A_{ML}	3.28	5.35	561	135	0.23	0.06	1.79	2.72
B_{ML}	3.81	5.48	685.6	125.4	0.23	0.05	1.98	2.73
C_{ML}	3.51	5.52	823.3	102.5	0.25	0.05	1.8	2.47

surface outcrop. The ratio γ_{NA} (γ is averaged in a region where the bottom flow is at least 75% of its maximum in absolute value, south of the ridge crest) is close to unity for all the experiments, in agreement with observations of the region [Beaird et al., 2013]. As a result, the bottom intensified gravity current is more stable to baroclinic instability than that of the upper ocean front and does not play a role in this study, while frictional effects on the bottom current are still at work. The zonal volume flux by the bottom intensified flow $Q_{OV} = \int\int_{A_{NA}} \overline{u} dA_{NA}$ (the area A_{NA} represents the cross sectional area bounded meridionally by the contours where the surface jet is at least 75% of its maximum in absolute value, and depths greater than $z = z_\theta$) is a measure of the strength of the non-local overflow transport associated with the Færæ Bank channel [Prater and Rossby, 2005, Beaird et al., 2013], and is always negative representing westward transport (see Table2.1).

The IFR is not an infinitely long ridge and the IFF is not reentrant, but it is also not (statistically) equilibrated. The warm water inflow across the IFR has a finite time residence that can be approximated by the advective timescale of the front $T_{Ad} = u_{max_{NO}}/L_x \approx$10 days (for all simulations). As such, the IFF can be thought of as always in the initial stages of (mesoscale) baroclinic instability. Here, we focus on the instability behavior up until a time T_{Ad} after the initial development of baroclinic instability.

2.4 Model Results

In this section we examine the characteristics of the initial development of the instability and the impact of the eddies on the mean flow once they reach finite amplitude. We begin by looking at the differences of the instability growth rates in the different experiments, before performing an energetics analysis that allows us to identify the dominant mechanisms driving the instability. We end this section by looking at the effects of eddies on the cross-slope transport, where we examine the modification of the bottom Ekman transport and also the eddy-driven overturning circulation that is localized to the instability. In order to distinguish between mean and eddy components of the flow, we define the *mean* as the zonal average $\overline{(\cdot)} = \frac{1}{L_x}\int_0^{L_x}(\cdot)dx$ and the *eddy* as any deviation from the mean (*e.g.* given the mean

flow $\overline{\mathbf{u}}$, the eddy component is $\mathbf{u}' = \mathbf{u} - \overline{\mathbf{u}}$ such that $\overline{\mathbf{u}'} \equiv 0$, at any given time).

2.4.1 Baroclinic Instability: Initial Development

The initial development of the unstable jet is controlled by the growth of the most unstable wave, which in all simulations takes place at the surface. In experiments $\{A, B, C\}$, the eddies are more pronounced at the location of the frontal surface outcrop, with their behavior associated with their location relative to that of the surface frontal jet, even at the nonlinear finite amplitude phases (Figs. 2.4a, 2.4c and 2.4e). Eddies in experiments $\{A_{ML}, B_{ML}, C_{ML}\}$, on the other hand, grow south of the location of the surface jet within the mixed layer front and although these eddies break northwards towards the location of the surface jet once reaching finite amplitude (Figs. 2.4b, 2.4d and 2.4f), the controlling dynamics during initial growth are associated with the baroclinicity within the mixed layer.

The initial development of the instability when it is dominated by a single most unstable mode, can be analyzed by examining the time-evolution of the volume integrated eddy kinetic energy $E_{EKE} = \frac{1}{2}\overline{\mathbf{u}'^2_h}$, where $\mathbf{u}'_h$ represents the horizontal component of the eddy velocity. Assuming that the initial perturbation growth is exponential (so that $E_{EKE}(t) \sim E_{EKE}(0)\exp(2\sigma t)$), the growth rate σ of the perturbation kinetic energy can be estimated, following Badger and Hoskins [2001], Reszka et al. [2002] by:

$$\sigma = \frac{1}{2}\frac{d}{dt}\left[\ln\left(\frac{E_{EKE}(t)}{E_{EKE}(0)}\right)\right] \tag{2.4}$$

All of the model experiments show a constant growth rate (Fig. 2.5) with the most unstable mode ($\sigma(t) \sim \sigma_0$) dominating only for a finite time T_σ. For experiments $\{A, B, C\}$, the initial growth rate decreases as the initial frontal jet moves into deeper water (42% reduction from A to B, and a reduction of 36% from B to C, Fig. 2.5a). The calculated growth rates imply a growth timescale $\tau = (2\sigma)^{-1} \approx 1$ day in experiment A, τ =2.5 days in B and about $\tau = 4$ days in experiment C. The length scale of the instability $\lambda \approx 60$ km is the same for experiments $\{A, B, C\}$. The observed reduction in growth rates (increase

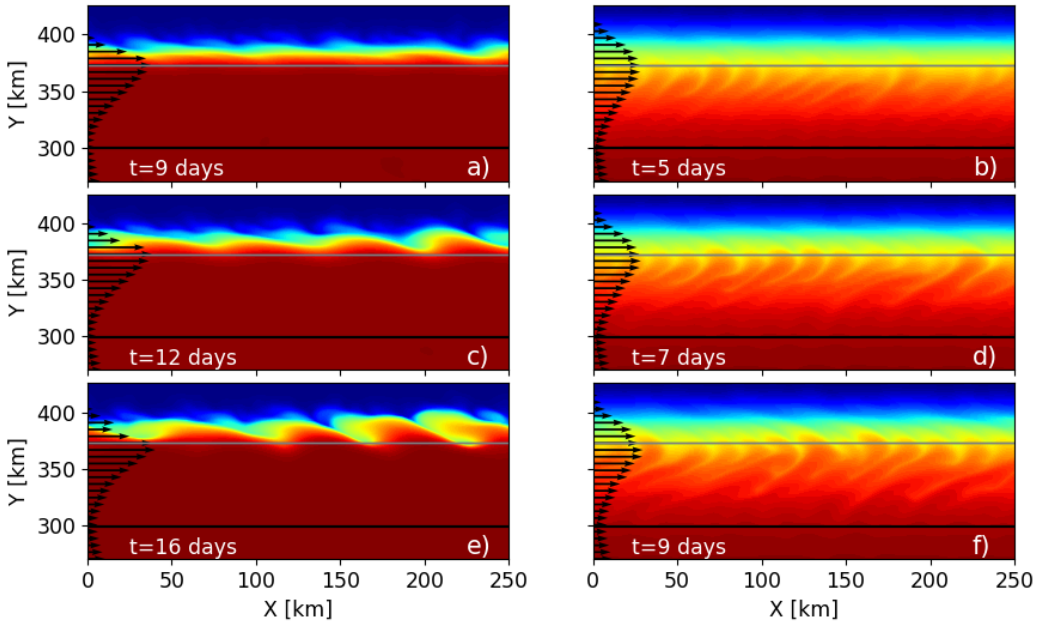

Figure 2.4: Sea surface temperature showing the development of baroclinic instability in experiment B (left) and experiment B_{ML} (right), the latter one characterized by the presence of mixed layer eddies. $\Delta T = 6°C$ across the front. The black arrows represent the zonal-mean surface jet $\overline{u}(y, 0, t)$, with the gray line showing the location of surface jet maximum $\max(\overline{u}(y))$ before the onset of instability. The ridge crest is identified by the solid black line.

growth timescale) agrees well with the expected behavior as a result of the frontal jet moving to a region with a more stabilizing slope parameter γ_{NO}, *i.e.* γ_{NO} becomes more negative. In addition, the bottom layer thickness $h_2 = \int_{z=-h}^{z=z_\theta} dz$ increases with respect to the upper layer thickness $h_1 = \int_{z=z_\theta}^{z=\eta} dz$ as the initial jet moves towards deeper water (from A to B, and then from B to C), thus increasing the depth ratio parameter and therefore indicating a theoretical reduction in the growth rate (from A to B and then to C). Thus, both the changes in slope parameter and changes in depth ratio act together to reduce the growth rate as the jet is shifted towards greater (total) depth.

The growth rates of experiments $\{A_{ML}, B_{ML}, C_{ML}\}$ show little modification as the jet

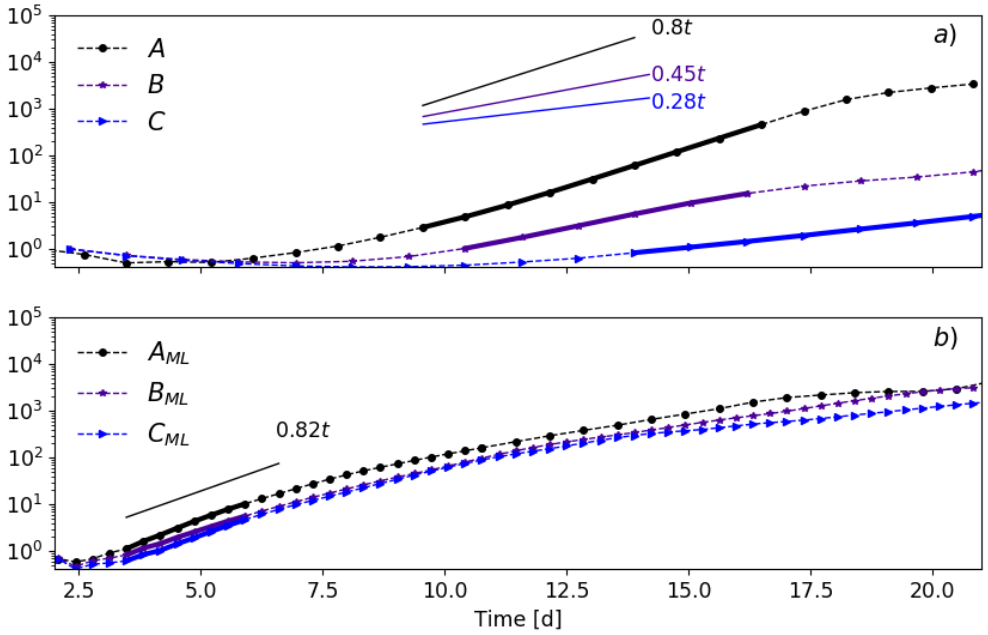

Figure 2.5: Normalized Eddy kinetic energy ($E_{EKE}(t)/E_{EKE}(0)$) for a) $\{A, B, C\}$ and b) $\{A_{ML}, B_{ML}, C_{ML}\}$ as a function of time. Thick, short, colored lines represent the linear approximation to the most unstable growth $\sigma(t) = \sigma_0$. The value of σ_0 is calculated by fitting an exponential curve of the form ae^{bt} to each normalized kinetic energy. Then, $2\sigma_0 = b$.

moves towards deeper waters (Fig. 2.5b). The growth rate decreases 5% from A_{ML} to B_{ML} even when the location of maximum E_{EKE} shifts towards deeper waters, as seen by examining the relative meridional location of maximum dE_{EKE}/dt and maximum E_{EKE}, between experiments (see Figs. 2.6d, 2.6e, and 2.6f). The calculated growth rates imply an e-folding (growth) timescale for $\mathbf{E}_{EKE}$ of $\tau = (2\sigma)^{-1} \approx 1$ day. In addition, the maximum in dE_{EKE}/dt and the maximum in the surface jet do not coincide, suggesting that the MLEs grow separately from the mesoscale instability of the mean jet, despite the mean jet being unstable. The calculated growth rate for baroclinic instability in C_{ML}, however, is almost the same than that of A_{ML}. This agrees well with the Richardson number (Ri_{ML}) calculated at the location of maximum dE_{EKE}/dt during initial linear growth (see Table 2.2) and reflects

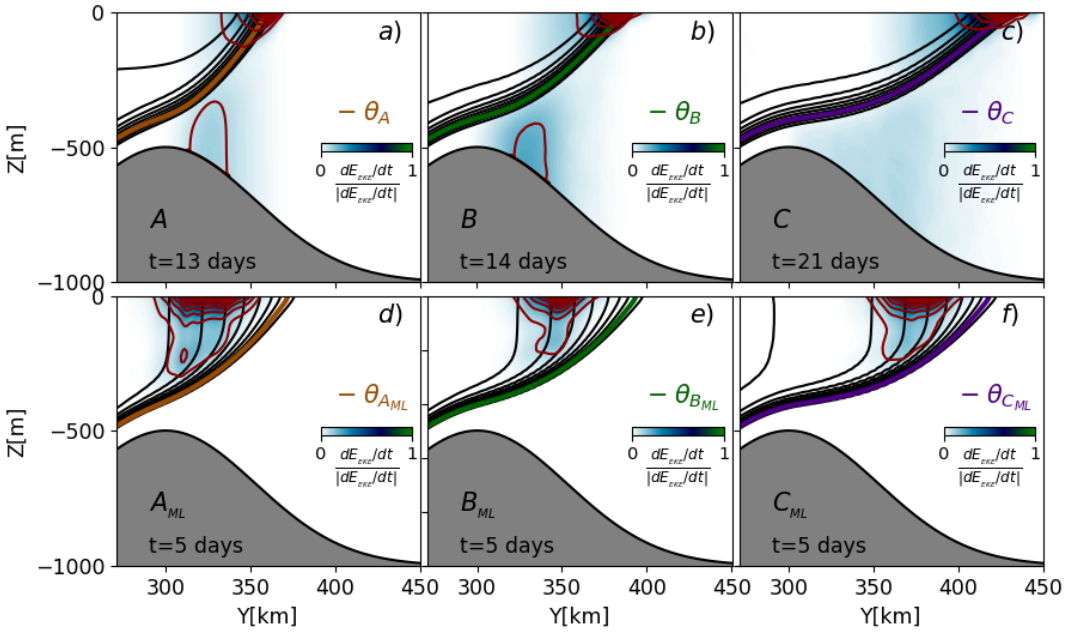

Figure 2.6: Spatial distribution of normalized dE_{EKE}/dt for all simulations when the growth is approximately linear ($\sigma \approx \sigma_0$). Red contours represent the location of normalized E_{EKE} with 10% increments, and black contours represent mean temperature $\overline{T}$, with 0.5°C increments. Thick colored contour indicated the location of the thermocline θ.

no direct influence of the changes in bottom depth.

MLEs have a lateral scale $\lambda \approx 10$ km around day 7, after the onset of initial instability, a much smaller scale than the width of the mixed layer frontal region L_{ML} (Fig. 2.4b). This results in eddies having different sizes and growth rates depending on where they originate with their properties depending on the local slope of the base of the mixed layer and local barotropic shear. Nevertheless, the growth rate represents that of the most unstable modes for each simulation and these modes largely determine the evolution of the mixed layer front. During their initial development, MLEs are entirely confined to the upper warm waters (corresponding to the temperature classes warmer than θ), with a strong vertical density jump associated with the thermocline θ acting as the bottom boundary to the surface mixed

layer baroclinic instability in the initial development phase, making growing MLEs insensitive to the topographic slope [Boccaletti et al., 2007].

2.4.2 Eddy-Mean Energetics

In order to better understand the differences between the two sets of experiments and to help identify the dominant mechanisms driving the instabilities, we examine the time evolution of the mean and eddy kinetic energy. The mean and eddy kinetic energy equations are obtained by projecting the horizontal mean $\overline{\mathbf{u}}_h = (\overline{u}, \overline{v})$ and horizontal eddy $\mathbf{u}'_h = (u', v')$ velocity vectors onto the horizontal momentum equations, and subsequently performing the zonal average. The equations governing the mean and eddy kinetic energy, ignoring cubic terms in the perturbation that result from the triple multiplication of eddy variables (neglectable only during initial, small amplitude eddy development), are:

$$\frac{\partial E_{_{MKE}}}{\partial t} + \nabla^x \cdot \left[\overline{\mathbf{u}} \big(E_{MKE} + \overline{p} \big) \right] = \underbrace{\big(\overline{u'v'} \partial_y \overline{u} + \overline{v'v'} \partial_y \overline{v} \big)}_{\mathbf{C}_h} + \underbrace{\big(\overline{u'w'} \partial_z \overline{u} + \overline{v'w'} \partial_z \overline{v} \big)}_{\mathbf{C}_v} + \underbrace{\overline{w} \overline{b}}_{\mathbf{C}_{MA}} + \underbrace{\overline{\mathbf{u}} \cdot \overline{\mathcal{D}}}_{\overline{\epsilon}} + O(\overline{\mathbf{u}}^3) \tag{2.5}$$

$$\frac{\partial E_{_{EKE}}}{\partial t} + \nabla^x \cdot \left[\overline{\mathbf{u}} E_{EKE} + \overline{\mathbf{u}' p'} \right] = - \underbrace{\big(\overline{u'v'} \partial_y \overline{u} + \overline{v'v'} \partial_y \overline{v} \big)}_{\mathbf{C}_h} - \underbrace{\big(\overline{u'w'} \partial_z \overline{u} + \overline{v'w'} \partial_z \overline{v} \big)}_{\mathbf{C}_v} + \underbrace{\overline{w'b'}}_{\mathbf{C}_{EA}} + \underbrace{\overline{\mathbf{u}' \cdot \mathcal{D}'}}_{\overline{\epsilon'}} + O(\overline{\mathbf{u}'^3}) \tag{2.6}$$

where $\nabla^x = (0, \partial_y, \partial_z)$. The second term on the lhs of both (2.5) and (2.6) represent adiabatic redistribution of kinetic energy by advective convergence and by pressure work, and therefore do not represent net sources or sinks of energy (*i.e.* their integral are zero) [Heifetz et al., 1998]. The dissipation terms of the mean kinetic energy ($E_{_{MKE}}$) and eddy kinetic energy ($E_{_{EKE}}$) are given by $\bar{\epsilon}$ and ϵ' respectively, and constitute an irreversible loss of total kinetic energy that result from viscous (harmonic) numerical dissipation. The four terms $\mathbf{C}_h$, $\mathbf{C}_v$, $\mathbf{C}_{_{EA}}$ and $\mathbf{C}_{_{MA}}$ represent *energy convergence* that promote energy transfer associated with the presence of instability processes. Both $\mathbf{C}_h$ and $\mathbf{C}_v$ represent flow of energy between the mean and eddy kinetic energy and require the presence of mean horizontal ($\mathbf{C}_h$)

or mean vertical ($\mathbf{C}_v$) shear, and result from a mechanism of barotropic or Kelvin-Helmholtz instability [Samelson and Chapman, 1995]. $\mathbf{C}_{MA}$ represents the energy transfer between E_{MKE} and the mean available potential energy E_{MAPE}, while $\mathbf{C}_{EA}$ represents the transfer of energy between E_{EKE} and the eddy available potential energy E_{EAPE}.

The evolution of the mean and eddy kinetic energy budgets (2.5) and (2.6) demonstrate the processes that control both the linear and nonlinear phases of the instability (Fig. 2.7). Here, we analyze the E_{EKE} budgets for C and C_{ML}, that represent the typical initial behavior of $\{A, B, C\}$ and $\{A_{ML}, B_{ML}, C_{ML}\}$, respectively. In experiment C, *baroclinic production* of E_{EKE} ($\mathbf{C}_{EA}$) dominates the initial growth ($t = 16$ to $t = 21$ days), indicating that baroclinic instability is the dominant mechanism that feeds the growing eddy field (Fig. 2.7c). Baroclinic production is positive throughout, signaling a continuous transfer energy from eddy available potential energy (E_{EAPE}) into E_{EKE}. During this initial growth both $\mathbf{C}_h$ and $\mathbf{C}_v$ are nonzero and negative, but much smaller and therefore non dominant. After the initial growth phase in experiment C ($t > 21$ days after initialization), $\mathbf{C}_h$ dominates the evolution of E_{EKE}, driving a decrease in E_{EKE} and an increase in E_{MKE}. This coincides with wave breaking and eventual separation of cold-core eddies that propagate southwards toward shallow water observed (but not analyzed here), characteristic of the life cycle of fronts [Simmons and Hoskins, 1978, Samelson and Chapman, 1995, Skyllingstad and Samelson, 2012].

The evolution of E_{EKE} for simulations A_{ML} and B_{ML} is very similar to that of C_{ML} (shown in Fig. 2.7d). Eddy energy growth is dominated throughout by baroclinic production term $\mathbf{C}_{EA}$, with very small net contributions to E_{EKE} by $\mathbf{C}_h$. Harmonic viscous dissipation promotes a small but continuous sink on the energy balance.

The growth in E_{EKE} is greatest near the upper and bottom boundaries that vertically bound the growing baroclinic waves, in agreement with the energetics within the Eady model [Eady, 1949, Heifetz et al., 1998], which for $\{A, B, C\}$ these boundaries are the ocean surface and bottom topography (Fig. 2.6). Thus for $\{A, B, C\}$ the instability is full depth. The growth in E_{EKE} is greatest within the mixed layer front for experiments $\{A_{ML}, B_{ML}, C_{ML}\}$, bounded above by the ocean surface and below by the thermocline θ. This implies that this

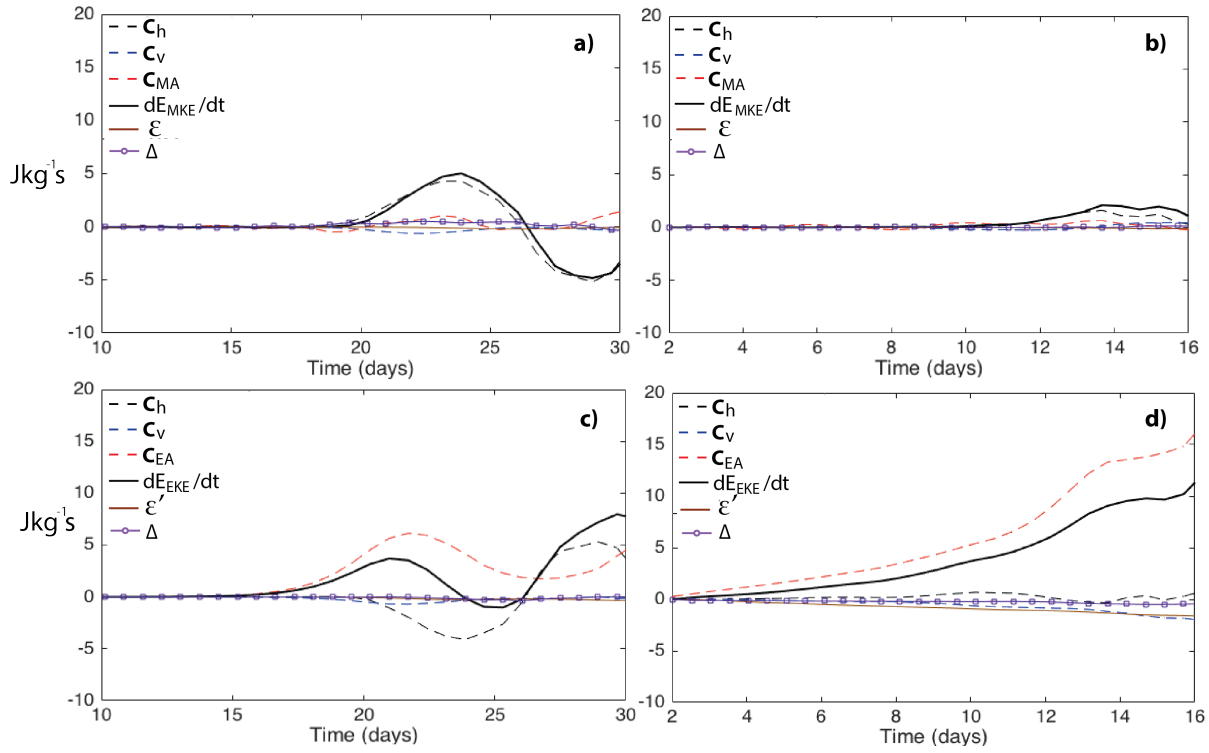

Figure 2.7: Terms in the E_{MKE} (top row) and E_{EKE} (bottom row) budget equations for experiment C (a, c) and C_{ML} (b, d) respectively. ϵ and ϵ' were calculated by multiplying $\overline{\mathbf{u}_h}$ and $\mathbf{u}'_h$ times the horizontal viscosity terms that are calculated within the model diagnostics. Δ represents the residual from the budgets equations (2.5) and (2.6).

surface intensified modes grow by extracting perturbation available potential energy and restratifying the mixed layer front [Boccaletti et al., 2007].

The difference of the vertical structure of the instability waves between $\{A, B, C\}$ and $\{A_{ML}, B_{ML}, C_{ML}\}$ is even more apparent in the distribution of the dominant terms in the eddy kinetic energy budgets (2.6) in temperature space. During linear baroclinic instability (*e.g.* the Eady problem), buoyancy production $\mathbf{C}_{EA}$ is greatest where dE_{EKE}/dt is minimum, which for experiments $\{A, B, C\}$ is near the thermocline θ (Figs. 2.8a, 2.8b and 2.8c), since it is there that the greatest temperature perturbations take place. In experiments $\{A_{ML}, B_{ML}, C_{ML}\}$ the spatial distribution of both dE_{EKE}/dt and $\mathbf{C}_{EA}$ is entirely located in the upper warm layer ($\overline{T} > \theta$), and decays exponentially to zero below the thermocline θ.

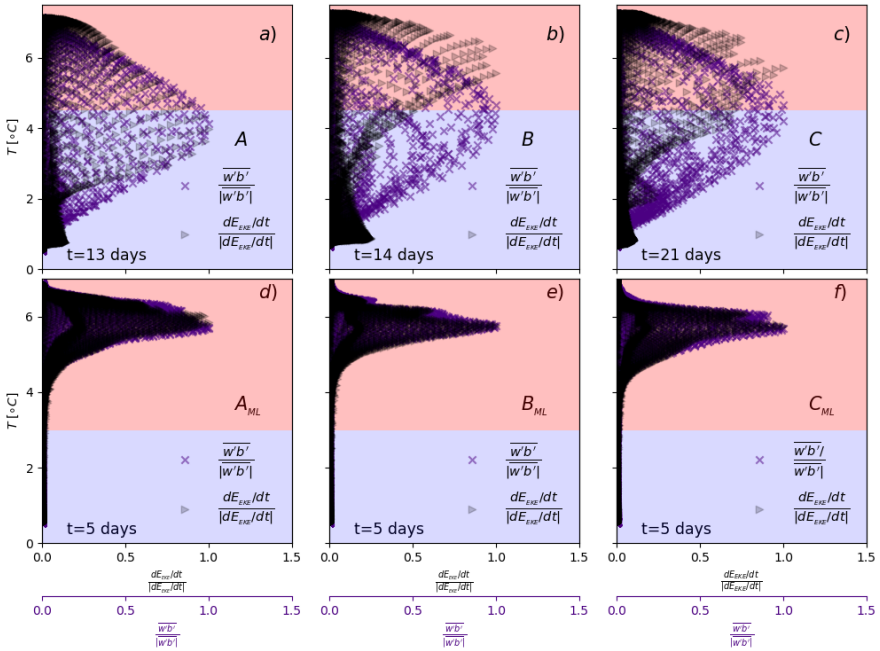

Figure 2.8: Distribution in (mean) temperature space of normalized eddy kinetic growth dE_{EKE}/dt and normalized buoyancy production $\mathbf{C}_{EA} = \overline{w'b'}$ during linear growth, corresponding to the spatial distribution shown in Fig. (2.6). Red shading represents mean temperature greater than that of the thermocline $z = \theta(y, z)$ (and thus the upper layer), and blue shading represent mean temperature values lower than that of the mean thermocline (lower layer).

This means that the mechanism for instability is confined above the thermocline which acts as a bottom PV sheet that drives the instability process [Callies et al., 2016]. Furthermore, the confinement above the thermocline of the mixed layer baroclinic instability suggest that during initial development, bottom topography has no influence on the initial growth of mixed layer eddies, a result that agrees with the calculated growth rates.

The sloping bottom topography below the thermocline on the Nordic flank, however, destabilizes the flow at the mesoscales during the initial growth, and can still have an effect

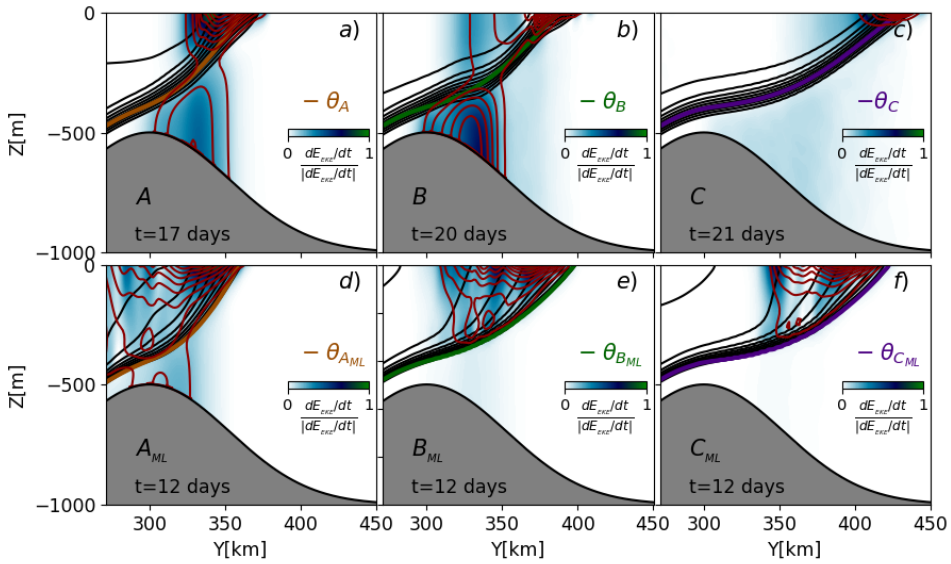

Figure 2.9: Spatial distribution of normalized dE_{EKE}/dt for all simulations at a time much after the linear growth phase. Red contours represent the location of normalized E_{EKE} with 10% increments, and black contours represent mean temperature $\overline{T}$, with 0.5°C increments. Within each subfigure, the thick colored contour represents the location of the thermocline during linear development.

on the instability in $\{A_{ML}, B_{ML}, C_{ML}\}$ after the initial growth. Just as the configuration in A is more unstable to that of B and C owing to sloping bottom topography, the same is true for A_{ML} with respect to B_{ML} and C_{ML}, even though this is not seen during initial growth. Eight days after initial development (12 days after model initialization), the spatial structure of dE_{EKE}/dt associated with A_{ML} shows evidence that the instability fills the water column (Fig. 2.9d). dE_{EKE}/dt shows a secondary maximum at the bottom. The spatial distribution of dE_{EKE}/dt with respect to the mean temperatures also shows the full depth growing instability, since it no longer decays to zero below the thermocline, at this time (Fig. 2.10d). This shows that, while sloping bottom topography does not affect the initial growth rates of mixed layer eddies, we find that it allows a faster growth of mesoscale modes whenever the sloping bottom acts to destabilize the bottom layer in agreement with

mesoscale results [Blumsack and Gierasch, 1972, Lozier and Reed, 2005, Isachsen, 2011]. In experiments $\{A_{ML}, B_{ML}, C_{ML}\}$, the spatial distribution of eddy kinetic energy growth and buoyancy production shows various maxima over a range of temperature classes, a direct consequence of the MLEs being much smaller than the lateral extent of the mixed layer frontal region (Figs. 2.10d, 2.10e and 2.10f, and Figs. 2.11d, 2.11e and 2.11f, respetively). In contrast, the spatial distribution of eddy kinetic energy growth and buoyancy production of the instability in experiements $\{A, B, C\}$ shows a maximum, most likely associated with the most unstable growing mode that is dominating the eddy variability (Figs. 2.11a, 2.11b and 2.11c, respectively).

The continuous large contribution of the buoyancy production on the evolution of E_{EKE} represents continuous restratification and lateral heat advection that extends over most of time period considered in this analysis. The restratification is characterized by a net change in the zonally averaged potential energy of the system that results from the cross-slope adiabatic heat flux, which we investigate next.

2.4.3 Cross-Slope Transport

In this section we look at the meridional transport driven by the eddies and the mean flow. The (along-isobath) mean flow promotes a cross-slope transport in the presence of bottom friction (bottom arrows in Fig. 2.3), where most of the transport is confined within a narrow bottom Ekman layer of thickness $\delta_{Ek} = \sqrt{2\nu/f} \approx 7m$ where ν is the vertical viscosity. The mean flow configuration favors, through bottom Ekman transport V_{Ek}, *downwelling* conditions on the Atlantic flank of the ridge and upwelling conditions on the Nordic flank of the ridge [MacCready, 1994, Condie, 1995, Wåhlin and Walin, 2001, Brink and Lentz, 2010]. V_{Ek} corresponds to the southward component of the mean overturning circulation (MOC) across the ridge. In the absence of atmospheric forcing, the northward component of the MOC is associated with the interior ageostrophic velocities that help maintain the flow in thermal wind balance. In all simulations, the spindown of the mean flow promotes a slow decrease of the magnitude of the Ekman transport $|V_{Ek}|$ over time, in the absence of eddies

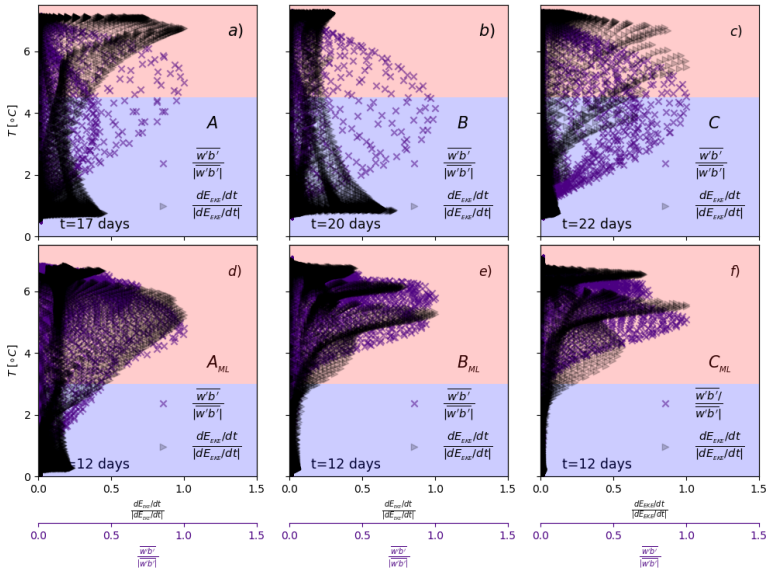

Figure 2.10: Distribution in (mean) temperature space of normalized eddy kinetic growth dE_{EKE}/dt and normalized buoyancy production $\mathbf{C}_{EA} = \overline{w'b'}$, corresponding to the spatial destribution shown in Fig. (2.9). Red shading represents mean temperatures greater than that of the thermocline $z = \theta$ (and thus the upper layer), and blue shading represent mean temperature values lower than that of the thermocline (lower layer). The presence of many local maxima in dE_{EKE}/dt (black right triangles) in $\{A_{ML}, B_{ML}, C_{ML}\}$ represent multiple growing baroclinic eddies within the mixed layer front.

or any other external forcing (Fig. 2.12a), with oscillations most likely due to the presence of internal waves. During the time span of the initial growth, $|V_{Ek}|$ shows no clear modification at either the crest of the ridge, or at the location of the maximum bottom velocities at either flank of the crest, for all simulations. In experiments $\{A, B, C\}$ the transport $|V_{Ek}|$ increases (becomes more southward) after the initial growth when the flow becomes nonlinear and cold-core lenses form that propagate southwards towards the ridge crest. These eddies can promote the increase of the bottom southward transport by locally increasing the tilt of the frontal thermocline so that the bottom flow becomes more westward and thus V_{Ek} becomes more negative and southward resulting in advection of cold water up the slope on the Nordic

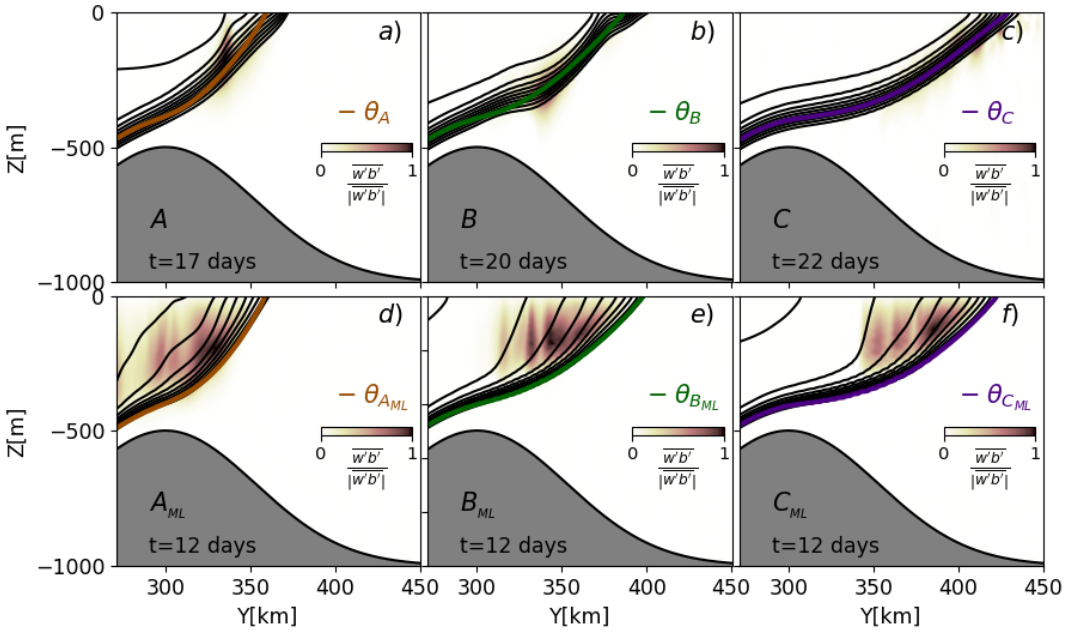

Figure 2.11: Spatial distribution across the domain shown in Fig. (2.6) of normalized buoyancy production $\mathbf{C}_{EA}$ for all simulations, at a later time after linear growth. Black contours represent mean temperature $\overline{T}$, with 0.5°C increments. Maximum values attained for experiments $\{A, B, C\}$ are associated with the thermocline, while those for experiments $\{A_{ML}, B_{ML}, C_{ML}\}$ vary spatially, signaling the presence of multiple growing eddies over the frontal region.

side of the ridge.

In experiments $\{A_{ML}, B_{ML}, C_{ML}\}$, $|V_{Ek}|$ shows no clear modification by the presence of MLEs over most of the timespan considered, *i.e.* up to day 11 after initialization, long after the initial growth phase (Fig. 2.12b). Thus, the surface-confined MLEs have little to no influence on bottom flows throughout the initial growth and beyond. At around day 12, almost 9 days after the initial development and with the eddying flow field well developed, $|V_{Ek}|$ shows a small decrease at the crest of the ridge (less southward transport), but most of the changes take place outside of the time-span considered (T_{Adv}). In contrast to the eddies in experiments $\{A, B, C\}$, the ML eddies in experiments $\{A_{ML}, B_{ML}, C_{ML}\}$ are not horizontally

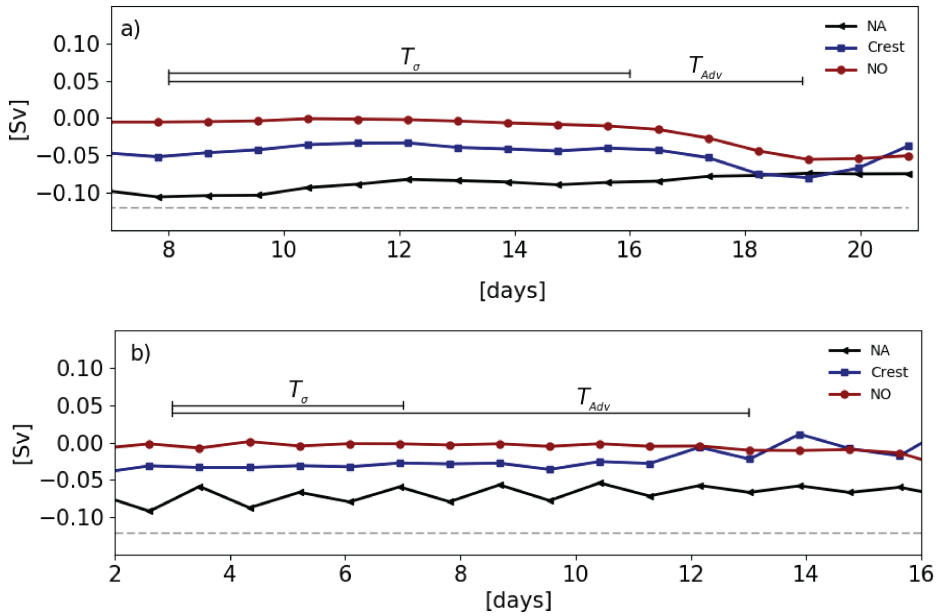

Figure 2.12: Bottom Ekman transport V_{Ek} for a) experiment A and b) experiment A_{ML} computed at three locations: At the core of the bottom-intensified jet (dotted black, denoted NA), at the crest of the ridge (dotted blue, denoted Crest) and at the location of the maximum bottom current on the Nordic flank of the ridge (dotted red, denoted NO) that is associated with the surface intensified jet. The gray line represents the estimate transport given in [Beaird et al., 2013] of $V_{Ek} = -0.12$Sv. $V_{Ek} < 0$ represents southward flow.

isolated from each other and instead eddies of different sizes fill the water column over the entire mixed layer front. Thus, the bottom transport may be dependent on the location of the bigger most unstable eddies. The location of the E_{EKE} growth is maximum at the ridge crest for experiment A_{ML}, but shifts northwards on B_{ML} and C_{ML}. In experiments B_{ML} and C_{ML}, V_{Ek} shows no clear change over the timescale considered and thus, MLE-induced changes in V_{Ek} are very sensitive to the location of the maxima in E_{EKE} and dE_{EKE}/dt.

Eddies promote an interior cross-front transport by the action of eddy fluxes along adiabatic surfaces [Vallis, 2017]. When the isothermal surfaces do not vary significantly with respect to the mean, the Transformed Eulerian Mean (TEM) developed for quasigeostrophic waves can be used to represent the circulation induced by the eddies [Plumb and Ferrari,

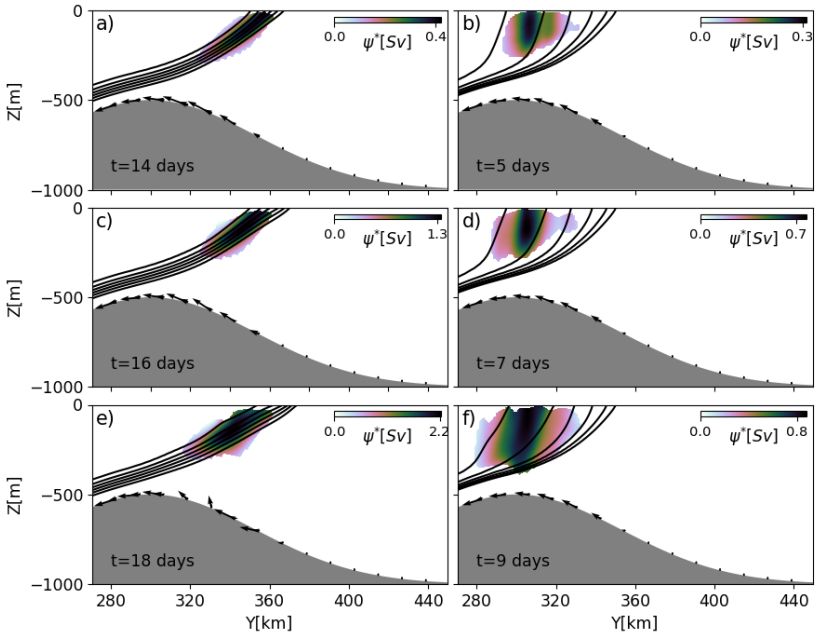

Figure 2.13: Sequence of (eddy-induced) overturning circulation ψ^* for simulations A (a, c, e) and A_{ML} (b, d, f). ψ^* is calculated by time-averaging the terms in 2.7 over a window of two days, and considering only eddy heat fluxes above or greater than 10% of the maximum $\overline{w'T'}$. The arrows represent the mean cross-slope bottom transport $(\overline{v}, \overline{w})$, scaled by the aspect ratio of the figure to show true direction. The dark contours represent the mean isotherms, plotted in 0.75°C intervals for experiment A, and 0.5°C intervals for experiment A_{ML}, all averaged over a 2-day window.

2005, Stewart and Thompson, 2015]. The eddy induced circulation ψ^* in the primitive equations is given by

$$\psi^* = \frac{\overline{v'T'}\ \ \overline{T}_z - \overline{w'T'}\ \ \overline{T}_y}{||\nabla^x \overline{T}||^2} \tag{2.7}$$

ψ^* represents a circulation that in the case of baroclinic instability waves that describes a clockwise relaxation of the tilting mean temperature surfaces $\overline{T}$ due to baroclinic eddy fluxes $\overline{v'T'}, \overline{w'T'}$. The experiments $\{A, B, C\}$ are characterized by growth of baroclinic instability dominated by the most unstable mode, with its effects on the zonal mean represenTeed by the

residual overturning circulation. The residual circulation is strongest when eddies separate from the main frontal outcrop and propagate southwards. As the eddies detach from the front southwards towards the ridge crest, their effect on the front is to subduct waters along the main frontal thermocline (Figs. 2.13a, 2.13c and 2.13c). Here, the eddies do not propagate across the ridge crest during the timescale considered, thus ψ^* has a meridional extension limited to the Nordic flank of the ridge. On the other hand, MLEs promote a residual overturning circulation ψ^* in the temperature range associated with the mixed layer front (Fig. 2.13b, 2.13d and 2.13f), and promote a rapid restratification of the mixed layer, by advecting warm surface temperature anomalies northward. ψ^* does not reach across the outcropping thermocline; instead it is confined meridionally south of the location of the mean jet where the most unstable MLEs dominate the evolution of the front.

2.5 Implications for the Iceland-Færæ Front

Eddies that result from the instability of topographically locked, rim currents that circle around convective basins play an important role in the watermass transformation at high latitudes, a central process in global climate [Spall, 2004]. Eddies that separate from baroclinic currents carry heat that is deposited far away from their generation site, near deep convection sites, providing the necessary heat to close the heat budget associated with basin-scale convective overturning [Spall, 2010]. The topographically locked IFF is the widest and shallowest open ocean boundary separating the North Atlantic from the Nordic Seas, and thus regulates the inflow of warm water across the IFR into the convective Nordic basins. The eddies that are generated along the IFF, on the other hand, advect heat across the front and therefore play an important role in regulating the amount of water that is exchanged between the Nordic seas and the subpolar North Atlantic. In this section we address the relative importance of eddies resulting from baroclinic instability of the modelled polar front.

In order to provide a measure of the role of the eddies on the exchange under the two frontal configurations in this study ($\{A, B, C\}$ and $\{A_{ML}, B_{ML}, C_{ML}\}$), we compare the advective eddy heat flux to the mean heat advection by the zonal surface jet, that represents

the flux of Atlantic waters into the Nordic basin. In the model, the along ridge (northward, since the mean flow that is along topographic contours heads northwards, once is flows past the IFR as in Fig. 2.1) flux of Atlantic waters by the mean flow is $Q_{FB} \approx 3$ Sv, close to that observed in yearlong averages [Hansen et al., 2008]. The associated advective heat flux is given by $\mathcal{H}_{FB} = \rho_0 c_p Q_{FB} \Delta T \approx 80$ TW, a factor of 2 smaller than that found during typical summertime conditions in observations [Rossby and Flagg, 2012] (in the above flux calculation, $\rho_0 = 1025\ kgm^{-3}$, $c_p = 3580\ J/(kg°C)$, and $\Delta T = 6°C$). The advective eddy heat flux $\mathcal{H}_{adv}$, given by

$$\mathcal{H}_{adv} = L_x \rho_0 c_p \int_{z=-h}^{z=\eta} \overline{v'T'} dz \tag{2.8}$$

is greatest when the instability of the front becomes nonlinear, characterized in $\{A, B, C\}$ by isolated cold anomalies that pinch off from the main front (Fig. 2.14). The location of the maximum $\mathcal{H}_{adv}$ with respect to bottom topography closely matches the averaged meridional location of the isolated eddy cores, each with length scale $\lambda^e \approx 12km$. The maximum eddy heat flux is $\mathcal{H}_{adv} \approx 50$ TW, a value comparable to that of the mean $\mathcal{H}_{FB}$ (Fig. 2.14a). When averaged over the upper 500m and over the length of the ridge, the eddy heat flux gives the upper bound maximum intensity of around $40 \times 10^4\ Wm^{-2}$, a value that agrees well with recent observational estimates [Beaird et al., 2016]. In comparison, the maximum eddy heat flux calculated for $\{A_{ML}, B_{ML}, C_{ML}\}$ over the timescale T_{adv} is $\mathcal{H}_{adv} \approx 17$ TW, which corresponds to $13.6 \times 10^4\ Wm^{-2}$ when averaged over the upper 500 m and the length of the ridge (Fig. 2.14d). The difference in the maximum eddy heat flux recorded from the eddies in $\{A, B, C\}$ and those in $\{A_{ML}, B_{ML}, C_{ML}\}$ is associated with the eddy temperatures anomalies T', and these are much larger for eddies in $\{A, B, C\}$. In addition, we find that the eddy heat flux is dependent on the sloping bottom, with the greater values resulting from the more destabilizing bottom topography (γ_{NO} less negative) when the frontal jet is located closer to the ridge crest, and the lesser values associated with less destabilizing bottom topography ((γ_{NO} more negative), *i.e.* frontal jet located over deeper waters.

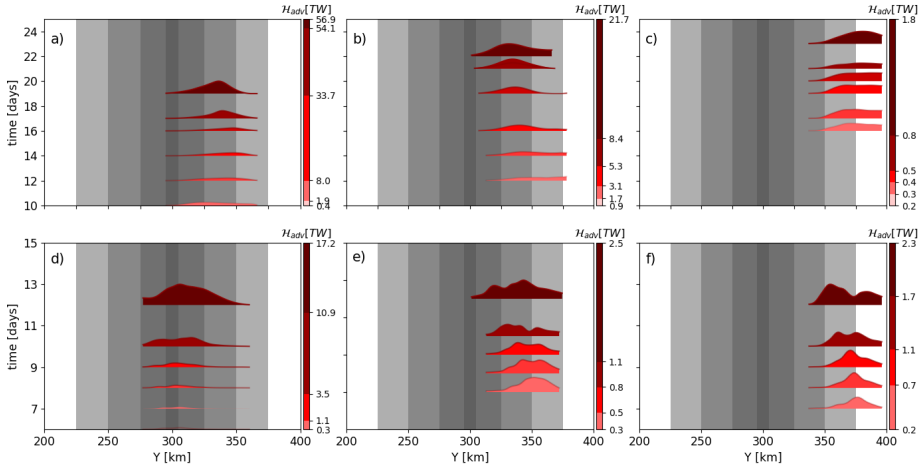

Figure 2.14: Time evolution of the meridional distribution of the advective eddy heat flux $\mathcal{H}_{adv}$ in both control experiments $\{A, B, C\}$ (a, b and c, respectively) and experiments $\{A_{ML}, B_{ML}, C_{ML}\}$ (d, e and f, respectively). At each time, the shape represents the spatial distribution with respect to bottom topography (grey-filled contours), and the color is associated with the maximum heat transport (the peak). Each spatial distribution is normalized with respect to the next, and each tick value on the discrete (red) colorbar is spaced proportional to the jump on $\mathcal{H}_{adv}$.

In experiments $\{A, B, C\}$, within the timescales considered, the isolated anomalies did not reach across the ridge crest onto the Atlantic flank. Thus, the anomalies will likely get advected downstream by the mean flow which roughly follows topographic contours. Eddies that originate closer to the ridge crest, and where the front is steeper (as in A) will be more likely to cross. These conditions are usually met on the western end of the IFF, closer to Iceland [Maskell et al., 1992]. In contrast, eddies in simulations $\{A_{ML}, B_{ML}, C_{ML}\}$ grow over the entire mixed layer baroclinic zone with their initial growth not significantly affected by depth changes below θ. Whether these eddies can induce a residual circulation that reach across the IFR initially depend on the extent of the mixed layer frontal zone, and later on the background characteristics of the frontal zone, as detailed in [Manucharyan and Timmermans, 2013]. Given the relatively shallow polar front that sits over the IFR and the

deep wintertime convection that takes place over the region, where observations show mixed layer depths on the order of 500m over the IFR in winter [Beaird et al., 2016], it is likely that mixed layer frontal zones exist and extend across the crest of the IFR.

MLEs all originate within warm temperature classes (warmer temperatures than θ) where the mixed layer front is unstable. Thus, at least during their initial growth, while MLEs advect heat laterally (Fig. 2.14b), they do not necessarily advect heat across the mean θ-contour, which represents the barrier between Atlantic and Nordic waters, as seen from the residual overturning circulation (Fig. 2.13). As MLEs restratify the mixed layer south of the main outcropping IFF, MLEs can flux surface ocean properties downward and, depending on the strength of surface cooling, can even shut down convection [Callies and Ferrari, 2018]. Eddies in experiment B induce strong vertical buoyancy and heat flux once the isolated eddies form that are linked to frontal collapse and the strong lateral temperature gradients around the isolated anomalies (Fig. 2.15). Eddies in B_{ML}, on the other hand, promote a strong surface vertical heat flux localized to the mixed layer front. The vertical heat flux associated with the MLEs grows exponentially during the initial growth, but equilibrates after that, when it becomes comparable to values expected during wintertime $\sim O(100)\ Wm^{-2}$ [Marshall and Schott, 1999]. This means that vertical heat flux driven by MLEs can become, during the timescales relevant for the IFF, an important process for the heat budget within the mixed layer, potentially balancing surface heat fluxes.

Our results also suggest that the evolution of the IFF in winter will most likely be characterized by both mixed layer eddies and mesoscale eddies. That is, wintertime conditions will most likely present a complex geography of baroclinic instability with isolated cold-core eddies that detach from the outcropping frontal thermocline and propagate south towards the ridge crest, while at the same time MLEs will grow in regions with deep mixed layers in the presence of baroclinicity. Meandering of the front associated with full-depth baroclinic waves like the ones in the experiments $\{A, B, C\}$, are more likely to be responsible for promoting an increase of deep overflow across the IFR and cross-front exchange of between the North Atlantic and Nordic waters. MLEs, once reaching finite amplitude, are likely associ-

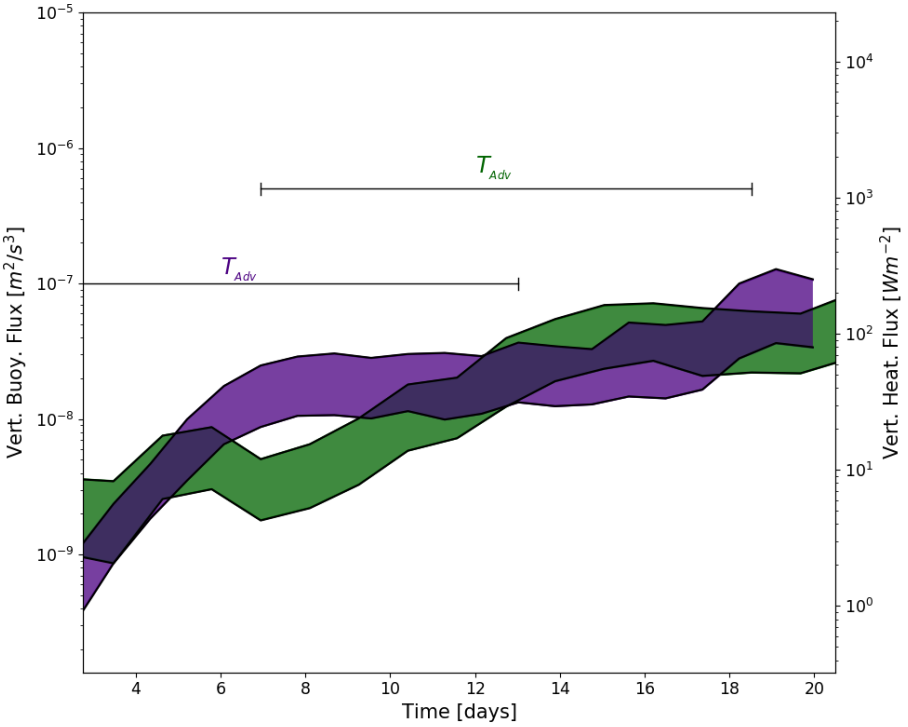

Figure 2.15: Vertical buoyancy flux $\overline{w'b'}$ (left axis) and the equivalent surface vertical heat flux required to change the equivalent amount of buoyancy $c_p\rho_0\overline{w'b'}/g\alpha$ (right axis) for simulation B (green) and B_{ML} (indigo).

ated with lateral stirring of water that promotes cross-ridge spreading of watermass. The rapid MLE growth could make lateral stirring within the mixed layer a dominant mechanism of cross-ridge exchange of surface watermasses, while the meandering of the front remains an important mechanism yearlong for cross-frontal exchange, with implications for bottom overflow transport.

2.6 Limitations and Conclusions

We investigated the effects of bottom topography on the baroclinic instability of an idealized representation of the IFF, motivated by contrasting temperature distributions that represent summer and wintertime conditions. The dynamics of all simulations are eddy dominated,

with two different *regimes* of surface intensified baroclinic instability. The first is a mesoscale instability characterized by a temperature distribution with no surface mixed layer typical of a shallow summer mixed layer as represented in experiments $\{A, B, C\}$, and in which both the slope parameter and depth ratio play a role on the stability of the frontal configuration. We find the greater growth rates for the most destabilizing values of slope parameter experiences by the jet in our study (*i.e.* the less negative γ_{NO}), in accordance to linear stabiity analysis of the modified Eady model. The estimated growth rates decrease as the baroclinic jet moves towards deeper water, hence a increase of the depth ratio as well as the jet experiencing a more negative and therefore less destabilzing slope parameter compared to the other cases considered. Although this points to a good agreement on the expected behavior of growth rates with that of the theory, calculated growth rates where expectedly higher than the ones theory predicts (by a factor of 2).

The second regime is that of a mixed layer instability characterized by MLEs that grow within the mixed layer front that are insensitive to the presence of bottom topography during initial growth of the instability, as represented in experiments $\{A_{ML}, B_{ML}, C_{ML}\}$. Sloping bottom topography does have an effect on these simulations once mixed layer eddies already fully developed, by promoting a faster mesoscale eddy growth when the surface frontal jet sits atop the shallower and less negative bottom topographic slopes. Whether there is significant cross-scale, non-linear energy flux between the mixed-layer and mesoscale modes, we do not address here. A major limitant in our analysis is the periodic domain, which constrains the time integrations, but not the growth rates of the most instable mode are not affected by the length of the channel (we performed additional simulations varying the length of the channel, not shown here). Thus we considered the results up to an advective timescale of the order to 10 days, much smaller that the damping time scale associated with air-sea fluxes, which is on the order of 1 month in high latitudes, which increases for increasing mixed-layer depth [Frankignoul et al., 1998].

Our results show eddy-driven cross-front lateral heat flux that is comparable to that by the mean flow ($\mathcal{H}_{FB}$), the latter depending directly on the temperature jump across the

front (the strength of the geostrophic also depends on the temperature jump ΔT). On the initialization of the experiments, we set the temperature jump $\sim 20\%$ below to those of observational estimates, thus providing a lower bound estimate for $\mathcal{H}_{FB}$, which helps explain a mean heat transport smaller than observational transport estimates. The initial amplitude of the perturbation that seeds the instability is the same for all our experiments, allowing direct comparison between simulations with and without a mixed layer front. The spatial scale of the initial (temperature) perturbation is smallest scale ($\pm 0.2^{\circ}C$ every dx,dy), and by focusing on the initial development of the instability (*i.e.* from small amplitude) up to an advective (residence) timescale, we argue our estimates provide lower bound estimates of the eddy heat transports as a function of time. The maximum of these (lower bound) estimates takes place when the baroclinic eddies have reached a finite amplitude and greatly distort the front, leading to cold-core eddies that pinch off from the front into warmer temperature waters. This greater transports estimates are associated with eddy separation from the front and thus depend strongly on the ΔT across the front.

Another potential limitant for our study is the choice of depth for the mixed layer front. While at high latitudes wintertime mixed layer depth can reach $500m$ (or deeper), the depth of a mixed layer front depends on the presence of baroclinicity and, in the case of the IFF, on the depth of the outcroping pycnocline. In our initial configuration the depth of the mixed layer front has a range of values $100m < h_{ml} < 300m$. It is possible that our simulations underestimate the depth of the mixed layer front, which can potentially affect our results, in particular shift the eddy advective transport estimates to larger values (since mixed layer eddies would be deeper). Thus, again, we argue that our heat transport carculations represent lower bound estimates.

In this study, we find through our estimates that eddy dynamics that arise from the instability of the IFF have the potential to play an important role on lateral heat exchanges across the region south and north of the IFR, with sloping topography playing a crucial role through the slope parameter, whether the initial development of eddies is dominated by mesoscale baroclinic instability, or mixed layer instability.

Chapter 3

ON THE ASYMMETRY OF THE CIRCULATION OF THROUGHFLOWS ACROSS LARGE AMPLITUDE TOPOGRAPHY. PART I: BAROTROPIC CIRCULATION

3.1 Introduction

The exchange of watermasses across ocean basins through a gap (a *strait*) and a sill can exert a control on the circulation downstream due to net fluxes of heat, salt and momentum. For example, the inflow of Atlantic water into the Nordic basins across the Greenland Scotland Ridge (GSR) provides heat fluxes that precondition for deep convection and water-mass transformation [Hansen and Østerhus, 2000, Østerhus et al., 2005, Hansen et al., 2008, Bringedal et al., 2018]. Moreover, localized dissipation as the inflow navigates the GSR can potentially affect the circulation of the inflow downstream, as the throughflow must balance large scale constraints on mass, energy and momentum [Yang and Price, 2007].

The dynamics of throughflows across straits and sills has an exhaustive literature, with most of the efforts in providing insight into the linkage between the net volume (mass) flux across basins through a strait or sill, and upstream oceanographic properties [Gill, 1977, Whitehead et al., 1974, Pratt and Lundberg, 1991, Helfrich and Pratt, 2003]. The vast majority of idealized models, however, assume uniform potential vorticity flows, where Kelvin wave dynamics determine the pressure field [Gill, 1976, Pratt, 1983, 1984, Whitehead, 1995], thus neglecting Rossby wave dynamics that can significantly change the pressure field and flow pattern beyond that determined by Kelvin waves [Hermann et al., 1989]. Uniform potential vorticity dynamics is then an approach most suitable for flows across *narrow* gaps (channels), characterized by a cross-sectional width of the order of (or smaller than) the deformation radius $L_{_D} = NH/f$ where H is the water depth, f the Coriolis parameter, and

$N^2 = \partial b/\partial z$ the buoyancy frequency, a measure of vertical stratification (vertical variation of buoyancy b).

In this paper we examine the circulation associated with equilibrated, uniformly rotating channel throughflows across a large amplitude symmetric ridge. We consider a *wide* channel geometry $(0 < x < L) \times (0 < y < M)$, with $M > L > L_D$, where the ridge intersects lateral walls at $x = 0$ and $x = L$. We force the circulation with a laterally uniform northward flow across the ridge by imposing inflow/outflow conditions far upstream/downstream from the ridge, in a way that the forcing results in a net zero barotropic vorticity flux, equivalent to the conservation of mass.

The imposed inflow/outflow configuration implies, under linear quasigeostrophic dynamics [Hallberg, 1997], that the forced flow will result in a combination of the imposed flow, plus the circulation induces by bottom trapped topographic Rossby waves that can only propagate *pseudo* westward along topographic contours, where they become arrested by the presence of the wall. Thus, the thoughflow (flow along the ridge that connects upstream with downstream imposed conditions) is characterized by boundary currents and given a symmetric ridge topography, the circulation associated with the boundary currents and thus the flow pattern across the ridge (*i.e.* the throughflow) will be symmetric with respect to the ridge crest. Nonlinear modification by eddies, bottom frictional effects that are localized to solid boundaries [MacCready, 1994, Benthuysen and Thomas, 2012], may exert a local modification to the throughflow as it navigates topography, thus exert a control on the character of the flow downstream.

The question then is how does the equilibrated throughflow satisfy the large scale constraints imposed of the circulation given local a modification by processes localized to the ridge. The large scale constraints imposed by the forcing and bottom topography precondition for an asymmetric behavior of the barotropic circulation across topography, through a modification of the stratification localized to boundary currents. We test this by analyzing nonlinear simulations of the primitive equations (see table 3.1 for parameters associated with boundary currents).

This f-plane model differs from zonal β-plane channels models (*e.g.* MacCready and Rhines [2001], Hallberg and Gnanadesikan [2001]), in that in our model the mean net transport is perpendicular to the Rossby waveguides atop the ridge that intersect lateral walls, and thus strongly depends on recirculation patterns associated with boundary currents, to connect between upstream and downstream flow conditions.

This model is based as an idealization of the flow of Atlantic water into the Nordic Seas that gets *funneled* to cross the shallow, large amplitude Iceland-Faroe Ridge (IFR), the widest and shallowest gap of the Greenland Scotland Ridge (GSR). Characteristics of the flow around the IFR are that it is largely driven by large scale, surface sea level gradient across the ridge [Hansen et al., 2010], a standing anticyclonic meander atop the ridge crest that can results in upwelling of cold deep overflow waters from south of the ridge crest [Prater and Rossby, 2005], and, lastly, that the Atlantic inflow downstream from the ridge becomes greatly topographically steered, an apparent change on the barotropic structure of the flow after navigating across the GSR.

A clear disadvantage of our model is the absence of the subpolar frontal expression of the IFR maintained by the confluence of Atlantic waters with the East Icelandic Current [Beaird et al., 2016], a current whose flow pattern, stratification and watermass composition are a result of freshwater and surface buoyancy fluxes that are set at the basin scale [Hansen and Østerhus, 2000, Jónsson, 2007]. Our objective is to provide a simplified model that incorporates large scale and localized processes to bottom topography that can exert control on the flow as it navigates topography, the basis to built upon when considering more complex, convectively driven exchanges across topographic obstacles.

Our approach to relate our model to the Atlantic inflow is motivated by the success of barotropic models in describing the basin circulation patterns that are observed at high latitudes on the Nordic seas [LaCasce et al., 2008, Nøst et al., 2008], as well as observational evidence that show strong topographic steering of the Atlantic inflow as it circulates the IFR [Beaird et al., 2016].

The outline of this paper is as follows. In the next section, we provide the basic theoretical

framework for understanding large scale constraints on the throughflow and the potential local modification by frictional effects that apply to our model. In section 3 we analyze simulations, relating observed asymmetries on the circulation of equilibrated simulations with the effect of eddies and bottom friction. Lastly, in section 5 we summarize our results and discuss implications for large scale throughflows across large amplitude topography.

3.2 Model Configuration

We use the Regional Ocean Modelling System (ROMS) that solves the primitive equations using a terrain-following vertical coordinate [Shchepetkin and McWilliams, 2005], with a high order approximation to the vertically integrated pressure gradient force term in the momentum equations consistent with energy and momentum integral conservation laws [Song and Wright, 1998]. The resolution in the vertical grid spacing varies as a function of the distance from the ridge, and the top and bottom boundaries. We use 40 vertical levels that allow for a maximum resolution of $dz \approx 3$ m near the sea surface and ocean bottom over the ridge crest, and a minimum resolution of $dz = 32$ m at intermediate depths, away from ridge topography and vertical boundaries. The horizontal resolution is constant, with $\Delta x = 1$ km and $\Delta y = 2$ km. The inflow and outflow are relaxed towards a background stratification $N_0^2 = 1 \times 10^{-5} s^{-2}$ every 5 days, decaying linearly 10 gridpoints into the interior. A sponge layer is also applied within the nudging region to further bring the boundary condition to that of the imposed inflow/outflow. The model is forced by a lateral volume influx of $Q_{in} \approx 3$ Sv (1 Sv=$10^6 m^3 s^{-1}$), an outflow Q_{out} of equal magnitude, and an advective barotropic vorticity flux potential magnitude $\mathbf{J}_{_A} = H_0 v_0 f \hat{\mathbf{j}} \approx 1.5 \times 10^{-3} m^2 s^{-2}$ at both the inflow and outflow locations.

The model uses quadratic bottom drag with drag coefficient $C_D = 2.5 \times 10^{-3}$, a background vertical viscosity of $A_{k_0} = 10^{-3} m^2 s^{-1}$, and we implement the KPP parameterization for (nonlocal) vertical mixing [Large et al., 1994]. Lateral dissipation of momentum is implemented through a harmonic viscous dissipation. Each simulation is ran for 7 years, of which the first 12 months represent the spin up, a short time due to the strongly barotropic

nature of the simulations. The analysis takes place 50km away from the nudging regions, localized to northern and southern open boundaries. We consider both free-slip and no-slip tangential boundary conditions resulting in the flow configurations which flux momentum laterally (no-slip), or not (free-slip), across lateral walls.

We vary the viscosity coefficient A_H for each different experiment, thus varying the width of the lateral boundary currents given by the scaling $\lambda_M = (A_h/\beta_T)^{1/3}$, where $\beta_T = (f/h^2)dh/dy$ is the topographic beta (Table 2.1). We measure the non-linearity of the (lateral) boundary currents through the (bottom) boundary current Reynolds number $Re = V_{max}\lambda_M/A_H$, a measure of the relative thickness of boundary layer and the role of inertial terms against viscous dynamics.

3.3 Theoretical Framework

3.3.1 Boundary currents: The large scale constraint on the circulation

The equation for the evolution of the *Barotropic Vorticity* ($\Omega = \nabla_h \times <\mathbf{u}_h>$, where $<\cdot>$ represents vertical integration and $\mathbf{u}_h$ is the horizontal velocity vector) is given by

$$\frac{\partial \Omega}{\partial t} = \frac{\partial(B_{bot}, h)}{\partial(x, y)} - \underbrace{\nabla_h \cdot \mathbf{J}_{\Omega_A}}_{\text{Advective}} + \underbrace{\nabla_h \times \mathbf{J}_{\Omega_{NA}}}_{\text{Dissipative}} \tag{3.1}$$

where the advective ($\mathbf{J}_A$) and dissipative ($\mathbf{J}_{NA}$) barotropic vorticity fluxes in the primitive equations are found by integrating the horizontal momentum equations in the vertical and then taking the curl (see derivation in Appendix B). The first term on the right hand side of (3.1) represents the bottom Bernoulli torque $B(z = -h) = B_{bot}$, with $B = (1/2)\mathbf{u}_h^2 + g(\eta - z) + p/\rho_0$ where η is the surface elevation and p the hydrostatic pressure due to stratification.

The barotropic vorticity fluxes in (3.1) are

$$\mathbf{J}_{\Omega_A} = <\mathbf{u}_h\,(f + \zeta)> - <[w\boldsymbol{\omega}_a]_h> \tag{3.2}$$

$$\mathbf{J}_{\Omega_{NA}} = <\mathbf{F}_h> + \left(\frac{\boldsymbol{\tau}_s - \boldsymbol{\tau}_{bot}}{\rho_0}\right) \tag{3.3}$$

Table 3.1: Parameters relevant to lateral boundary currents. For stratified simulations, variables are vertically averaged within 100m from the bottom, localized to boundary currents, given the bottom intensified nature of the flows in all stratified simulations.

Experiment	$A_H\ [m^2 s^{-1}]$	$N_0^2[s^{-1}]$	$\lambda_M\ [km]$	$\overline{V}_{bot}[ms^{-1}]$		$\lvert Ro\rvert_{bot}$		Re		N^2_{bot}	
				WBC	EBC	WBC	EBC	WBC	EBC	WBC	EBC
A_{fs}	2500	$--$	79.4	0.45	0.345	0.05	0.04	14.3	10.96	–	–
A_{ns}	2500	$--$	79.4	0.24	0.22	0.02	0.02	7.62	6.99	–	–
Ast_{fs}	2500	10^{-5}	79.4	0.20	0.28	0.15	0.09	3.81	8.26	3.06	1.04
Ast_{ns}	2500	10^{-5}	79.4	0.11	0.17	0.08	0.05	2.86	4.76	3.07	0.87
B_{fs}	250	$--$	36.8	0.84	0.48	0.18	0.1	123.6	70.7	–	–
B_{ns}	250	$--$	36.8	0.54	0.43	0.12	0.09	79.5	63.3	–	–
Bst_{fs}	250	10^{-5}	36.8	0.47	0.47	0.45	0.16	41.2	66.24	2.39	0.85
Bst_{ns}	250	10^{-5}	36.8	0.24	0.36	0.18	0.12	26.5	53	2.82	0.83
C_{fs}	25	$--$	17.1	0.94	0.48	0.44	0.22	643	328.3	–	–
C_{ns}	25	$--$	17.1	0.78	0.65	0.36	0.31	533.5	444.6	–	–
Cst_{fs}	25	10^{-5}	17.1	0.47	0.62	0.72	0.17	218.9	478.8	2.63	0.87
Cst_{ns}	25	10^{-5}	17.1	0.32	0.39	0.28	0.91	164.2	321.5	2.2	0.7

Ast_{fs}, Ast_{ns}: Stratified simulation A performed using *free slip* and *no slip* tangential boundary condition. A_{fs} refers to homogeneous (single density) simulation A using *free slip* boundary condition.

WBC, EBC: Value calculated for the western/eastern boundary current, respectively.

Here, $\mathbf{u} = \mathbf{u}_h + w\hat{\mathbf{k}}$ is the 3D velocity vector, $\omega_a = (v_z, u_z, f + \zeta)$ is the absolute vorticity vector. $\mathbf{F}_h = A_h \nabla^2 \mathbf{u}_h$ and $\boldsymbol{\tau}$ represent the (horizontal) viscous dissipation of momentum, and the momentum stress imparted at the surface or bottom. The term $[w\boldsymbol{\omega}_a]_h = w(-v_z, u_z)$ is the horizontal component of the vertical advection of absolute vorticity, and arises from the assumptions within the primitive equations (see Appendix B).

To better understand the how the balance (3.9) describes cross-slope flows, we introduce a quasigeostrophic scaling ($Ro = U/fL \ll 1$) for the throughflow. $\overline{\mathbf{u}}_h$. $(x, y) \sim L$, $z \sim H$, $(\overline{u}, \overline{v}) \sim U$, $\overline{w} \sim (HU/L)$, $g\overline{\eta} \sim fUL$, $\overline{p} \sim \rho_0 UfL$ and $h = H(1 - Ro\eta_b)$, where $\eta_b = \delta h/H$ is a linear function of y. Furthermore, $\mathbf{u}_h = \mathbf{u}_h^{(0)} + Ro\mathbf{u}_h^{(1)} + O(Ro^2)$ and $w = Row^{(1)} + O(Ro^2)$. Then, assuming dissipation of momentum is purely horizontal, the barotropic vorticity fluxes are

$$\overline{\mathbf{J}}_{\Omega_A} = UfH\left[\overline{\mathbf{u}}_h^{(0)} + Ro\left(\overline{\mathbf{u}}_h^{(0)}\overline{\zeta}^{(0)} - \overline{\mathbf{u}}_h^{(0)}\eta_b + \overline{\mathbf{u}}_h^{(1)}\right) + O(Ro^2)\right] \tag{3.4}$$

$$\overline{\mathbf{J}}_{\Omega_{NA}} = \frac{A_H U}{L^2}\nabla^2\left(\overline{\mathbf{u}}_h^{(0)} + Ro\overline{\mathbf{u}}_h^{(1)}\right) + O(Ro^2) \tag{3.5}$$

We have approximated the vertical integrals by their mean values *e.g.* $<\overline{\mathbf{u}}_h> = H\overline{\mathbf{u}}_h(1 - Ro\eta_b)$ where now $\overline{\mathbf{u}}_h$ represents the vertical average. This further implies $\overline{\Omega} = H\overline{\zeta} + O(Ro)$. The error in these approximation are included in the $O(Ro^2)$ correction terms in (3.4). Given the scaling for sloping bottom, all terms associated with the first term in (3.1) are $O(Ro)$. Thus, the $O(1)$ balance in dimensional form is given by

$$\frac{Qf}{H}\nabla \cdot \overline{\mathbf{u}}_h^{(0)} = \frac{A_H U}{L}\nabla^2\overline{\zeta}^{(0)} \tag{3.6}$$

where $Q = UHL$ is volume transport. The balance in (3.6) in the differential form of the integral constrain derived by [Yang and Price, 2000], and states that a recirculation (rhs of 3.6) is required to allow mean quasigeotrophic, interior (outside boundary layer), cross- slope flows (lhs of 3.6). Thus, a throughflow with net transport upslope ($\nabla \cdot \overline{\mathbf{u}}_h^{(0)} > 0$) requires an

anticyclonic recirculation $\overline{\zeta}^{(0)} < 0$ so that $\nabla^2\overline{\zeta}^{(0)} > 0$. Similarly, a throughflow with a net downslope transport requires a cyclonic recirculation (positive torque).

Recirculation across f/H contours implies the formation of boundary currents, with the orientation of the boundary current given by the sign of the barotropic PV gradient ($\beta_{_T} = \partial_y(f/H)$). Flow up the slope has $\beta_{_T} > 0$, thus westward intensification results in an anticyclonic boundary current. Flow down the slope, on the other hand, promotes a *pseudo-westward* intensification and thus the formation of a cyclonic boundary current at an eastern wall. The case of a throughflow across a symmetric (large amplitude) ridge, the crest acts as a *pseudo-north pole*, with an anticyclonic boundary current south of the crest, a cyclonic boundary current north of the crest, both localized to sloping topography (Fig. 3.1). A powerful result from simple linear dynamics.

Scaling analysis of (3.6) provides a relative magnitude of the terms involved in the balance. This is, in order for the leading order balance to remain valid, we must have

$$\frac{Qf}{H} \sim \frac{A_{_H}U}{L} \tag{3.7}$$

In the case of cross slope flows, (3.7) implies that a reduction of H (shallow water) while keeping the transport constant, implies an increase in the relative vorticity $Ro = U/L$ of the mean flow, with $A_{_H}$ fixed. The mean flow can then become unstable to hydrodynamic instabilities. I in the limit $Ro \sim O(1)$ dynamics within the bottom boundary layer, left apart from the discussion so far, have the potential to induces rapid re(de)-stratification of the interior flow outside the bottom boundary layer [MacCready, 1994, Benthuysen and Thomas, 2012] and thus exert a control on the mean circulation, given that the throughflow must still conserve global constrains on mass, momentum and circulation. In this limit, however, higher order terms must be included, as well as separate equations for the dynamics within the bottom boundary layer coupled to the interior.

The validity of the $O(1)$ balance in (3.6), then, comes into question. as it requires $A_h H \gg Q$ for a quasigeostrophic scaling $Ro \ll 1$. Typical values of $Q \approx 1Sv$ ($1Sv = 10^6 m^3/s$) and $H = 1000m$, $A_{_H} \gg 10^3 m^2/s$. The scaling analysis implies that the throughflow scales with

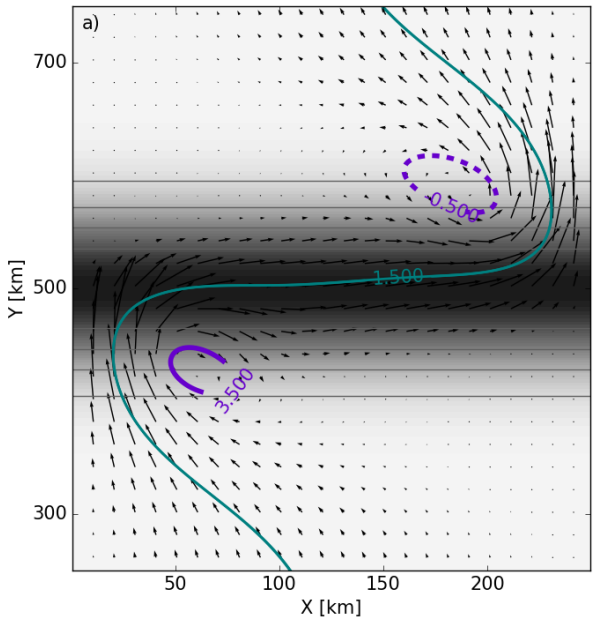

Figure 3.1: (a) Steady barotropic circulation of a homogeneous (single density), viscous simulation (A_{ns}, see Table 3.1), driven by the advective barotropic vorticity flux $\mathbf{J}_A = v_0 H_0 f \hat{\mathbf{j}}$ specified as equal upstream/downstream boundary conditions. Black arrows represent the (time-mean) surface velocity field, and the greyscale shows the location of the ridge. The path of the throughflow ($0 \leq \psi \leq 3$ Sv, 1Sv$= 10^6 m^3 s^{-1}$), is depicted by $\psi = 1.5$Sv (teal contour). The throughflow induces a cyclonic $\psi = -0.5Sv$ (dashed indigo) and anticyclonic $\psi = 3.5$ (solid indigo) recirculation (torques) across the ridge crest. Torques of equal magnitude across the ridge crest imply the vanishing of the area integral of each term of the rhs of (3.1).

the width of the sloping bottom, since the flow pattern and thus pressure field is determined by topographic Rossby waves, and that such length scale applies also to the recirculating region. Thus, for a sill with a half-width $L = 100km$, a depth change of $dh = 500$m, and $f = 1.25 \times 10^{-4}$, $\beta_{_T} = 2.5 \times 10^{-12} m^{-2} s^{-1}$, $A_{_H} = 1000 m^2 s^{-1}$ imply $\lambda_{_M} \approx 75km$. Thus confirming that the validity of the quasigeostrophic, viscous balance (3.6) requires a scaling in which both the throughflow and the width of the boundary current $\lambda_{_M}$ scale similarly.

3.3.2 Bottom boundary layer dynamics: Localized modification

Bottom friction acts to slow down the flow by draining fluid through the bottom boundary layer, resulting in a net transport within the bottom boundary layer at left angles to the flow [Pedlosky, 2013a]. Thus, depending on the orientation of the mean (interior) flow with respect to f/H contours, bottom friction can lead to an Ekman transport across f/H contours, rapidly modifying the stratification of the boundary layer and even the upper ocean if such advection results in a convectively unstable stratification [Condie, 1995, Wåhlin and Walin, 2001, Brink and Lentz, 2010].

The evolution of the bottom boundary layer can be represented as a two timescale process, which results in net transport of within the bottom boundary layer, and the buoyancy shutdown which leads to an Ekman arrest, where the baroclinicity of the bottom boundary layer reduces the effects of the bottom boundary layer onto the mean interior flow [MacCready and Rhines, 1991, Trowbridge and Lentz, 1991, MacCready and Rhines, 1993]. The relative importance of each term in a limited domain such as a channel flow in which f/H contours intersect walls, depends in the relative timescales in which the along-slope flow navigates f/H ridge topography.

The timescale at which buoyancy forces balance an (initial) up/down-slope Coriolis force is given by the buoyancy shutdown timescale, defined as $\mathcal{T}_{shut} = P_r^{-1} S^{-2} f^{-1}$, valid for $S \ll 1$ where $S \approx (N\theta/f)^2$ with $\theta \approx dh/dy$ is (*small angle*) slope Burger number, Pr=A_ν/A_κ is the Prandtl number (usually $Pr \sim O(1)$). Thus, buoyancy shutdown requires a sloping bottom, with the timescale $\mathcal{T}_{shut} \to \infty$ as the mean flow approaches flat bottom or a ridge crest.

The stratified frictional spindown time scale is given by $\mathcal{T}_{spin} = E^{-1/2} f^{-1}$, where $E = 2A_\nu/fH_p^2$ is the Ekman number and $H_p = fL/2\pi N$ the Prandtl depth, the depth scale over which anomalies penetrate into the interior. The inertial and diffusive time scales are expressed as $\mathcal{T}_{inertial} = f^{-1}$ and $\mathcal{T}_{diffusive} = E^{-1} f^{-1}$. A summary of these scales is given in Table 3.2 which applies to all stratified simulations.

From linear arguments, we expect the throughflow as it navigates a symmetric ridge, to

flow along f/H contours at or near ridge crest, where $\beta_{_T} = 0$, with the mean flow along f/H contours where $\theta \to 0$ after separation from the west ($x = 0$) wall. This implies that along the ridge the buoyancy shutdown timescale is much larger than, say an advective time scale along the ridge (see Table 3.2). Thus, in our model, frictional effects that apply to along-slope flows will largely be determined by the frictional spindown of the along-slope current, although localized to the boundary current, advection of buoyancy within the bottom boundary layer may still be important. Thus, depending on the near bottom distribution of temperature as regulated by the equilibrated throughflow, bottom boundary layer dynamics can precondition for differences on circulation and stratification downstream from the ridge, when compared to upstream conditions.

3.3.3 Integral balances: Cross-ridge barotropic vorticity balance

In order to diagnose topographic constrains on the circulation (*i.e. form drag* across the ridge) across a large amplitude zonally symmetric $h = h(y)$ ridge topography, we integrate the equation for the barotropic vorticity equation (3.1) along f/H contours, since f/H contours are parallel to the east-west (x) direction. The integral of (3.1) over a control area centered around the ridge crest (and away from upstream/downstream inflow/outflow boundary conditions where numerical relaxation takes place), is given by

$$\iint \frac{\partial(\overline{B}_{bot}, h)}{\partial(x,y)} dA - \oint (\overline{\mathbf{J}}_{\Omega_A} \cdot \hat{\mathbf{n}})\, dl + \oint (\overline{\mathbf{J}}_{\Omega_{NA}} \cdot \hat{\mathbf{s}})\, dl = 0 \tag{3.8}$$

where the overbar $\overline{(\cdot)}$ represents a time average, $\hat{\mathbf{n}}$ and $\hat{\mathbf{s}}$ represent the normal and tangential vectors to the boundary (following a cyclonic orientation). Then the integral balance can be written as a northward integral in which the integrands of each term represents the along-slope integration of the sources of barotropic vorticity Ω. This is, integrating (3.8) only in x yields

$$\int \frac{\Delta_x \overline{p}_{bot}}{\rho_0} \frac{dh}{dy}\, dy + \int \Delta_x \overline{E} \frac{dh}{dy}\, dy - \int \Delta_x (\overline{\mathbf{J}}_{\Omega_A} \cdot \mathbf{i})\, dy + \int \Delta_x \left(\overline{\mathbf{J}}_{\Omega_{NA}} \cdot \mathbf{j}\right)\, dy = 0 \tag{3.9}$$

Table 3.2: Parameters associated with bottom boundary layer dynamics, arising on the region away from the influence from lateral boundary currents, along f/H contours atop the ridge, in all our simulations. The region is defined laterally as $\lambda_M < x < 250 - \lambda_M$. Values represent an average over this region.

Parameter	Description	Value
θ	(small angle) topographic slope	0.002
A_ν	Vertical mixing coefficient	$\approx 5 \times 10^{-3}[m^2 s]$
A_κ	Vertical diffusivity coefficient	$\approx 5 \times 10^{-3}[m^2 s]$
N_c^2	Buoyancy frequency at ridge crest	1.3×10^{-5} $[s^{-2}]$
S	Slope Burger number $S = (\theta N_c/f)^2$	0.003
H_p	Prandtl depth	$55[m]$
E	Ekman number	0.026
P_r	Prandtl number	≈ 1
$\mathcal{T}_{shut}$	Buoyancy shutdown timescale	8360 [days]
$\mathcal{T}_{spin}$	Spindown timescale	0.57 [days]
$\mathcal{T}_{diff}$	Diffusive timescale	3.5 [days]
$\mathcal{T}_{adv}$	Advective timescale	3.8 [days]
$\mathcal{T}_{inertial}$	Inertial timescale	0.58
δ_{Ek}	Ekman layer thickness	9 $[m]$
δ_T	Diffusive boundary layer thickness	55 $[m]$
ω_{bbl}	Eddy forcing frequency	2.31×10^{-6} $[s^{-1}]$

where $\Delta_x(\cdot) = (\cdot)\big|_{x=L} - (\cdot)\big|_{x=0}$ is the cross-channel difference, $\overline{p}_{bot} = p(z = -h)$ is the mean bottom pressure, and $\overline{E} = (1/2)|\mathbf{u}_h|^2$ is the *free*-slip along wall mean kinetic energy (since the term is non-zero only in free-slip simulations). The balance (3.9) results from having the equal northward and southward barotropic vorticity fluxes (*i.e.* uniform inflow/outflow), so that the balance only involves meridional (cross-ridge) integrals. By having the barotropic vorticity balance integrated along f/H contours, we can diagnose the relative contribution to each of the terms in (3.9) associated with each boundary current to the spatial integral of the evolution of the barotropic vorticity (3.1).

The usefulness of the barotropic vorticity comes from the ability to include the bottom pressure forces (form drag) that results from the presence of uneven bottom topography and that are associated with inertial forces across a topographic obstacle. The first term in (3.9), represents the bottom pressure torque and it derives from the twisting force that the bottom topography exerts on the flow. Moreover, through geostrophy, $\Delta_x\overline{p}_{bot} > 0$ implies a net northward geostrophic transport and therefore the integrand of the first term in (3.9) is negative for a net upslope and positive for a net downslope geostrophic transport (see Fig. 3.2).

The integrand of last term in (3.9), associated with the dissipation of momentum induced by boundary currents, is positive for an anticyclonic boundary current and negative for a cyclonic boundary current (since $\mathbf{F} \propto v_{xx}\hat{\mathbf{j}} \propto -v\hat{\mathbf{j}}$, with $v > 0$). The relative location each integrand with respect to the ridge crest, and relative magnitude can provide insight into the location of the net cross slope transport with respect to the ridge crest and, therefore, the relative magnitude of form drag forces on the flow across the ridge crest, that is the required inertia to promote cross-slope flows.

3.4 Results

In this section we evaluate the spatially integrated balance in (3.9) on the simulations described in Table 3.1. We begin by considering a linear ($Ro \ll 1$), viscous ($A_{_H} = 2500m^2s^{-1}$), homogeneous (steady) control simulation characterized by a boundary current scaling $\lambda_{_M} =$

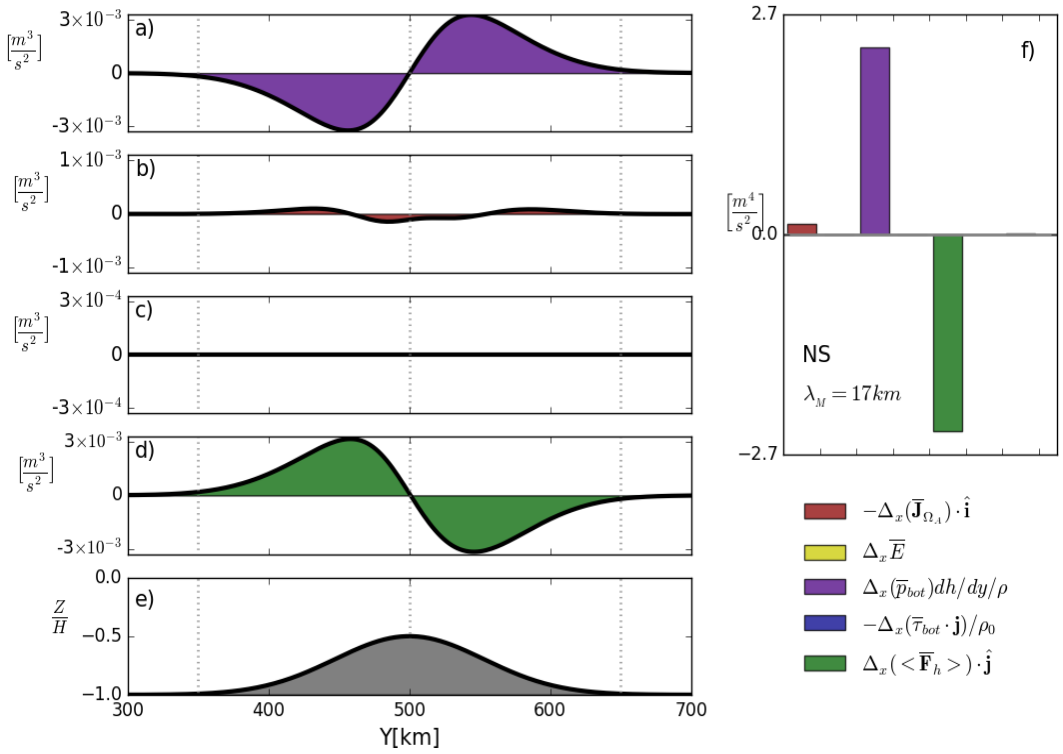

Figure 3.2: a-d) Integrands of the terms in the integral (barotropic) vorticity balance (3.9), collapsed along f/H contours to reflect the distribution of each term across the ridge. The color code is located at the bottom right. The area under the curve for each term is the net contribution to the integral balance. f) Net integral balance for all terms (area under the curve) in (3.9).

$80km$ (see Table 3.1 for other parameters for control simulation A_{ns}). In the following interpretation of the simulations, we will refer to linear simulations those for which the QG, viscous scaling characterizes the flow. This is, $Ro \ll 1$ and simulations where the width of the boundary currents $\lambda_{_M} > 50$km. We are most interested in the differences between linear ($\lambda_{_M} = 79$km) and non-linear ($\lambda_{_M} = 17$km), stratified simulations.

The throughflow of the control simulation ($\lambda_{_M} = 80km$, no-slip, $N^2 = 0$) is characterized by an anticyclonic boundary current as the throughflow moves upslope, facilitated by a recirculation (Fig. 3.1, see $\psi = 3.5$Sv at x=70km, y=400). Similarly, along the downslope, the mean thoughflow develops into a cyclonic boundary current that is facilitated by a

cyclonic recirculation (Fig. 3.1, see $\psi = -0.5$Sv at x=180km, y=550). Near the ridge crest, the flow mostly follows topographic contours. Given the large values of viscous dissipation $A_{_H}$, some of the recirculating streamlines go through the viscous boundary layer (Fig. 3.1, at y=450km, and at y=600km).

Applying the integral balance in (3.9) to the control simulation results in a balance between the spatially integrated bottom pressure torque and net dissipation of momentum associated with lateral boundary currents (Fig. 3.2f). This is,

$$\int \frac{\Delta_x \overline{p}_{bot}}{\rho_0} \frac{dh}{dy} dy + \int \Delta_x \left(<\overline{\mathbf{F}}_h> \cdot \mathbf{j} \right) \, dy = 0 \tag{3.10}$$

where we have found that dissipation of momentum can be well approximated as $\mathbf{J}_{\Omega_{NA}} \approx <\mathbf{F}_h>$ (this will be true for all our simulations).

The net positive value of the first term in (3.10) implies that the throughflow requires more inertia (stronger torque) to flow down the slope downstream from the ride crest, compared to that required by upstream from the ridge crest (fig 3.2f). Such inertial acceleration (*i.e.* a stronger torque) balanced by momentum dissipation is analogous to flows across topography along narrow channels in the presence of critical conditions [Baines, 1998, Pratt and Whitehead, 2007].

Given that the simulation is unstratified, and the requirement of conservation of mass (transport) by the throughflow, the observed difference in required torque across the ridge crest must be associated with the relative location of the boundary currents. Given that $<\overline{\mathbf{F}}_h> \propto -v\mathbf{j}$ at the wall, then by looking at the extrema of the curve associated with dissipation of momentum (Fig. 3.2d) shows the anticyclonic boundary current is located closer to the ridge crest, where $|dh/dy|$ is smaller for a symmetric ridge with a continuously varying slope.

We now apply the spatially integrated balance (3.9) to all simulations, where we observe some similarities and some differences between stratified and unstratified simulations (Fig. 3.3a is the reference simulation). First, all simulations show a *stronger torque* downstream from topography, where the cyclonic boundary current dissipates more momentum when

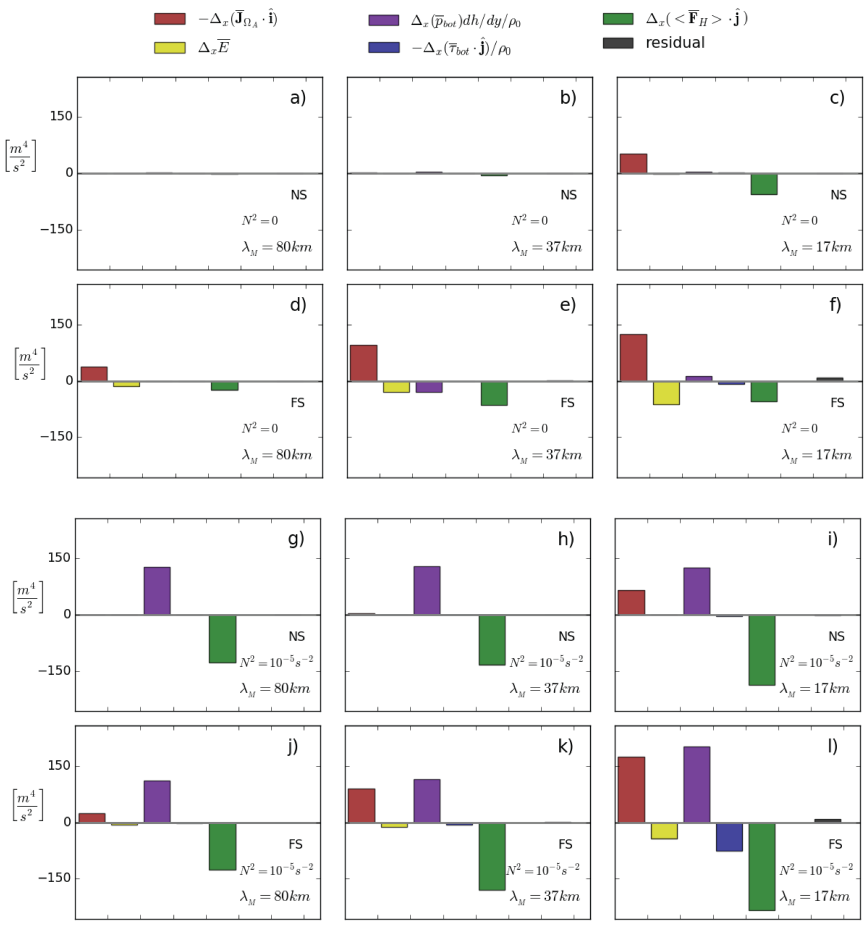

Figure 3.3: Barotropic vorticity balance for all simulations. a-f) Homogeneous simulations ($N_0^2 = 0$), g-l) stratified simulations.

compared to the anticyclonic boundary current, upstream from the ridge.

All free slip simulations are stable to barotropic instability due to the condition at the lateral wall of $v_x = 0$, and so the net contribution to the balance in (3.9) by the nonlinear advective flux term $\overline{\mathbf{J}}_{\Omega_A}$ is likely associated with curvature of the path of the throughflow. What processes dominate the contribution of such term is beyond the scope of this study.

In the no-slip simulations, the nonlinear term is associated with eddies, and we see that in the unstratified simulation (Fig. 3.3c), eddies increase the momentum dissipation of the cyclonic boundary current. The increase in momentum dissipation in the presence of eddies

takes into account for the observed increase in net dissipation of momentum of the cyclonic boundary current (Fig. 3.3c) when compared to the other no-slip, unstratified simulations (3.3a-b). Thus the presence of eddies on the mean flow does not imply a greater torque, but rather a local effect.

Gula et al. [2015] found, on their barotropic vorticity analysis a local balance between the nonlinear advective fluxes of barotropic vorticity and the bottom pressure torque associated with a section of the Gulf stream. Such result is likely associated with the orientation of the f/H contours in their realistic model, with respect to the transport streamlines. This is, in their model, the mean flow and eddies were aligned with topographic contours, a case that does not apply the cyclonic boundary current, which dominates the net contribution.

A stark contrast between unstratified and stratified simulations, is the increase in magnitude in the difference between the spatial integral of the bottom pressure torque (*i.e.* the term with $\Delta_x \overline{p}_{bot} dh/dy$) across the ridge in stratified simulations. Compared to the reference simulation (Fig. 3.3a), the magnitude of the dissipative term to the net integral balance (3.9) does not imply stronger boundary currents in stratified simulations, but rather a greater contrast across the ridge crest. Compared to the spatially integrated balance (3.9) of the stratified simulations, the reference simulation can be considered a *symmetric* boundary current system in which the inertial recirculations across the ridge crest have (almost) equal torques (Fig. 3.1).

The presence of stratification on the simulations introduces an asymmetry on the barotropic circulation across the ridge, according to our metric, in all stratified simulations (Fig. 3.3g-l). This is, in all simulations we find a stronger downstream from the ridge crest, implying not only that the cyclonic boundary current dissipates more momentum, but that the net northward (geostrophic) transport across f/H contours experiences greater resistance downstream form the ridge crest, than upstream.

As in homogeneous simulations, we find that free-slip simulations (which are free of eddies), nonlinear fluxes due to curvature effects of the mean path are as important as the difference in form stress. In no-slip, stratified simulations, nonlinear advective fluxes become

relevant only in the non-linear simulation (Fig. 3.3i), which results in an increase in the net dissipation. Since the net dissipation of momentum associated with boundary currents becomes more negative, this implies that non-linear advective fluxes associated with the cyclonic boundary current are responsible for the observed change. This is, as we found in the unstratified no slip simulation (Fig. 3.3c), eddies account for the observed increase in dissipation, which also implies torque remains unchanged as the boundary currents become unstable.

To better understand the observed difference in bottom pressure torque in the stratified simulations, with or without eddies, we will focus mostly in 4 simulations, all no-slip, 2 unstratified with balances shown in fig. 3.3a and fig.3.3c, and 2 unstratified with balances shown in fig. 3.3g and fig. 3.3i.

The behavior of the transport streamline in our four simulations shows great similarity as the simulations becomes nonlinear (λ_M gets reduced) in both unstratified and stratified simulations. This is, there is an intensification of the cyclonic recirculation downstream from the ridge in both stratified and unstratified (Fig. 3.4b,d, when compared to the linear viscous simulations fig. 3.4a,c), in agreement with the integral balance. The inflow pattern as it goes through the symmetric ridge is also similar in all simulations, with an anticyclonic recirculation (boundary current) near the west wall ($x = 0$) and a cyclonic boundary current along the east wall ($x = 250$km), localized to sloping topography. The flow along the ridge away from lateral walls follows f/H contours, east.

The circulation pattern in unstratified simulations with eddies (Fig. 3.4c) has a stronger recirculation downstream from the ridge, when compared to the control simulation (Fig. 3.4a). From our integral balance, we now that the stronger recirculation of the nonlinear unstratified simulation is associated with eddies that detach from the cyclonic boundary current, and flux vorticity into the interior. Such intensification of the cyclonic recirculation can be observed in the non-linear, stratified simulation (Fig. 3.4d), although the process of instability, and the depth of the instability, may be different between the two simulations.

While the circulation pattern associated with the cyclonic boundary current system down-

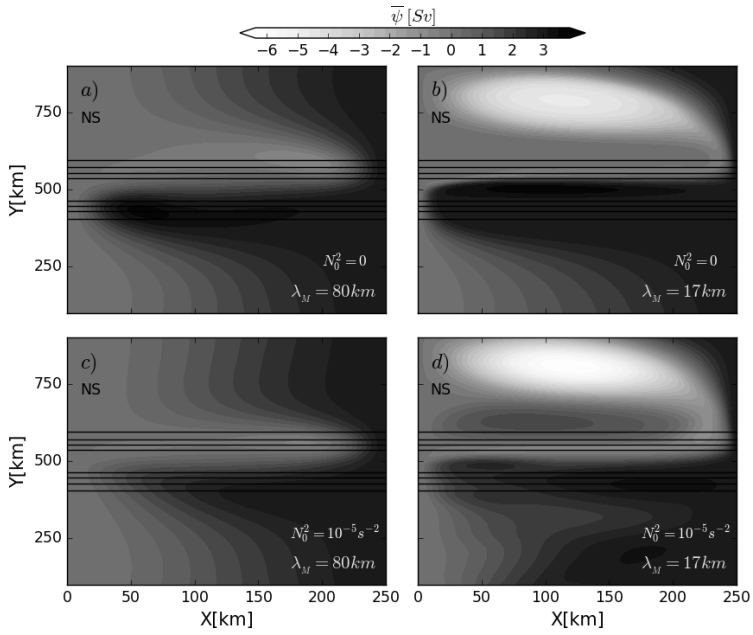

Figure 3.4: time mean transport streamfunction $\overline{\psi}$ showing the barotropic circulation across the ridge comparing unstratified simulations A_{ns} (a) and C_{ns} (b) with stratified simulations Ast_{ns} (c) and Cst_{ns} (d). $\overline{\psi} > 0$ represents both an anticyclonic circulation and northward transport. NS represents no-slip. $\lambda_{_M}$ is a representative of the width of the boundary current, and therefore an indication of viscous forces.

stream from the ridge between the nonlinear, unstratified and non-linear stratified simulations resembles one another, likely associated with barotropization of baroclinic eddies on the stratified simulation, the circulation pattern differs upstream from the ridge crest, between unstratified (Fig. 3.4a and b) and stratified (Fig. 3.4c and d) simulations. The difference being most clear in the viscous simulations with $\lambda_{_M} = 80$km, which we will now discuss.

In the unstratified simulation, the streamline pattern as the flow approaches the ridge, is more focused towards the west wall ($x = 0$, $y = 450$km) in the unstratified simulation (Fig.3.4a), representing the location of the anticyclonic boundary current. In the stratified simulation, the streamline patterns as the northward flow approaches the ridge show a wider extend of the inflow (Fig. 3.4c, y=400km), in agreement with the flow experience lesser

topographic constraint by topography.

In stratified simulations, we find a stronger stratification along the west wall $x = 0$ near the ridge crest (Fig. 3.5a, y=500km), and low stratification at the east wall, downstream from the ridge crest below the 500m isobath (Fig.3.5d, y = 575km). Along the ridge, isotherms are relatively flat, although the tilt of the near bottom temperature surfaces near the west wall at $35<x<100km$ suggests bottom intensified anticyclonic recirculation, centered around x = 50km (black contours in figure 3.5 are the $\overline{T}_1 = 5.7$ and $\overline{T}_2 = 6.2$ isotherms). Such recirculation appears to agree well with an apparent anticyclonic recirculation in the transport streamfunction also centered around x = 50km at the ridge crest (Fig. 3.4d). Near the eastern wall (x>200km), the along ridge stratification suggests downwelling of warm waters (Fig. 3.4c).

The observed difference in stratification along and across the ridge, can help explain the difference in the barotropic behavior of the throughflow, between the cyclonic and the anticyclonic boundary currents. This is because in the f-plane, the circulation around sloping topography is associated with bottom trapped topographic Rossby waves [Rhines, 1970], with a depth scale that is inversely proportional to vertical stratification ($H_R^2 \sim f^2 L_R^2/(N_R^2\pi^2)$, derived from the ratio of the horizontal to vertical (stretching) terms in the f-plane quasi-geostrophic equation $\nabla^2\phi + (f^2/N^2)\phi_{zz} = 0$ where L_R is the scale of the recirculation near the boundary current). Thus, the influence of topographic Rossby waves has a shorter depth scale along the anticyclonic recirculation, when compared to that east along the ridge (see table 3.1 for values of mean vertical stratification atop the ridge at lateral walls). The shallow water depth at and near the ridge enables a strong barotropic (full depth) influence by topographic Rossby waves along the cyclonic boundary current, and a lesser barotropic behavior west, along the anticyclonic boundary current.

The vertical stratification along the west wall implies upwelling of cold waters up the slope (fig. 3.5a) and downwelling of warmer waters down the slope along the east wall (Fig. 3.5d). Fig. 3.6 shows snapshots of relative vorticity above the bottom boundary layer, where the bottom boundary layer thickness layer surpasses 15 meters in regions with strong curvature

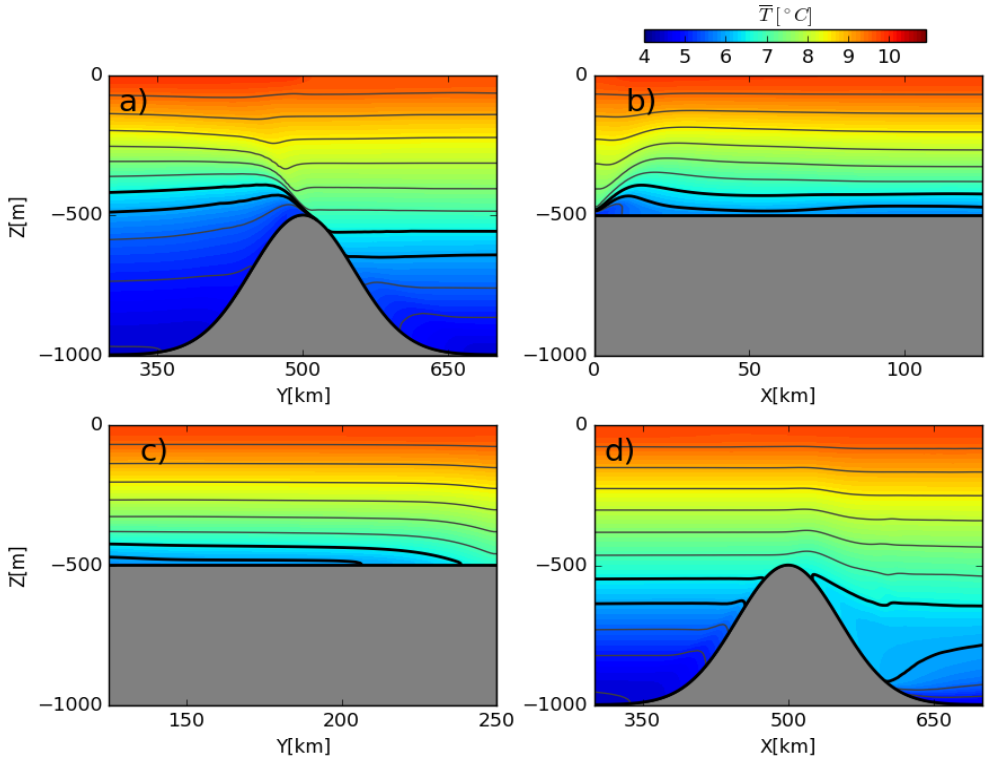

Figure 3.5: Vertical stratification for the nonlinear, stratified simulation Cst_{ns} characterized by $\lambda_{_M} = 17km$ with no-slip boundary conditions. a) Stratification along the western wall ($x = 0$), with b) showing the along-crest stratification a distance of 125km away from the west wall. d) shows the across-ridge temperature along the eastern wall ($x = L$), where c) shows the along-ridge stratification a distance of 125km away from the east wall. Gray contours depicts isotherms every $0.5°; C$ and thick black contours show the location of isotherms $\overline{T}_1 = 5.7° \; C$ and $\overline{T}_1 = 6.2° \; C$

(see Table 3.1). A large standing anticyclone sits atop the ridge crest near the west wall, and is associated with the recirculation of cold waters.

The pattern displayed by an upwelling isotherm south of the ridge crest $\overline{T}_0 = 5° \; C$ (black contours in fig. 3.6a) further sheds light into the bottom pressure distribution. The upwelling isotherm away from the west wall ($x >$ 150km) is aligned with f/H contours, and it shows the broad scale of the cold upwelling, recirculating inflow. The isotherm slowly tilts up the slope westward, feeding the standing anticyclonic meander with cold water (Fig. 3.6a, $x<$100km). The upwelling of cold water masses associated with a bottom intensified meander atop the

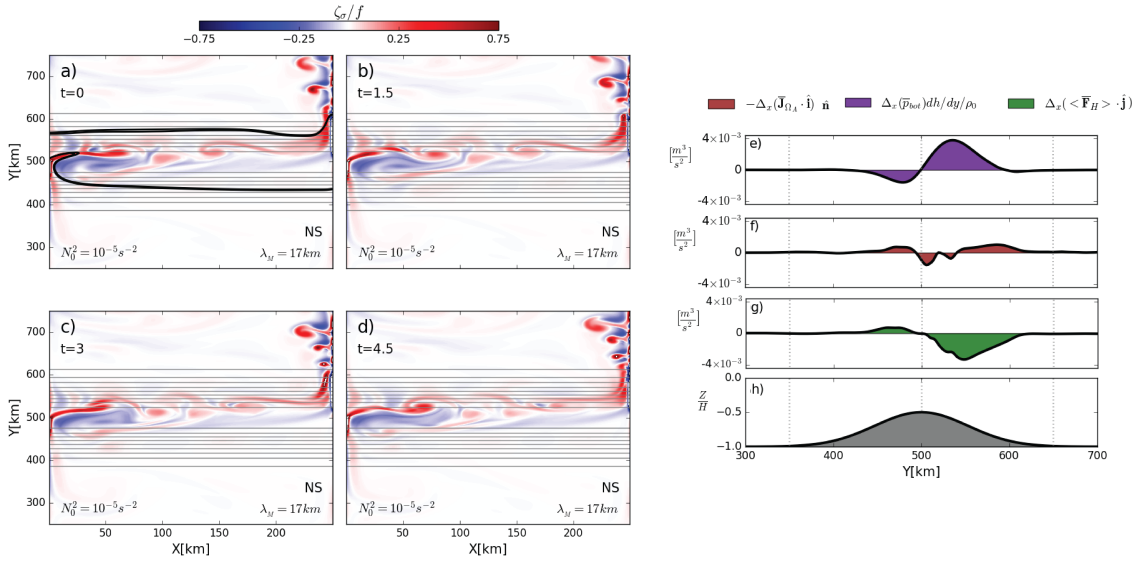

Figure 3.6: a-d) Snapshots of relative vorticity 15m above the terrain for the equilibrated, nonlinear, stratified simulation Cst_{ns}. Eddies from the anticylonic (x=0) boundary current detach every 1.5 days, propagating along f/H contours. The reversal in β_T promotes a strong anticyclonic recirculation near the boundary current at the west wall (x=0, y=500km). Cyclonic eddies decay away from the west wall as they propagate and are advected east, creating the advective vorticity flux in f), localized near the ridge crest. As before, the contribution (area under the curve in f) by the eddies to the integral balance is negative, meaning eddies associated with the cyclonic boundary current (x = 200km, $y >$ 500km) dominate the fluxes, increasing the net dissipative contribution (g).

ridge crest is in agreement with observations of upwelling of drifters along the Iceland-Faroe Ridge, initially set to drift along with the deep overflow plume of the Faroe Bank Channel that navigates along the sloping bottom south of the ridge crest [Prater and Rossby, 2005].

Most of the net upslope transport takes place close to the ridge crest at $y = 450$km, with the strongest mass flux just south of the crest ($y \approx 500$km), where the isotherm becomes parallel to the west wall. There, the topographic slope nearly vanishes, a behavior that results in the smaller integrated bottom pressure torque (Fig. 3.6c). The closer the cross-isobar flow is to the ridge crest where $dh/dy = 0$, the lesser the contribution (area under the curve in fig. 3.6c) to the integral barotropic vorticity balance (3.9). The same bottom isotherm ($T_0 = 5^\circ$ C) suggest that the net downslope transport takes place farther downstream from

the ridge crest, when compared to the location of the net upslope transport, in agreement with the much greater area under the curve in figure (3.6f).

The location of the standing anticyclonic meander (Fig. 3.6a-d, at $y = 500$km) is just upstream of the ridge crest where the topographic β_T changes sign, and flow separates from the wall at $x = 0$. The anticyclonic side of the jet is located near the ridge crest, and feeds the recirculating anticyclonic meander. As a result, only cyclonic eddies break away from the standing meander, and move towards the west wall along f/H contours, advected by the mean flow. Eddies associated with the cyclonic boundary current separate from the current as a train of dipoles that appear to have a stronger cyclonic core, with a greater surface wall area to extract barotropic vorticity when compared to the anticyclonic separating boundary current. The contrasting behavior between the generation sites of eddies, is likely responsible for the difference in momentum flux contribution between the two boundary currents in our balances (area under the curve in figs.3.3c,i).

Despite the complex nature of the nonlinear dynamics involved in the equilibration of the throughflow, the pattern of the circulation, an western intensified anticyclonic boundary current and a *pseudo-westward* intensified cyclonic boundary current at the east wall is in agreement, to first order, with the preferred orientation of topographic Rossby waves. But such dynamics do not completely provide an explanation of the observed differences in stratification, which modify the extent to which topographic Rossby waves influence the upper ocean.

Dynamics within the bottom boundary layer, cannot be ignored, given the observed thickness $\delta_{Ek} \approx 24m$, which reaches a maximum at the location of boundary currents, and along the path of the mean flow roughly along f/H contours (*e.g.* fig. 3.7 shows the calculated bottom boundary layer thickness of the nonlinear simulation. A similar pattern is found for linear viscous simulations). After an initial fast spinup by the topographic Rossby waves which promote the formation of boundary currents, dynamics within the bottom boundary layer become important.

Bottom pressure torque, the leading term in our spatially integrated balance, can be

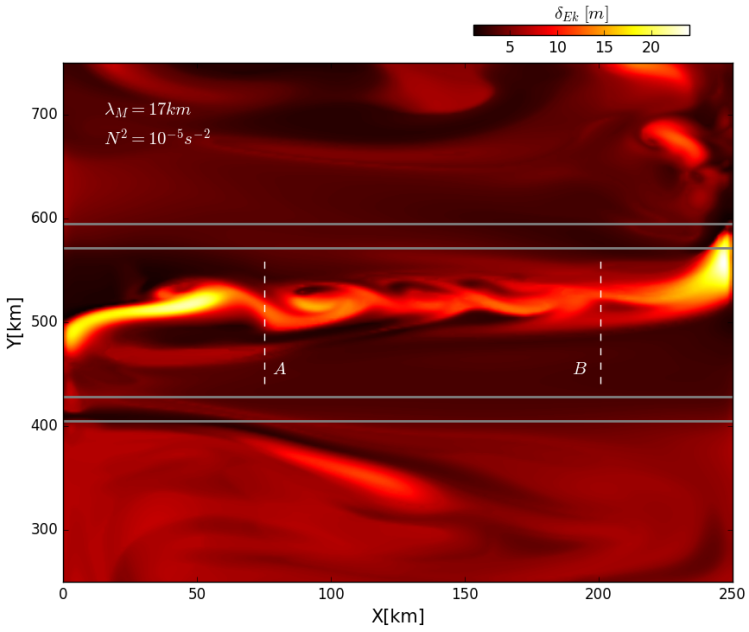

Figure 3.7: Snapshot of thickness of bottom boundary layer in nonlinear stratified (no slip) simulation Cst_{ns} with the greater thickness values associated with the boundary currents. Grey solid lines show the location of the ridge. The spindown of the bottom along-slope current results in downslope flow, downslope migration of bottom intensified current and thus, on the pattern of δ_{Ek}. Dashed white lines A and B span an area where the interior flow is along f/H contours and where downslope transport is associated with bottom Ekman dynamics of the along-slope flow. Net downslope transport over this region contributes to the net force.

approximated to leading order term by the vertical stretching of vortex lines. This is,

$$\frac{1}{\rho_0}\frac{\partial(\overline{p}_{bot}, h)}{\partial(x, y)} \approx -f\overline{w}_{bot} \tag{3.11}$$

where $\overline{w}_{bot}$ is the mean vertical velocity above the bottom boundary layer [Gula et al., 2015]. Thus, a net negative contribution by the spatially integrated bottom pressure torque (integral of 3.11), associated with the anticyclonic meander, implies Ekman suction $w_{bot} > 0$ and thus upwelling of cold waters within the bottom boundary layer. In addition, frictional spindown of the anticyclonic boundary current promotes a rapid modification of the bottom

stratification by advecting cold water towards the west wall ($x = 0$), strongest where the flow becomes aligned to the wall. Thus, at west wall, the Ekman suction and frictional spindown promotes an increase in the stratification of the water column above, thus making the anticyclonic boundary current more bottom trapped.

As the flow separates at the ridge crest where β_T=0, it continues to experience frictional spindown along f/H contours, inducing transport down the slope within the bottom boundary layer (Fig. 3.8a,d,g at x=530). Transport within the bottom boundary layer then promotes a slow descent, as can be seen from the downslope migration of the interior eastward velocity (Fig. 3.8d and g at $y = 530$km), as well as from the descent of the thickness of the bottom boundary layer (Fig. 3.7), which also shows the mild downward migration of eddies. Thus, the frictional spindown of the current along f/H contours, contributes on the location of the cyclonic boundary current at the east wall down the slope, at greater depths, when compared to the location of the separating anticyclonic boundary current.

At the east wall, the spatial integral of the bottom pressure torque implies Ekman pumping ($fw_{bot} < 0$) of warm waters into the bottom boundary layer, while the frictional spindown promotes an advection of warm interior waters west of the wall, where ambient waters are relatively colder (Fig. 3.6b, $x = 220$km, $y = 600$km). This results in a convectively unstable water column, therefore reducing the vertical stratification near and downstream from the cyclonic boundary current (Fig. 3.9a,b $x > 220$km, $y > 600$km), in agreement with the observed along wall stratification at the east wall (Fig .3.5d). Such destratification associated with the cyclonic boundary current can lead a potentially interesting and rich instability problem, the subject of an accompanying paper.

3.5 Discussions and Conclusions

We have presented an idealized model of a large scale throughflow across a symmetric ridge, where we investigated the asymmetry on inertial recirculation across the ridge crest, that result in increase of momentum dissipation localized to boundary currents. Central to our study was the effect of stratification and dynamics within the bottom boundary layer and

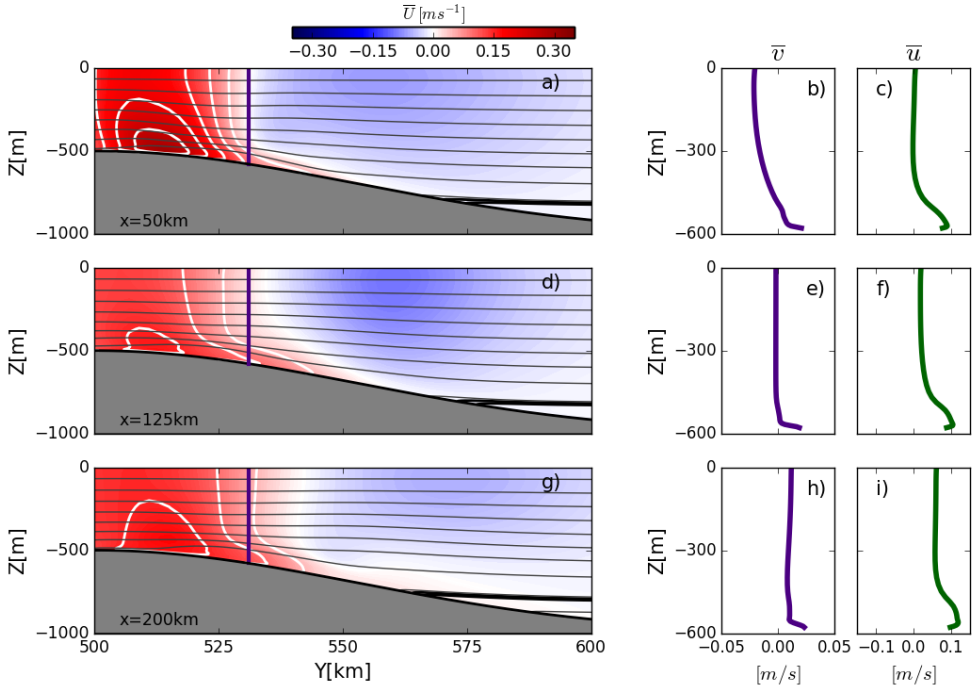

Figure 3.8: Frictional spindown of the along-slope flow for simulation Cst_{ns}, where $\lambda_{_M}$ = 17km. Mean zonal ($\overline{u}$) velocity is shown at three sections away from the influence of lateral boundary current. Thus, the only cross-slope flow is the to friction within the bottom boundary layer. Also shown are vertical profile of along/across slope flow at y = 530km. Isotherms are shown every 0.5° C (gray contours).

localized to the throughflow as it navigates topography, on determining the spatial differences on the large scale barotropic circulation. We found that the anticyclonic boundary current required less inertia (torque) to promote transport up the slope, when compared to the cyclonic boundary current downstream from the ridge crest, which requires a stronger inertia (torque) to promote an equal transport down the slope. This implies stronger topographic steering experienced by the throughflow is it moves past the ridge crest.

The contrasting difference between the barotropic behavior of the throughflow across the ridge crest, we found to be largely associated with the destratification of the cyclonic boundary current by bottom Ekman transport of water waters that resulted in a convectively

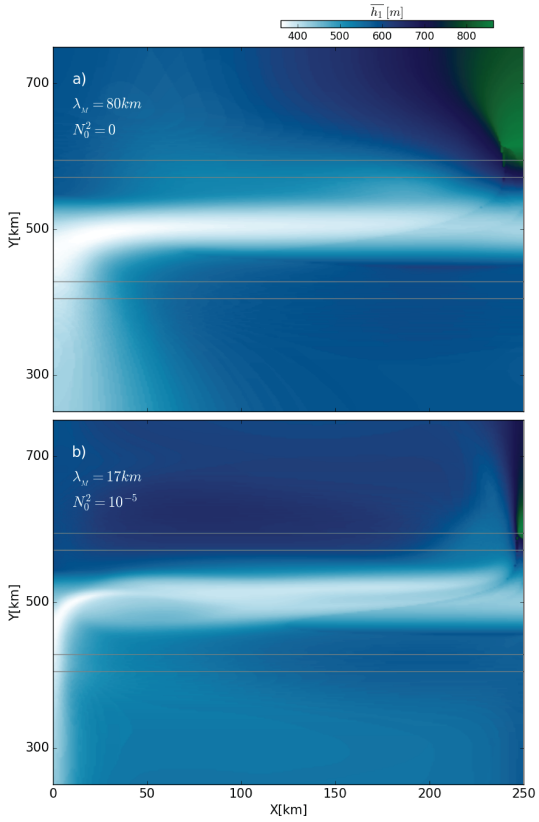

Figure 3.9: Thickness of the water column above the mean isotherm $\overline{T}_0 = 6.0° \, C$ in the viscous stratified simulation Ast_{ns} (a) and nonlinear stratified simulation Cst_{ns} (b). Both simulations show a deepening of the layer downstream of the cyclonic boundary current, representing a rapid destratification of the water column due to advection of warm water within the bottom boundary layer. The difference in the lateral extent of the deepening region is determined by the width of the boundary current.

unstable bottom boundary layer, and strengthening of the stratification by Ekman transport associated with the anticyclonic boundary current. In addition, the relative location of the boundary currents with respect to the ridge crest, with the anticyclonic closer to the ridge crest where topographic slope nearly vanishes, further increased the asymmetry, an effect due to the continuously varying sloping bottom (a departure from linear slopes).

We found an asymmetry on the eddying field between the boundary currents, with eddies associated with the cyclonic boundary current being advected downstream from the ridge

and experiencing barotropization due to nonlinear interaction between the eddies. Along the ridge, eddies are predominantly cyclonic due to the anticyclonic recirculating meander at the west wall. Such meander facilitates the upslope transport of cold waters up the slope, and can potentially promote southward downslope transport due to its recirculation nature. Such behavior agrees with observations of northward (upslope) advection of floats located on cold overflow plumes that navigate along sloping bottom south of the IFR crest [Prater and Rossby, 2005].

Given the simplicity of our model, with the circulation implied by topographic Rossby waves associated with large amplitude topography, our results are robust in the sense that Ekman dynamics will promote a reduction of the baroclinicity of the flow whenever the bottom flow down the slope has enough torque to promote Ekman pumping and frictional spindown, promoting a destratification at depths determined by the sloping bottom. The presence of the anticyclonic meander near the ridge crest is also robust for a large broad inflow that is perpendicular to a large amplitude ridge.

Our model of the topographically steered component of the Atlantic inflow across the IFR does a good job on incorporating some of the most important features: A western intensified, recirculating anticyclonic meander on the ridge crest, along ridge eddying variability, and a downstream cyclonic circulation typical of the Nordic seas, although in our model such basic scale barotropic behavior is associated with eddies that detach from the boundary current. Most important, is the characterization of the northward downslope flow as requiring strong inertia, such that the northward (downslope) flow experiences a greater resistance to cross f/H contours than the flow upstream. Thus, in the absence of a lateral (eastern) wall, but rather a continuous (but steeper) sloping bottom, a current will get attached to the sloping bottom and continue flowing along f/H contours, following a cyclonic path.

This interesting result may help understand the observed behavior of the circulation downstream from the ridge on the Nordic basins, where the Atlantic inflow is strongly topographically steered along f/h contours cyclonically around the basin [Hansen and Østerhus, 2000, Hansen et al., 2008], a complementary but different explanation for the preferred cir-

culation around high latitude closed basins [Nøst et al., 2008, LaCasce et al., 2008].

The validity of the approximation of channel geometry with a symmetric ridge intersecting lateral walls as a model for throughflows across a ridge, most is appropriate when topographic ridge ends at a coastal shelfbreak, with the slope of the shelfbreak being is much greater that the slope of the ridge. In such scenario, long topographic Rossby waves become arrested. Then, the mean flow navigating the ridge would experiences the coastal shelf effectively as a wall, developing an inertial recirculation in order to promote cross-slope transport, and satisfy basin scale constraints or mass, volume, energy and potential vorticity.

Chapter 4

ON THE ASYMMETRY OF THE CIRCULATION OF THROUGHFLOWS ACROSS LARGE AMPLITUDE TOPOGRAPHY. PART II: INJECTION OF BOUNDARY LAYER PV

4.1 Introduction

The pathway of large scale, topographically steered throughflows across finite amplitude topography results from a balance between baroclinic form stress (bottom pressure changes along topographic contours), lateral dissipation and eddy induced vorticity fluxes that redistribute momentum along f/H contours (as described in Chapter 3). The mean flow develops into a bottom-intensified, anticyclonic western boundary current as it flows into the ridge crest, and separates from the wall as it encounters a reversal of sign in the topographic slope. The mean flow then follows f/H contours and developes into a cyclonic, eastern boundary current as it encounters the eastern wall and flows into deeper water downstream from the ridge. A seldom studied approach at large scales, throughflows along channel geometry can represent exchanges of topographically steered flows across ocean basins constrained laterally by abrupt coastal shelfs, such as the flow of North Atlantic waters across the Iceland-Faroe Ridge [Hansen et al., 2003, Østerhus et al., 2005, Hansen et al., 2008, 2010].

An overlooked component of boundary currents and therefore throughflows, is their vertical structure, in particular the secondary ageostrophic circulation associated with the bottom boundary layer [Pedlosky, 1968]. Depending on the orientation of the mean (interior) flow with respect to f/H contours, bottom friction can lead to an Ekman transport across f/H contours, rapidly modifying the stratification of the boundary layer and even the upper ocean if such advection results in a convectively unstable stratification [Condie, 1995, Wåhlin and

Walin, 2001, Brink and Lentz, 2010]. Moreover, bottom friction can lead to an Ekman arrest, when the Ekman transport promotes a horizontal buoyancy gradient in thermal wind balance, in which the geostrophic shear reduces the effects of the bottom boundary layer onto the mean interior flow [MacCready and Rhines, 1991, Trowbridge and Lentz, 1991, MacCready and Rhines, 1993]. Furthermore, baroclinicity within a *thick* bottom boundary layer, can become unstable to baroclinic instability, leading to a rapid restratification of the bottom boundary layer [Wenegrat et al., 2018]. Lastly, diapycnal mixing at the bottom can drive frictional flow up the slope by weakening the stratification, thus promoting a stable boundary layer [Wunsch, 1970, Phillips, 1970, Thorpe, 1987, Benthuysen and Thomas, 2012].

In the case of channel throughflows across finite amplitude ridge topography, the flow experiences significant along stream variability that result in localized regions of enhanced turbulent mixing, effectively increasing the bottom boundary layer thickness. Thus, Ekman dynamics within a thick boundary layer can become very effective in inducing a modification of the upper interior ocean through rapid re or de-stratification within the bottom boundary layer. Then, depending on the resulting localized distribution of potential vorticity within the bottom boundary layer, the mean flow or baroclinic eddies can advect PV anomalies away into the interior. Such non-local redistribution by eddies has already been explored in idealized studies of subduction in surface fronts [Spall, 1995, Manucharyan and Timmermans, 2013] and shelf break boundary currents [Spall et al., 2008], although in these studies, bottom boundary layer dynamics are largely unresolved. Similarly, most studies of bottom boundary layer dynamics do not consider equilibrated interior flows with significant along-stream variability.

How bottom boundary layer control may come about in topographically steered throughflows is unclear, particularly since the mean flow experiences significant along-stream changes *i.e.* boundary current formation localized to lateral boundaries, and eddies that propagate along f/H contours. Both of these characteristics of the mean flow outside the boundary layer, usually neglected in quasi 2D idealized studies of bottom boundary layer dynamics, can introduce patterns on the bottom diapycnal mixing and frictional stresses along f/H

contours, and thus have the potential for constraining the effect of boundary layer dynamics to localized regions along the path of the flow as it crosses the ridge.

In this study we investigate the effects associated with baroclinic eddies and bottom boundary layer dynamics on the throughflow across a finite amplitude ridge. We analyze the (Ertel) potential vorticity (PV) of the fluid, a dynamically active tracer with conservation properties that incorporate both thermodynamic and dynamical aspects of the flow [Haynes and McIntyre, 1987, 1990], using a combination of theory and numerical simulations of the primitive equations. What makes ideal the use of the PV of the fluid, is its ability to describe density and mean flow anomalies associated with bottom boundaries as *High* or *Low* PV, associated with the presence of a strong or low vertical stratification within the bottom boundary layer, respectively, with respect to background values associated with the large scale field. Additionally important to the understanding of the distribution of PV anomalies, is the role of advective processes such as that by the eddies or the mean.

The outline of the paper is as follows: In section 2 we derive the expressions for eddy potential vorticity fluxes, mean advective fluxes, as well as boundary PV fluxes consistent with integral balances of PV, and associated with the intersection of density surfaces along solid boundaries, where bottom boundary layer dynamics can result in net fluxes into the interior. In section 3 we present the main results beginning with a description of the vertical structure of the mean fields associated with equilibrated simulations, and the resulting integral PV balance. We then relate the PV integral balance, which incorporates boundary PV sources, with the dynamics within the bottom boundary layer. Lastly, we summarize our findings and conclusions in section 4.

4.2 Boundary sources of potential vorticity

In the primitive equations, the conservation of (Ertel) potential vorticity$q = \boldsymbol{\omega}_a \cdot \nabla b$ in flux form is given by

$$\frac{\partial q}{\partial t} = -\nabla \cdot \mathbf{J} \tag{4.1}$$

where $\boldsymbol{\omega}_a = (-v_z, u_z, f+\zeta)$ is the absolute vorticity with $\mathbf{u} = (u, v, w)$ the 3D velocity, $\zeta = v_x - u_y$ the relative vorticity and $b = g\alpha T$ buoyancy, where we have assumed a linear equation of state. The PV flux vector can be written in two equivalent forms

$$\mathbf{J} = \underbrace{\mathbf{u}q}_{\mathbf{J_A}} + \underbrace{\nabla b \times \mathbf{F}}_{\mathbf{J_{NA}}} = \nabla b \times \nabla B + \nabla b \times \left(\frac{\partial \mathbf{u}_h}{\partial t}\right) - \boldsymbol{\omega}_a \frac{\partial b}{\partial t} \tag{4.2}$$

$B = (1/2)|\mathbf{u}|^2 + g(\eta - z) + p/\rho_0$ is the Bernoulli potential, where η is the surface elevation, p the fluid pressure due to interior stratification, and $\mathbf{F} = \mathbf{F}_h + \rho_0^{-1}\partial_z \boldsymbol{\tau}$ represents dissipation of horizontal momentum. Although each dissipative term is left implicit in our analytical formulation, $\mathbf{F}_h$ represents viscous, harmonic horizontal dissipation of momentum.

The two equivalent formulations of the PV flux vector $\mathbf{J}$ allow complementary interpretations: $\mathbf{J}$ can be decomposed into an advective and a dissipative flux contribution [Haynes and McIntyre, 1987, 1990], and so in the absence of dissipative or diabatic processes, the evolution of (Ertel) potential vorticity is given entirely by the divergence of advective fluxes. Furthermore, the interior advective redistribution of PV in the presence of eddying variability can be split into a mean and eddy advection, *i.e.* $\mathbf{J}_A = \overline{\mathbf{u}}\,\overline{q} + \overline{\mathbf{u}'q'}$, where the overbar $\overline{()}$ represents time-mean, and primed variables $()'$ represent the deviation (eddy) from such mean. Lastly, if the flow is steady (last two terms in (4.2) are zero), the intersections of surfaces of constant Bernoulli potential and surfaces of constant buoyancy/temperature represent streamlines for the total potential vorticity flux, and three dimensional flow too in the absence of dissipation [Schär, 1993, Bretherton and Schär, 1993].

In the quasigeostrophic limit, the intersection of temperature/buoyancy surfaces with bottom topography can be represented as PV-delta sheets [Bretherton, 1966, Rhines, 1979], which can be tapped by the circulation and, in most extreme cases, be advected by the mean flow leading to downstream formation of cyclonic anomalies [Hallberg and Rhines, 2000, Schneider et al., 2003]. In what follows, we derive a local flux formulation of the topographic PV flux in primitive equations that is general enough that it can incorporate dynamics beyond QG, and allow us to diagnose the topographic PV flux that is consistent

with a volume integrated *Eulerian* Ertel PV balance.

Using the Bernoulli formulation of the PV flux vector in (4.2), the topographic PV flux can be written as the sum of two contributions, that is

$$\overline{\mathbf{J}} \cdot \mathbf{n}_{bot} = \overline{\mathbf{J}}^{t} \cdot \mathbf{n}_{bot} + \overline{\mathbf{J}}^{s} \cdot \mathbf{n}_{bot} \tag{4.3}$$

where the superscripts t and s differentiate between the fluxes that explicitly depend on the *tendency* of flow variables (time derivatives) or not. $\mathbf{n}_{bot} = (0, -dh/dy, -1)$ is the local normal vector to bottom topography, outward pointing. These terms are

$$\overline{J}^{t}_{bot} = \mathbf{n}_{bot} \cdot \left[\overline{\nabla b \times \left(\frac{\partial \mathbf{u}_h}{\partial t} \right)} - \overline{\boldsymbol{\omega_a} \frac{\partial b}{\partial t}} \right] \Big|_{z=-h} \tag{4.4}$$

which vanishes when the flow reaches steady state, and

$$\overline{J}^{s}_{bot} = \mathbf{n}_{bot} \cdot \left(\overline{\nabla b \times \nabla B} \right) \big|_{z=-h} \tag{4.5}$$

In the presence of finite amplitude topography, linearization of the bottom boundary condition is no longer possible. Thus we introduce a σ-coordinate transformation to transform a horizontal (*i.e.* meridional) derivative to terrain-following coordinates [Shchepetkin and McWilliams, 2005]. Thus, a terrain following derivative is

$$\left. \frac{\partial (\cdot)}{\partial y} \right|_{\sigma=-1} = \left(1 - \gamma_{(\cdot)} \right) \left. \frac{\partial (\cdot)}{\partial y} \right|_{z=-h} \tag{4.6}$$

where $\sigma = \mathcal{G}(\eta, h)$ is the terrain following coordinate with $\mathcal{G}$ a nonlinear *stretching* function, such that $\sigma(0) = \eta(x, y)$ and $\sigma(-1) = -h(y)$. The left hand side of (4.6) represents an along-bottom derivative of a scalar function denoted by $(\cdot)$, where $\gamma_f = (dh/dy) \big/ ((\cdot)_y / (\cdot)_z)$ is the ratio of local slope of $(\cdot)$ to the topographic slope, which vanishes for flat bottom topography. γ_f arises as a *stability slope* parameter that measures the effect of the sloping bottom on baroclinic instability, when applied to buoyancy (temperature) surfaces (γ_b) [Blumsack and Gierasch, 1972, Lozier and Reed, 2005, Isachsen, 2011].

Given the transformation (4.6), the (time-mean) contribution of the topographic PV flux vector by the first term in the rhs of (4.3) is

$$\overline{J^t_{bot}} = \underbrace{-\hat{\mathbf{k}} \cdot \left(\overline{\nabla_\sigma b \times \frac{\partial \mathbf{u}_h}{\partial t}} \right) \Big|_{\sigma=-1}}_{\overline{J}^t_{b1}} + \underbrace{\left[\overline{\left(f + \zeta_\sigma\right) \frac{\partial b}{\partial t}} \right] \Big|_{\sigma=-1}}_{\overline{J}^t_{b2}} \tag{4.7}$$

where $\hat{\mathbf{k}}$ is the unit vector perpendicular to depth-surfaces (note that there is no stretching in the x-direction in this study, but the expression (4.7) is general in the sense that can also represent stretching in x, as long as an equivalent transformation to (4.6) in the x-direction is introduced). Thus $\overline{J}^t_{bot} = 0$ either when the flow is in steady state, or when surfaces of constant buoyancy (temperature) do not intersect the bottom, and the along-bottom vorticity $\zeta_\sigma = -f$.

The contribution to the net topographic PV flux by the second term term in (4.3) can be written as

$$\overline{J}^s{}_{bot} = \left[\overline{B_x b_y \left(1 - \gamma_b\right)} - \overline{b_x B_y \left(1 - \gamma_B\right)} \right]_{z=-h(y)} \tag{4.8}$$

or, using σ-coordinates,

$$\overline{J}^s_{bot} = \overline{\frac{\partial_\sigma (B, b)}{\partial (x, y)}} \Big|_{\sigma=-1} \tag{4.9}$$

where the subscripts σ on the Jacobian term $\partial_\sigma(\cdot, *)/\partial(x, y)$ implies that derivatives are along sigma (terrain following) coordinates.

Now, we introduce the functional $\Gamma_b = \Gamma[b; y, z]$ acting on the scalar function b (in this case we take b as buoyancy, but it can be any function), defined as

$$\Gamma_b = \left(\frac{\partial b}{\partial y} \Big|_{\sigma=-1} \right) \Big/ \left(\frac{dh}{dy} \right) \tag{4.10}$$

The functional Γ_g represents the ratio between along-bottom northward gradient (*i.e.* along $\sigma = -1$ surface) to topographic slope, where we have used the transformation (4.6) for simplicity and compact notation. With this, the expression in (4.8) is

$$\overline{J^s}_{bot} = \left[\overline{B_x\Gamma_b} - \overline{b_x\Gamma_{_B}}\right]\Big|_{z=-h(y)} \frac{dh}{dy} \tag{4.11}$$

We now decompose $\overline{J}^s_{bot}$ into contributions from (lateral) boundaries (*i.e.* where topography intersects lateral boundaries) and terms along f/H contours. Then, the time-mean net topographic PV flux $\overline{J}_{bot}$, given by the sum (4.3) is

$$\overline{J}_{bot} = \Delta_x \overline{J}^*_{bot} + \int\int \left(\overline{b_{bot}\frac{\partial \Gamma_{_B}}{\partial x}} - \overline{B_{bot}\frac{\partial \Gamma_b}{\partial x}}\right)\Big|_{z=-h} \frac{dh}{dy} dxdy + \int\int \overline{J}^t_{bot} dxdy \tag{4.12}$$

where $\Delta_x(\cdot) = (\cdot)_{x=L} - (\cdot)_{x=0}$ is the cross-channel difference (*i.e.* difference between the evaluation at eastern and western walls). The first term on the RHS of (4.12) is associated with effects on lateral walls, *e.g.* form stresses; this term would vanish in a zonally periodic domain. The second term in (4.12) is associated with changes of buoyancy, pressure and kinetic energy across and along f/H contours, while the third term is associated with the *tendency* terms in (4.7).

The first term on the RHS of (4.12) can be expanded as follows:

$$\Delta_x \overline{J}^*_{bot} = \Delta_x \overline{\mathcal{F}^{BT}_{\Gamma}} + \Delta_x \overline{\mathcal{F}^{BC}_{\Gamma}} + \Delta_x \overline{\mathcal{E}_{\Gamma}} - \Delta_x \overline{\mathcal{S}_{\Gamma}} \tag{4.13}$$

where

$$\begin{aligned}
\mathcal{F}^{BT}_{\Gamma} &= \int_0^M (g\eta\Gamma_b)\big|_{z=-h} \frac{dh}{dy} dy \\
\mathcal{F}^{BC}_{\Gamma} &= \int_0^M \left(\frac{p\Gamma_b}{\rho_0}\right)\Big|_{z=-h} \frac{dh}{dy} dy \\
\mathcal{E}_{\Gamma} &= \frac{1}{2}\int_0^M (\Gamma_b v^2)\big|_{z=-h} \frac{dh}{dy} dy \\
\mathcal{S}_{\Gamma} &= \int_0^M (b\Gamma_{_B})\big|_{z=-h} \frac{dh}{dy} dy
\end{aligned} \tag{4.14}$$

Table 4.1: Parameters relevant to lateral boundary currents. For stratified simulations, variables are vertically averaged within 100m from the bottom, localized to boundary currents, given the bottom intensified nature of the flows in all stratified simulations.

Experiment	$A_H\ [m^2 s^{-1}]$	$N_0^2[s^{-1}]$	$\lambda_M\ [km]$	$\overline{V}_{bot}[ms^{-1}]$		$\lvert Ro\rvert_{bot}$		Re		N^2_{bot}	
				WBC	EBC	WBC	EBC	WBC	EBC	WBC	EBC
A_{fs}	2500	$--$	79.4	0.45	0.345	0.05	0.04	14.3	10.96	–	–
A_{ns}	2500	$--$	79.4	0.24	0.22	0.02	0.02	7.62	6.99	–	–
Ast_{fs}	2500	10^{-5}	79.4	0.20	0.28	0.15	0.09	3.81	8.26	3.06	1.04
Ast_{ns}	2500	10^{-5}	79.4	0.11	0.17	0.08	0.05	2.86	4.76	3.07	0.87
B_{fs}	250	$--$	36.8	0.84	0.48	0.18	0.1	123.6	70.7	–	–
B_{ns}	250	$--$	36.8	0.54	0.43	0.12	0.09	79.5	63.3	–	–
Bst_{fs}	250	10^{-5}	36.8	0.47	0.47	0.45	0.16	41.2	66.24	2.39	0.85
Bst_{ns}	250	10^{-5}	36.8	0.24	0.36	0.18	0.12	26.5	53	2.82	0.83
C_{fs}	25	$--$	17.1	0.94	0.48	0.44	0.22	643	328.3	–	–
C_{ns}	25	$--$	17.1	0.78	0.65	0.36	0.31	533.5	444.6	–	–
Cst_{fs}	25	10^{-5}	17.1	0.47	0.62	0.72	0.17	218.9	478.8	2.63	0.87
Cst_{ns}	25	10^{-5}	17.1	0.32	0.39	0.28	0.91	164.2	321.5	2.2	0.7

Ast_{fs}, Ast_{ns}: Stratified simulation A performed using *free slip* and *no slip* tangential boundary condition. A_{fs} refers to homogeneous (single density) simulation A using *free slip* boundary condition.

WBC, EBC: Value calculated for the western/eastern boundary current, respectively.

Our formulation of net topographic PV fluxes (4.12) shows the role of form stresses associated with lateral boundary currents in promoting local (and net) PV fluxes (4.13), as well as the potential role of along-slope variations of buoyancy and bottom Bernoulli potential in promoting local and integral PV fluxes. Along slope variations of buoyancy and bottom Bernoulli potential are associated with viscous dissipation, ageostrophic flows an eddies. The question of which processes of PV flux make the largest contribution, and what effect this flux has on structure of the mean flow associated with an equilibrated throughflow past finite amplitude topography is examined next.

We use a similar domain and experimental designed as in Chapter 3, where we apply uniform open inflow/outflow boundary conditions upstream and downstream from the ridge, respectively, forcing a lateral volume influx of $Q_{in} \approx 3$ Sv (1 Sv=$10^6 m^3 s^{-1}$) with a vertical stratification $N_0^2 = 1 \times 10^{-5} s^{-2}$. This results in a boundary inflow/outflow given by a (purely advective) potential vorticity flux of magnitude $\mathbf{J}^*_{_A} = N_0^2 H_0 v_0 f \hat{\mathbf{j}} \approx 5 \times 10^{-12} m^2 s^{-4}$. The local coordinates are rotated so that northward in our experimental setup represents cross-ridge, and east-west is parallel to topographic contours. We refer to Chapter 3 for a detailed description of the model numerics, and Table 4.1 for parameters associated with mean flow circulation across large amplitude topography.

Given the potential role of the bottom boundary layer away from the influence of lateral (mean) boundary currents, we introduce relevant parameters that arise in the idealized study of reentrant, (vertically) semi-infinite bottom boundary layer dynamics (see Table 4.2). A parameter of great importance of along slope flows is the (*small angle*) slope Burger number $S \approx (N\theta/f)^2$ where $\theta \approx dh/dy$. The timescale at which buoyancy forces balance an (initial) up/down-slope Coriolis force is given by the buoyancy shutdown timescale, defined as $\mathcal{T}_{shut} = P_r^{-1} S^{-2} f^{-1}$, valid for $S \ll 1$. Similarly, the stratified frictional spindown time scale is given by $\mathcal{T}_{spin} = E^{-1/2} f^{-1}$, where $E = 2A_\nu / f H_p^2$ is the Ekman number and $H_p = fL/2\pi N$ the Prandtl depth, the depth scale over which anomalies penetrate into the interior. The inertial and diffusive time scales are expressed as $\mathcal{T}_{inertial} = f^{-1}$ and $\mathcal{T}_{diffusive} = E^{-1} f^{-1}$.

The diffusive boundary layer has thickness of $\delta_T = (2A_\kappa \mathcal{T}_{diff})^{1/2}$, whereas the bottom

Table 4.2: Parameters associated with bottom boundary layer dynamics, arising on the region away from the influence from lateral boundary currents, along f/H contours atop the ridge, in all our simulations. The region is defined laterally as $\lambda_M < x < 250 - \lambda_M$. Values represent an average over this region.

Parameter	Description	Value
θ	(small angle) topographic slope	0.002
A_ν	Vertical mixing coefficient	$\approx 5 \times 10^{-3}[m^2 s]$
A_κ	Vertical diffusivity coefficient	$\approx 5 \times 10^{-3}[m^2 s]$
N_c^2	Buoyancy frequency at ridge crest	1.3×10^{-5} $[s^{-2}]$
S	Slope Burger number $S = (\theta N_c/f)^2$	0.003
H_p	Prandtl depth	$55[m]$
E	Ekman number	0.026
P_r	Prandtl number	≈ 1
$\mathcal{T}_{shut}$	Buoyancy shutdown timescale	8360 [days]
$\mathcal{T}_{spin}$	Spindown timescale	0.57 [days]
$\mathcal{T}_{diff}$	Diffusive timescale	3.5 [days]
$\mathcal{T}_{adv}$	Advective timescale	3.8 [days]
$\mathcal{T}_{inertial}$	Inertial timescale	0.58
δ_{Ek}	Ekman layer thickness	9 $[m]$
δ_T	Diffusive boundary layer thickness	55 $[m]$
ω_{bbl}	Eddy forcing frequency	2.31×10^{-6} $[s^{-1}]$

boundary layer thickness is defined as $\delta_{Ek} = \sqrt{2A_\nu/f}$, which not only can vary spatially according to patterns of enhanced vertical (turbulent) mixing, but also can vary in the presence of eddy variability. Eddies that propagate along f/H contours then introduce temporal variability on the thickness of the bottom boundary layer, measured by the ratio $r_\omega = \omega_{bbl}/f$. $r_\omega \ll 1$ characterizes slow evolving flows where *buoyancy shutdown* can take place [Ruan and Thompson, 2016]. Lastly, given that f/H contours begin and end at solid lateral walls, in regions with strong lateral boundary currents where quasi-2D boundary layer scaling are no longer valid, we introduce an advective timescale $T_{adv} = L_w/\overline{U}$ where $\overline{U}$ is the scaling for the along ridge flow, within a length scale L away from the influence of lateral boundary currents. While L_w depends on $\lambda_{_M}$, which varies for each experiment, an good estimate in our simulations is $L_w \sim O(100)$km, which makes $T_{adv} \sim 4$ days. Thus, a water parcel will be advected by the mean flow along f/H contours for roughly 4 days.

4.3 Results

In this section, we analyze simulations of continuously stratified, rotating throughflows under channel geometry and characterized by a net mean transport across finite amplitude bottom topography. Throughout this paper, unless otherwise stated, we focus particularly on simulation CSt_{ns} characterized by narrow ($\lambda_{_M} \approx 17km$) unstable lateral boundary current and a $Ro \sim O(1)$ associated with the cyclonic boundary current (see Table 3.1). Thus, the simulation best describes an equilibrated, topographically steered flow with significant along-stream variability, with locally Ekman dynamics are relatively important. At the end of this section, we will address the rest of the simulations, when we present the topographic PV fluxes just derived in the previous section. We refer to our previous study (Chapter 3) for a through description of the dominant balances that lead to the equilibration of the circulation.

The mean circulation is characterized by a bottom-intensified anticyclonic boundary current associated with the southward facing (decreasing y direction) sloping bottom localized near the ($x = 0$) wall, and a cyclonic boundary current associated with the northward facing

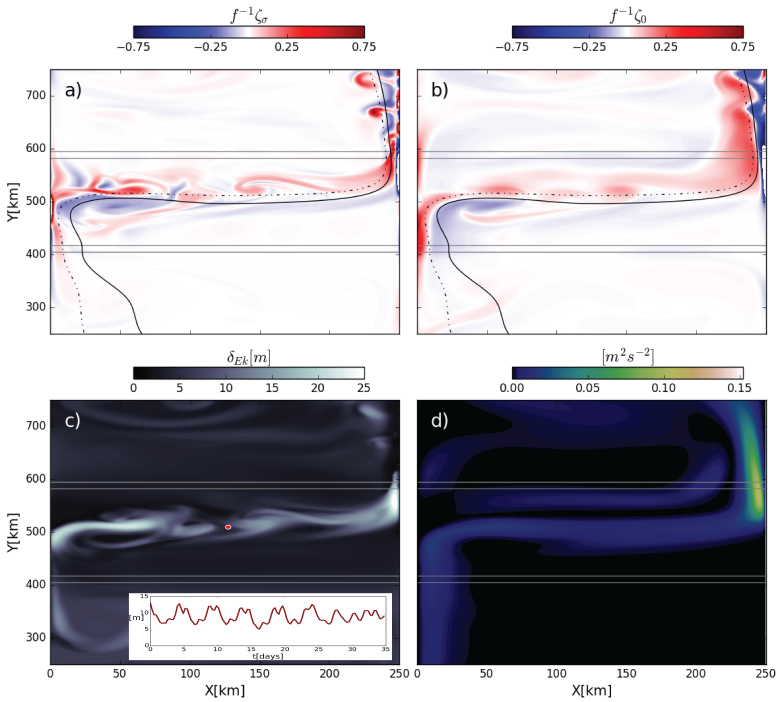

Figure 4.1: Snapshots of relative vorticity within the bottom boundary layer ζ_σ (a) and at the surface ζ_0 (b), both scaled by the Coriolis parameter, in simulation Cst_{ns}. The span of the bottom ridge centered at y=500km is shown by the light gray contours, with the mean streamlines $\psi_l = 0.5Sv$ (dashed black) and $\psi_c = 1.5$Sv (solid black) representing the mean transport pathway. Also shown is the bottom boundary layer thickness $\delta_{Ek} = \sqrt{2A_\nu/f}$ (c), which displays significant along-ridge variation due to (bottom intensified) baroclinic eddies. A time series of δ_{Ek} along the path of the mean flow away from boundary currents (red circle in c) is also shown. Lastly, the surface mean kinetic energy $(1/2)\overline{\mathbf{u}}_h^2$ is shown in (d), with a maximum along the cyclonic boundary current.

sloping bottom localized near the eastern wall ($x = 250$km). Atop the ridge, the mean flow is bottom intensified and along f/H contours, near the ridge crest.

We examine the vertical structure of the mean flow along the path of (time) mean transport streamlines that are calculated by inverting the 2D Laplacian of the (barotropic) vorticity ($\psi = \nabla^2\Omega$). While in the presence of sloping topography there is no longer a barotropic mode but instead a bottom intensified topographic Rossby wave [Rhines, 1970], the depth scale of topographic Rossby waves associated with the mean (boundary current) circulation

atop the ridge is relatively of the same order that the depth at the ridge crest $H_p \sim O(500m)$. Moreover, given that atop the ridge, all shear and baroclinicity is concentrated towards the bottom (*i.e.* there is no surface forcing), the vertically integrated flow fields represent a good approximation of the dominant (throughflow scale) dynamics that are associated with topographically locked Rossby waves.

Rather than integrate flow variables within an envelope defined by streamlines (*e.g.* an envelope defined by two of $\psi = \{0.5, 1.5, 2.5\}\ Sv$), we examine the quantities along each individual streamlines, recognizing that streamlines can diverge from each other, and follow a very different path along or across the ridge than the bottom intensified flow, and thus diverge greatly from path follow by topographically steered flow (*e.g.* Fig. 4.2 a and e). We find, generally that streamlines $\psi = 0.5, 1.5Sv$ do a good job in representing the (time-mean) topographically locked circulation (Fig. 4.1a-b).

Along the path of the mean flow atop the ridge crest, we find a laterally and temporally varying vertical (turbulent) viscosity A_ν as a result of along-stream changes on the bottom intensified current and eddies that separate from the western boundary current and propagate along f/H contours (Fig. 4.1a). As a result, the thickness of the bottom boundary layer $\delta_{Ek} = \sqrt{(2A_\nu/f)}$ varies along the path of the flow atop the ridge, with the greatest thickness localized to the boundary currents $\delta_{Ek} \approx 25m$. Along the f/H path of the bottom-intensified flow away from boundary currents, $\delta_{Ek} \approx 10 - 12m$ (Fig. 4.1c). Furthermore, baroclinic bottom intensified eddies promote thickness changes to the boundary layer $\delta'_{Ek} \pm 3m$ of the mean value (see Fig. 4.1c, inplot), with a timescale of approximately 4-5 days. The ratio of frequency on boundary layer thickness variability to inertial frequency $r_\omega = \omega_{bbl}/f << 1$, which means that eddies allow the bottom intensified flow along f/H contours to escape buoyancy shutdown [Ruan and Thompson, 2016].

The behavior of both the mean and eddy kinetic energy (MKE and EKE respectively) along the western boundary current is, as expected by the enhanced near bottom vertical stratification (Table 4.1), bottom intensified (Fig. 4.2a-d, at $R \approx 550$km). The maximum mean and eddy kinetic energy are located close to each other, and decay rapidly as the flow

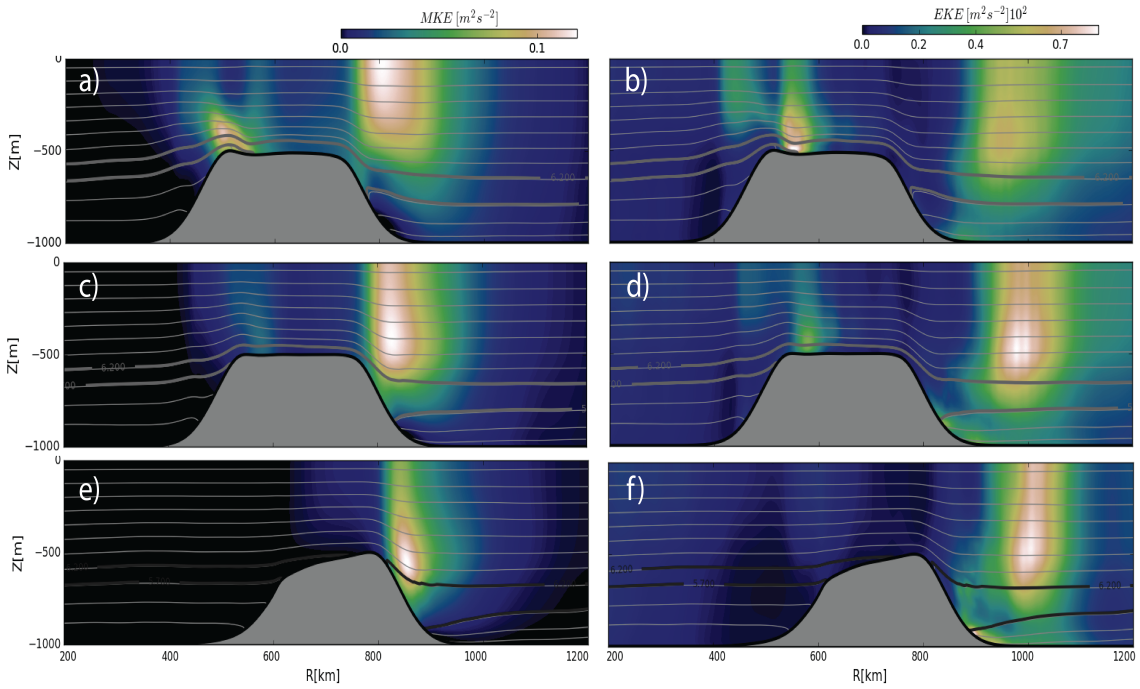

Figure 4.2: Along stream mean kinetic energy (MKE) (left column) and eddy kinetic energy (EKE) (right column) at streamlines $\psi_l = 0.5Sv$ (a, b), $\psi_c = 1.5Sv$ (c,d) and $\psi_u = 2.5Sv$ (e, f). Light gray contours represents isotherms, plotted at every $0.5°\ C$. The streamline $\psi = 2.5Sv$ crosses the ridge east of the crossing of the other two streamlines. The three streamlines do, however, align and exhibit a similar behavior downstream from the ridge crest.

moves along the ridge crest. MKE and EKE associated with the cyclonic boundary current are laterally apart from each other, roughly 150km, with the EKE maximum taking place downstream from the MKE maximum (EKE maximum at R≈ 1000km, see fig. 4.2b,d; MKE maximum at $R \approx 850$km, see fig. 4.2a,c).

The vertical structure of MKE and EKE along the cyclonic boundary current is suspect (*e.g.* MKE behavior seen at R=850km in Fig. 4.2c, and EKE behavior at R=1000km in Fig. 4.2d). Both are middepth intensified, above the isotherm $T = 6.2°C$ (Fig.4.2a-d), an isotherm that reaches across the ridge crest upstream. Their vertical structure (MKE and EKE) decays rapidly at increasing depths and slowly toward shallow depth. This suggests that both MKE and EKE retain the vertical structure of a (bottom intensified) topographically Rossby wave,

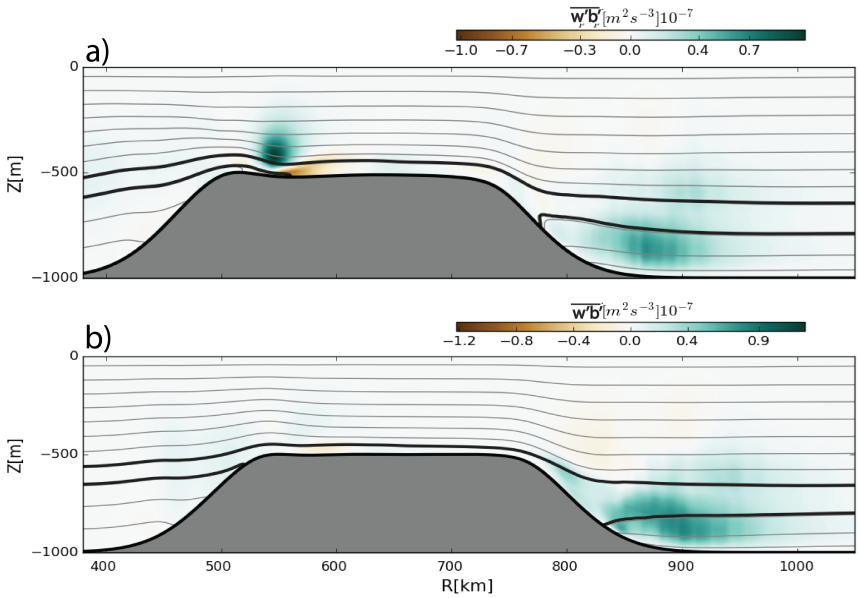

Figure 4.3: Buoyancy production ($\overline{w'b'}$) along the $\psi = 0.5\ Sv$ (a) and $\psi = 1.5\ Sv$ (b) time mean streamlines. Temperature is plotted at every 0.5° C (grey contours). Thick black contours represent the isotherms $\overline{T}_1 = 5.7°\ C$ and $\overline{T}_2 = 6.2°\ C$, which define the layer with anomalous low PV. At distance $R = 550$km along the path of the streamlines, buoyancy production $\overline{w'b'} > 0$ associate with the anticyclonic (western) boundary current can be seen clearly along $\psi = 0.5Sv$, and only faintly along $\psi = 1.5$Sv, due to bottom intensified vertical shear that introduces a vertical tilt in the velocity structure. For both streamlines, buoyancy production around $R = 870$km can be seen at intermediate depths ($z = -800$m), suggesting a process of instability that is localized to near bottom isotherms that tilt rapidly in the along-slope direction.

a behavior expected for MKE since it lies above sloping bottom but not for EKE which lies downstream, away from sloping topography.

The along stream behavior of buoyancy production $\overline{w'b'}$, associated with the conversion of available potential energy into eddy kinetic energy by baroclinic instability, provides further insight into the vertical structure of the mean and eddying fields. Associated with the western intensified boundary current (Fig. 4.3a, at R=550km) there is a local maxima in buoyancy production, a sign of baroclinic instability associated with a bottom intensified topographic Rossby wave.

Buoyancy production shows another local maxima at intermediate depths associated with the instability of the cyclonic boundary current ($R \approx 900$km in Fig. 4.3b). Such local maxima is located below the local EKE maxima of the cyclonic boundary current and 100 km upstream (Fig. 4.2d at $R = 1000$ km). This suggests that eddies on the cyclonic boundary current are advected (or self advect) roughly 100km before these reach finite amplitude. Furthermore, buoyancy production implies growth by baroclinic instability (possibly a mix between barotropic baroclinic instability), a mechanism that requires the *relaxation* of tilting buoyancy/temperature surfaces in the across-stream direction and, thus, the presence of a cross-stream PV gradient.

Lateral PV gradients, in the quasigeostrophic (layer) approximation, can be approximated by cross-stream layer thickness gradients, with a layer defined by two isotherms. In what follows, we will look a layer with thickness defined by the isotherms $T_c = \{5.7, 6.2\}^\circ\ C$ (thick black contours in fig. 4.3a,b). At first glance, there appears to be a cross-stream thickness gradient by comparing the behavior of the isotherms in fig. 4.3a,b at $R = 800$km along two spatially separated streamlines $\psi = 1.5Sv$ (Fig. 4.3b) is east (closer to the eastern wall) from $\psi = 0.5$Sv (Fig. 4.3a).

To better understand the PV gradient at intermediate depths north of the ridge crest, we now look at zonal (constant y) section of the mean northward advective PV flux $\overline{\mathbf{J}}_A \cdot \mathbf{j}$ at 4 locations: A section along the ridge crest at $y = 500$km where the local maxima of $\overline{\mathbf{J}}_A$ is associated with the bottom intensified anticyclonic boundary current (Fig.4.4a), a section at $y = 550$km north of the ridge crest where the local maxima of $\overline{\mathbf{J}}_A$ is associated with the bottom intensified cyclonic boundary current (Fig.4.4b); another section upstream from the ridge at $y = 200$km (Fig.4.4c) and lastly a section at $y = 800$km far downstream from the ridge (Fig.4.4d). In all the sections we show the isotherms $T_c = \{5.7^\circ\ C, 6.2^\circ\ C\}$ that define the layer where there is baroclinic instability growth at mid depths downstream from the ridge crest.

At the section along $y = 550$km, the isotherms $T_c = \{5.7^\circ\ C, 6.2^\circ\ C\}$ incrop towards the sloping bottom topography, with the advective PV going to zero within the space (area)

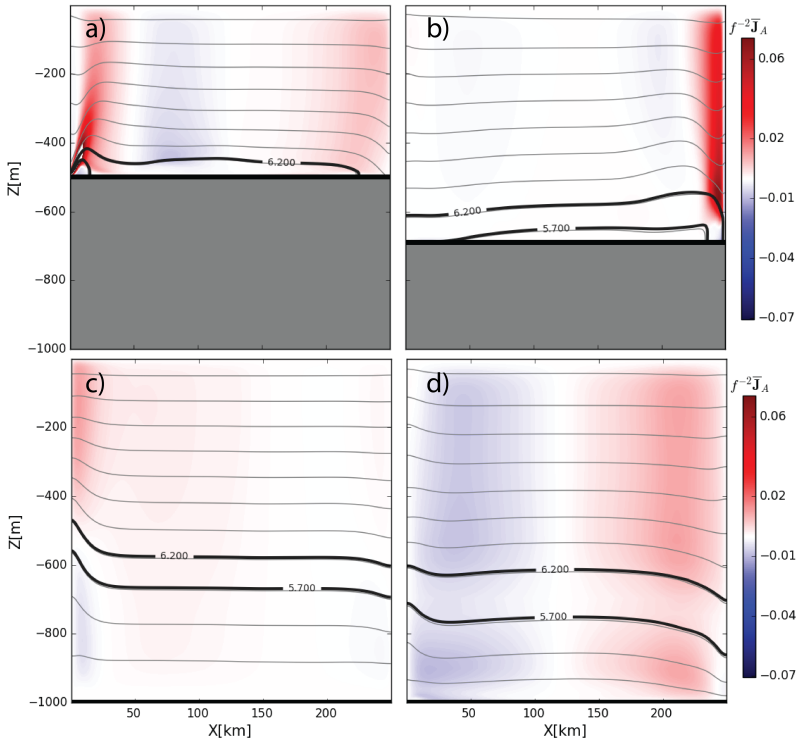

Figure 4.4: Zonal (x,z plane) sections of time-mean, northward advective potential vorticity flux ($\overline{vq}$) along the ridge crest (a) where the mean flow associated with the boundary current is strongest, at $y = 550$km where the northward flow associated with the cyclonic boundary current is strongest (b). In addition, section upstream at y=200km (c) and another downstream 800 km (d) from the ridge crest are shown. The location of the mean isotherms $\overline{T}_1 = 5.7^\circ\ C$ and $\overline{T}_2 = 6.2^\circ\ C$, are shown in thick black contours. The isotherms incrop towards the sloping bottom in the presence of the cyclonic boundary current (c,d), resulting in a layer with vanishing vertical stratification and vanishing potential vorticity flux.

bounded by these isotherms (z=600m, x=240km in fig. 4.4b). The mean advective PV can be approximate as $\overline{\mathbf{J}}_\mathbf{A} \approx \overline{vq}\hat{\mathbf{j}}$, since baroclinic growth takes place farther downstream. The vanishing of the mean advective PV is then associated with a vanishing mean (Ertel) potential vorticity $\overline{q} \approx 0$, given the observed isothermal tilts (thus vanishing stratification), and $\overline{v} \neq 0$, even within the bottom boundary layer (Fig. 4.2a).

The bottom and lateral (along-ridge) stratification within the incropping layer defined by isotherms $T_c = \{5.7^\circ\ C, 6.2^\circ\ C\}$ (in fig. 4.4b) resembles that of a mixed layer front within a

bottom boundary layer. The orientation of the bottom mixed layer front is associated with an across-slope flow, as opposed to along slope commonly used in idealized simulation of bottom boundary layer dynamics. Bottom mixed layer fronts within the bottom boundary layer with an orientation like the one observed in fig 4.4b must then be associated with a net along-slope (westward) Ekman driven transport of buoyancy/temperature anomalies, away from the eastern wall. The mean interior flow, is the cyclonic boundary current. The Ekman transport of warm water anomalies west, results in a convectively unstable stratification that promotes the formation of an incropping bottom mixed layer front.

Downstream from the ridge, the layer defined by the isotherms $T_c = \{5.7^\circ\, C, 6.2^\circ\, C\}$ shows a vanishing advective PV flow (Fig. 4.4d). Given the strong barotropic nature of the recirculation downstream from the ridge ($\overline{J}_A$ does not change sign in the vertical), this implies a vanishing of mean potential vorticity $\overline{q} \approx 0$ within the layer defined by the T_c-isotherms. Upstream from the ridge, the same layer defined by isotherms $T_c = \{5.7^\circ\, C, 6.2^\circ\, C\}$ has a lesser thickness, and while within this layer the $\overline{\mathbf{J}}_A \approx 0$, this is likely associated with the baroclinic behavior of the flow upstream, such that the northward velocity reverses sign there ($\overline{v} = 0$). Coincidentally, this level is set by the depth at the ridge crest $z = -500$m.

The presence of a vanishing PV anomaly within the layer defined by isotherms $T_c = \{5.7^\circ\, C, 6.2^\circ\, C\}$ downstream of the ridge, suggests the spreading of low PV watermasses, associated with the bottom boundary layer, in turn associated with the cyclonic boundary current. This becomes more evident by looking at the spatial distribution of mean potential vorticity across the ridge at the zonal section $x = 125km$ (Fig.4.5a). Downstream from the ridge, the layer defined by isotherms $T_c = \{5.7^\circ\, C, 6.2^\circ\, C\}$ shows a low PV anomaly (when compared to the PV values above of below). Given that PV cannot be changed within an isentropic surface [Haynes and McIntyre, 1987, 1990], the observed PV distribution must be associated with advective processes.

We now consider the isentropic PV (IPV) distribution along the $T_0 = 6.0^\circ C$ surface. The IPV shows a spread of low PV associated with the signature of bottom mixed layer frontal watermass into the interior (beginning at x=240km, y=500km in Fig. 4.5b), roughly in the

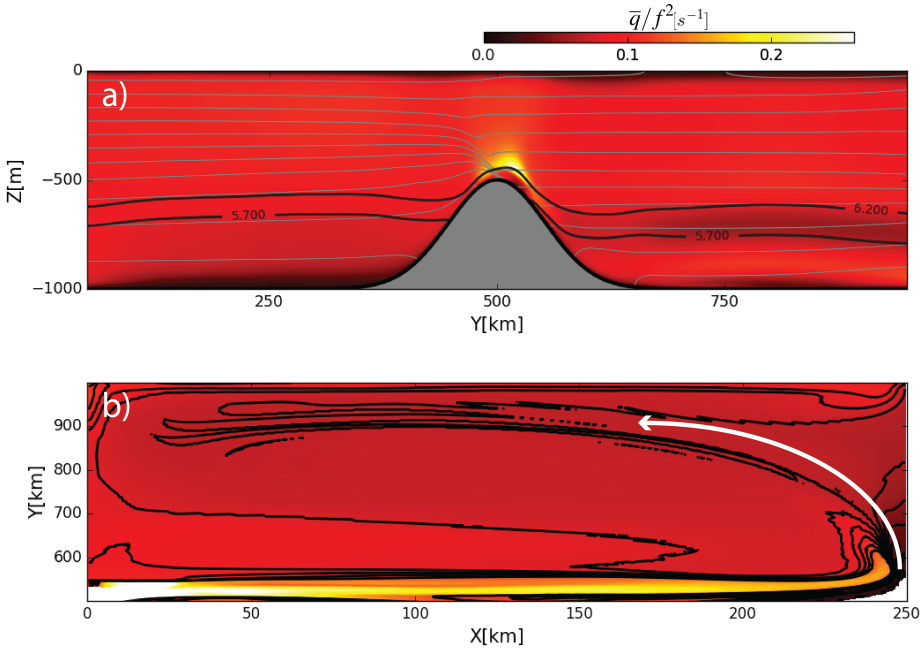

Figure 4.5: a) Cross-ridge spatial distribution of mean potential vorticity $\overline{q}$ at $x = 125$km, away from boundary currents, showing a low PV tongue north of the ridge crest, between isotherms $T_1 = 5.7$ and $T_2 = 6.2$. b) potential vorticity along isentrope $T_c = 6.0°\ C$ north of the ridge crest ($y > 500$km). This isentrope is located within the layer with low PV anomaly highlighted in a). Black contours now represent PV contours along the isentrope, showing the spread of low PV tongue associated with the mean cyclonic boundary current.

direction of the mean flow (white arrow). A snapshot of IPV along the same $T_0 = 6°\ C$ surface for day near the end of our (7 year) simulation shows eddies (dipoles) advecting low PV anomalies within their anticyclonic core, into the interior, away from their formation site (Fig. 4.6, at $x = 225$km, $y = 680$km). These eddies appear to be advected downstream by the mean flow, as well as rotate cyclonically, a sign of an unbalanced dipole with one core strong than the other [Manucharyan and Timmermans, 2013]. As the dipoles reach finite amplitude, these appear to get dissipated potentially by the strong shear of the mean (separating) boundary current.

IPV maps also show the advection of anomalous high PV along the ridge crest (Fig. 4.5, and Fig. 4.6). Advection of high PV anomalies is associated with the bottom intensified

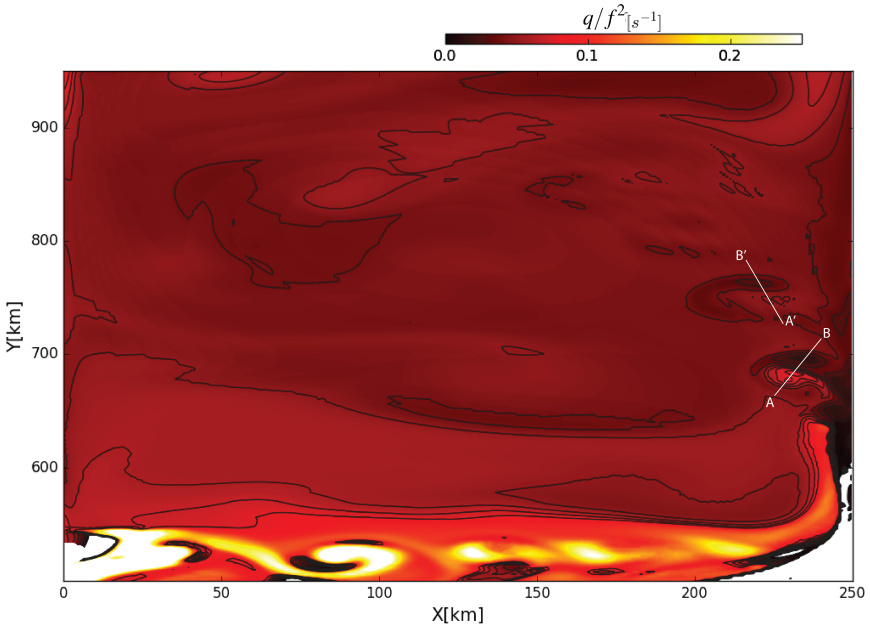

Figure 4.6: Snapshot of isentropic Ertel PV in simulation Cst_{ns} ($T_c = 6.0°$ C) north of the ridge crest ($y >$ 500km), located within the layer with low PV anomaly highlighted in Fig. 4.5a. Black contours represent PV levels $\overline{q}f^2 < 0.1$. Dipoles are continuously generated from the region of baroclinic instability growth $(240km, 600km)$, and advect low PV anomalies (anticyclonic vorticity) into the interior. A dipole can be seen at $(x, y) = (225km, 680km)$, with the line $\overline{AB}$ bisecting it. Dipole rotate cyclonically as they are advected by the mean flow, as shown by a second dipole downstream $(x, y) = (215km, 750km)$, where the line $\overline{A'B'}$ shows the respective orientation. Cyclonic (high PV) anomalies can be seen propagating along the ridge near the crest ($y =$ 550km), dissipating near the cyclonic boundary current ($x \approx 220km$).

baroclinic eddies, predominantly cyclonic (e.g. Fig.4.6 $x =$ 90km, $y =$ 550km) and along f/H contours.

4.3.1 Topographic PV Fluxes

The sources of PV anomalies shown in figs. 4.5 and 4.6 are associated with the interaction of the bottom-intensified flow with topography, and the local intersection of temperature/buoyancy surfaces with sloping bottom in regions of strong curvature of the mean flow (thus associated with alongstream depth changes). In this section we complement the

IPV and along-streamline analysis of the vertical structure of the mean and eddy fields, by presenting an (Eulerian) volume integrated PV budget (see Appendix D for a detailed description). Our previous analysis suggest net topographic PV fluxes to play an important role balancing the budget.

The control volume considered here is delimited by one cross channel section far upstream and another downstream from the ridge ($y = 100$km and $y = 900$km, both away from the imposed relaxation to flow variables). We calculate the volume integrated balance of PV in (4.1), which implies that for a sufficiently long time integration such that the LHS of (4.1) is vanishingly small, the evolution of PV is driven by boundary sources and interior redistribution (*e.g.* mean flow or eddy advection).

In all simulations the net northward PV flux is negative $\Delta_y(\overline{\mathbf{J}} \cdot \hat{\mathbf{j}}) < 0$, implying a larger (lateral) PV flux entering the control volume (upstream from the ridge) where $\Delta_y(\cdot) = (\cdot)_{y=M} - (\cdot)_{y=0}$ represents the difference in the integrated fluxes down and upstream. In addition, the dominant contribution to the net northward flux is advective *i.e.* $\Delta_y(\overline{\mathbf{J}} \cdot \hat{\mathbf{j}}) \approx \Delta_y(\overline{\mathbf{J}}_A \cdot \hat{\mathbf{j}}) < 0$ (Fig. 4.7). This net decrease in (advective) northward PV flux means there is a larger advective PV flux upstream towards the ridge. This agrees well with the observed spread of high PV watermasses along the ridge but not across, and the subsequent spread of low PV watermasses associated with the bottom boundary layer downstream from the ridge, that created a layer with vanishing PV and thus $\overline{\mathbf{J}}_A \approx 0$, thus decreasing the net northward advective flux.

The net loss of northward PV flux is approximately balanced by a net positive topographic PV flux ($\overline{J}_{bot} > 0$), in all simulations (Fig. 4.7) [1]. Thus

$$\Delta_y \overline{J}_A \approx -\overline{J}_{bot} \tag{4.15}$$

The positive value of the net topographic PV flux ($J_{bot} > 0$) can equally be interpreted as a net positive PV flux in the direction of $\hat{\mathbf{n}}_{bot}$ (*i.e.*outside control volume) or as a negative

[1]ROMS does not explicitly solve the integral PV equation (D.1) at every time-step. As a consequence, we don't expect that our integral PV budget will close exactly

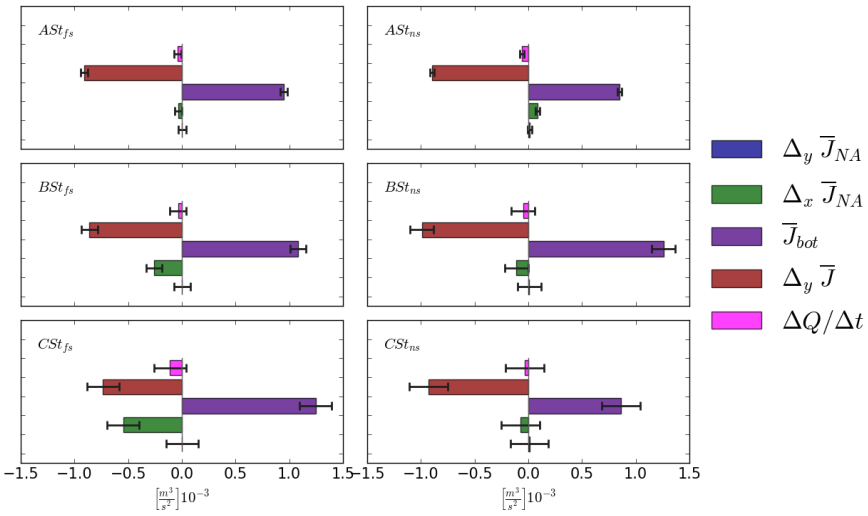

Figure 4.7: Integral PV balance (D.1) for all simulations. The error bars denote the residual error ($\pm\Delta$) in the balance. Note that the net northward dissipative PV flux ($\Delta_y \overline{J}_{NA}$) is vanishingly small in all simulation.

PV into the our control volume (*i.e.* in the direction of $-\hat{\mathbf{n}}_{\mathbf{bot}}$), through dissipative processes localized to the sloping bottom. This approximate balance in (4.15) is consistent the low PV anomaly originating at the bottom boundary layer over sloping bottom topography in the presence of the cyclonic boundary current. This is, the low PV anomaly redistributed (advected) into the interior downstream from the ridge in all simulations is associated with injection of low PV from the bottom boundary layer. This redistribution of low PV reduces the net advective PV flux downstream out of the control volume.

We now isolate the dominant contribution to the net topographic PV fluxes, following our derived decomposition as a sum of two terms in (4.3). We find that $\overline{J}^t_{bot}$ makes a vanishing contribution to the net flux in all simulations, so that $\overline{J}_{bot} \approx \overline{J}^s_{bot}$ (Fig. 4.8).

Rather than focusing on which term dominates the contribution, we focus on the spatial distribution along the ridge (f/H direction) of each individual term associated with the the second term in the rhs of (4.12). This is convenient given that the flow pattern is

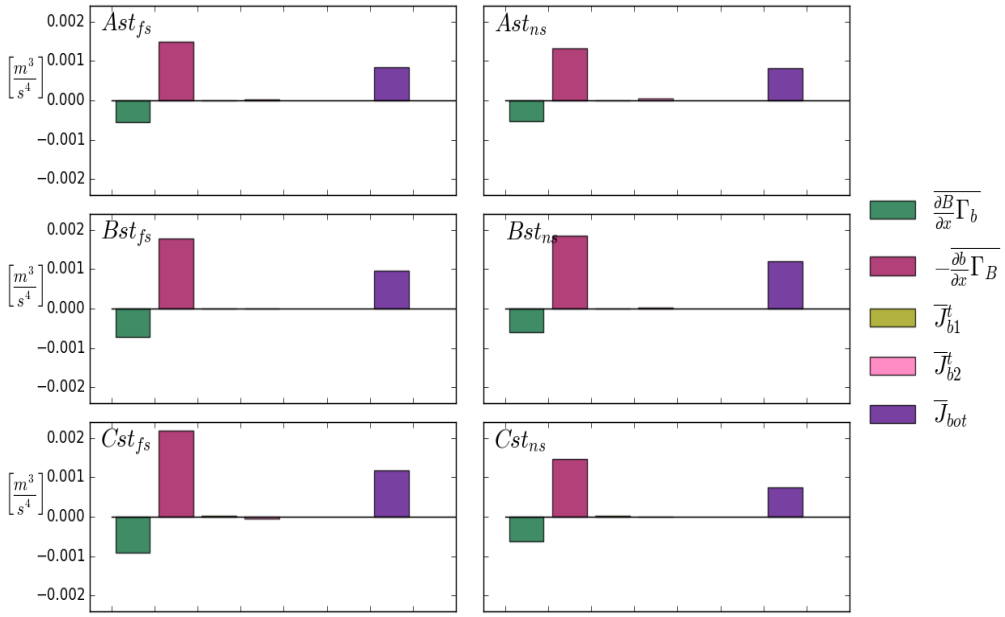

Figure 4.8: Net contributions of the terms in the decomposition of the net topographic potential vorticity flux $\overline{J}_{bot} = \overline{J}^t_{bot} + \overline{J}^s_{bot}$, where $\overline{J}^t_{bot} = \overline{J}^t_{b1} + \overline{J}^t_{b2}$ and $\overline{J}^s_{bot} = [\overline{B_x\Gamma_b} - \overline{b_x\Gamma_B}]h_y$ In all simulations, $\overline{J}^t_{bot} \approx 0$, making a vanishingly small contribution to the integral PV balance.

characterized by lateral boundary currents within a distance λ_M from lateral walls, and a region where the flow is roughly aligned with f/H contours. Thus, we divide topography into three regions, two associated with each lateral boundary current and one associated with the flow parallel to f/H contours, near the ridge crest. The dynamics associated with the mean flow along f/H contours best resembles idealized simulations of bottom boundary layers at a slope [MacCready and Rhines, 1991, Benthuysen and Thomas, 2012].

In all simulations, we find that the greatest contribution to the net topographic PV fluxes takes place within the region of influence of lateral boundary currents, where the mean flow departs greatly from f/H contours (Fig. 4.9 right panel, associated with simulation

Cst_{ns}, greatly discussed throughout this paper). Within the regions associated with lateral boundary currents, all variables except $\overline{\Gamma}_B dh/dy$, decay drastically away from the influence of lateral boundary currents. In the region associated with flow along f/H contours, the mean flow (and thus the bottom boundary layer) is located near the ridge crest where the bottom slope approaches zero, resulting in a buoyancy shutdown timescale much greater than the stratified, frictional spindown timescale, *i.e.* $\mathcal{T}_{shut} \gg \mathcal{T}_{spin}$ (see Table 3.2). This suggest that buoyancy effects within the bottom boundary layer are too slow to promote baroclinicity within the bottom boundary layer, and thus induce Ekman arrest. This further complements our earlier estimation of bottom intensified eddy variability of the bottom boundary layer thickness that further prevents buoyancy shutdown [Ruan and Thompson, 2016]. Thus, while we do observe downward Ekman transport within the bottom boundary layer (Fig. 4.10b), the vanishingly small contribution to the PV flux is likely associated with the location of the mean flow being close to the ridge crest, where the topographic slope almost vanishes, and eddy driven variability dominates.

Thus, we find that bottom boundary layer dynamics localized to the boundary currents are dominant in setting up the near bottom stratification that results in the observed net topographic PV and, furthermore, the injection of vanishingly low PV anomalies into interior mid-depth ocean, as the mean flow separates from the sloping bottom.

4.4 Discussions and Conclusions

We have presented in this study an analysis of the potential vorticity budget and the vertical structure of a rotating, stratified throughflow across finite amplitude topography under channel geometry. We found that bottom boundary layer dynamics localized to boundary currents promote the formation of *high* PV anomalies along an anticyclonic western boundary current, and a *low* PV anomaly associated with a eastern (*pseudo* westerward) cyclonic boundary current. The *high* PV anomaly is advected along topographic contours atop the ridge. Meanwhile, the vanishingly *low* PV anomaly, is advected downstream by the mean flow and eddies, resulting in a middepth isentropic layer characterized by watermasses with

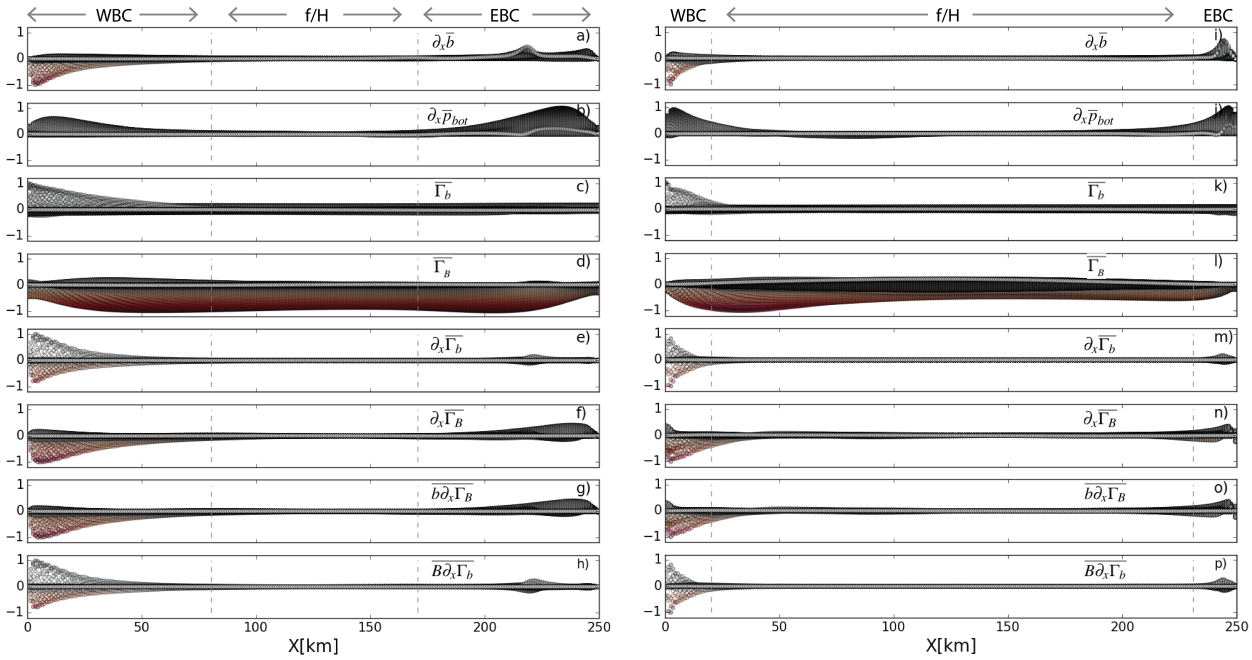

Figure 4.9: Along-ridge spatial variation of the terms associated with the second term in (4.12), a term in the decomposition of the topographic PV flux associated with the along f/H contributions (Left panels from simulations Ast_{ns} and right panel the terms from simulation Cst_{ns}). Denoted above the panels, shown by dashed vertical lines, are the regions of influence from western and eastern boundary currents (WBC and EBC), as well as the area where the flow is along f/H contours. All terms are normalized, and evaluated at 5m above the bottom, within the bottom boundary layer, and only taking into account values spanning the extent of the ridge ($400\ km < y < 600\ km$).

low PV. This injection of vanishingly *low* PV into the interior downstream from the ridge is driven by bottom boundary layer dynamics associated with the cyclonic boundary current, where Ekman transport within the bottom boundary layer promotes the formation of a bottom (incropping) mixed layer front within the boundary layer. Eddies that result from the instability of such front advect anomalous PV into the interior middepth.

Our choice of f-plane channel with lateral walls was made to isolate the dynamics to the ridge and, particularly, where the ridge intersects lateral walls. The choice of lateral walls is only appropriate when modelling large scale flows that separate from step continental margins or shelf breaks, particularly when the lateral scale of the flow (in this case roughly

determined by the half width of the ridge, *i.e.* width of sloping region $\sim 100km$) is much larger that the lateral scale of the continental margin or shelf break.

Our observed middepth eddy variability and subsequent eddy advection of low PV anomalies away from the middepth front, resembles the middepth boundary current of low potential vorticity studied in Spall et al. [2008]. There, eddies that grow from the middepth boundary current advect low PV waters into the interior. The major difference in our model is the significant mean flow advection into the interior, and the character of our flow: an equilibrated system. The equilibration of our throughflow allows us to quantify the net advective fluxes across the ridge that originate from the injection of vanishingly low PV waters from the bottom boundary layer, through a Eulerian PV volume budget.

The choice of lateral walls, however, does influence the orientation of the equilibrated bottom mixed layer front, which is perpendicular to isobaths, aligned with the mean (interior) flow. Such configuration was not explored by Wenegrat et al. [2018], where they only consider the effect of baroclinicity within a bottom boundary layer (similar to a mixed layer fronts) associated with along slope flow. Imposing a step sloping bottom instead of a lateral wall would still lead to net Ekman transport of warm water into the deep ocean, in the direction perpendicular to a cyclonic boundary current. Thus leading to convective instability and a middepth, incropping bottom mixed layer front, although the front now could potentially reside over the step shelf break rather than on the ridge crest. A step continental shelf break instead of a lateral wall could lead to a significant modification of the mean flow, however, since f/H contours would provide topographic Rossby waveguides along the shelf and prevent boundary current separation from the wall. Thus, while we believe the choice of lateral walls does not impact our main result of bottom boundary layer PV injection into the interior downstream from the ridge at middepths, it would likely impact the behavior on the mean equilibrated circulation, resembling previous studies of topographically steered, cyclonic basin scale circulation typical of the modeling of the Nordic seas [Nøst and Isachsen, 2003, Nøst et al., 2008, LaCasce et al., 2008, Spall, 2004]. An advantage of our model with respect to these studies, is that we allow dynamics within the bottom boundary layer to

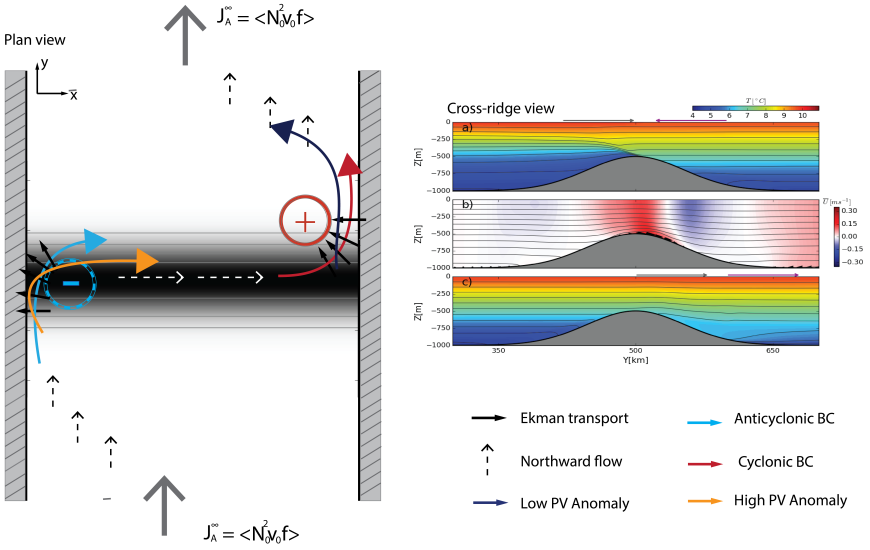

Figure 4.10: Diagram showing the plan view of the time-mean circulation with black dashed representing far upstream and downstream, and colored representing the location of the boundary currents (blue represents anticyclonic circulation, red cyclonic circulation). Thick black arrows show the location and direction of the bottom Ekman transport, resulting in upwelling of cold waters northward cross the ridge crest (a), and downwelling of water water northward associated with the cyclonic boundary current (c). Shown also is along-ridge flow ($\overline{u} > 0$ in the x-direction), and the associated bottom Ekman transport denoted by black arrows inducing downwelling along the slope. The stratification is shown by gray contours every 0.5° C. This system results in a net (positive) topographic PV flux that balances a negative northwards advective PV flux, characterized by anomalous low PV at middepths that is associated with mixed layer water below the cyclonic boundary (c at y=600km).

determine the vertical structure of the mean circulation.

A clear disadvantage of our study is the lack of surface forcing, *e.g.* destabilizing buoyancy forcing, which would drive a convective overturning circulation across the ridge crest characterized, in theory, by a baroclinic exchange across the ridge topography. Some particularly interesting question arise is such scenario, for example how the boundary and interior distribution of PV anomalies may change by introducing such effects. This is, could the injection of low PV waters be directed upstream with respect the direction of the throughflow (*i.e.* negative y), and thus model overflows? Also, whether a seasonal amplitude on the specification of destabilizing forcing and lateral transports can result in changes on the

intensity, or depth of the injection of bottom boundary layer PV anomalies into the interior downstream? This will be the subject of a separate study, where we will look at the top to bottom control on the exchange across finite amplitude topography.

Chapter 5

CONCLUSIONS

This dissertation has examined localized processes that can modify the baroclinic structure of rotating stratified flows across large amplitude topography that represent idealized models for the Atlantic inflow across the Iceland-Faroe Ridge.

5.1 Review of Chapter 2

We find agreement with the theoretical predictions for the development of mesoscale instability of the jet in the presence of sloping bottom topography, and we find the initial growth of surface mixed layer eddies is insensitive to topographic variations. However, during the finite amplitude phase of mixed layer instability, we find faster development of mesoscale eddies and thus a stronger cross-front eddy heat flux and residual circulation for the position of the jet where we found the faster growth of mesoscale baroclinic instability. Over an advective timescale that represents the transit time of a water parcel along the Iceland-Færæ Ridge, the resulting eddy heat flux is greatest in the cases where the frontal jet experiences the most destabilizing bottom topography of the three cases tested, with values comparable to the heat flux associated with the mean flow. Therefore, eddy dynamics over the IFR frontal region are important contributors to the heat exchanges between the North Atlantic and Nordic Seas, with bottom topography playing a key role in determining the largest eddy heat fluxes, whether the initial growth is dominated by mixed layer eddies, or mesoscale eddies.

5.2 Review of Chapters 3

We find that an along-stream modification of the stratification localized to boundary currents can be explained through Ekman suction/pumping and the frictional spindown of the current as it navigates the ridge. Associated with the anticyclonic boundary current, Ekman suction and frictional spindown promotes a strong stratification, and therefore modifies the vertical depth scale of topographic Rossby waves, the flow being more bottom confined. Associated with the cyclonic boundary current downstream from the ridge crest, Ekman pumping (of warm interior waters) and frictional spindown promotes advection of relatively warmer waters, that results in convective overturning and destratification of the water column, thus promoting a stronger barotropic behavior downstream from the ridge crest.

The modification by the bottom boundary layer results in an asymmetry of the flow response to the large amplitude topography, with the inflow experiencing less resistance to flow upslope into the ridge crest, than the resistance and required inertial torque for the inflow to move down the slope, and thus downstream from the ridge.

The relative location of the boundary currents with respect to the ridge crest further accentuates the observed asymmetry on the horizontal (barotropic) behavior of the throughflow across the ridge, since the anticyclonic boundary current is located much closer to the ridge crest. This also results in an asymmetry of the eddying field, with short-lived, cyclonic eddies along the ridge and dipole-like eddies downstream from the ridge, the latter evolving freely until eventually reaching barotropization due to nonlinear instability process, resulting in a strong basin-scale barotropic cyclonic circulation.

The observed modification in the baroclinic behavior across the ridge crest may provide an additional explanation to the preferred cyclonic circulation and strong along-slope topographic steering experienced by Atlantic waters as they flow north of the Greenland Scotland Ridge, since given the option, the flow downstream from the ridge crest will resist to flow across f/H contours, thus flowing along f/H contours following a prefered cyclonic circulation.

5.3 Review of Chapter 4

We find that bottom Ekman dynamics localized to lateral boundary currents restratify the bottom boundary layer, results in a strongly stratified front (thus a high PV anomaly) along the anticyclonic boundary current, and a low stratified (vanishingly low PV) mixed layer front localized to the cyclonic boundary current, analyzed in chapter 3 in terms of inertial torques and cross-slope flows.

PV anomalies are advected by both the mean flow and eddies resulting in a spatial distribution where high PV is concentrated along the ridge, and low PV is advected into the interior ocean at mid depths downstream from the ridge. The bottom incropping mixed layer front associated with the cyclonic boundary current has an effect on the vertical structure of the circulation downstream by injecting low PV associated with the mixed layer into the interior, downstream from the ridge. Such modification in our model resulted in the reduction of the strength of the circulation within the layer at which the low PV was injected, an important consequence given that the circulation was barotropic.

The observed middepth eddy variability and subsequent eddy advection of low PV anomalies away from the middepth front, resembles the middepth boundary current of low potential vorticity studied in Spall et al. [2008],

5.4 Future work

The surface dynamics examined in chapter 2 do not take into account the variability of the throughflow or that of the overflow plume south of the ridge crest, but do take into account for the transient nature of the Atlantic waters along the IFR. Therefore, it remains to be seen how well they represent an equilibrated frontal structure typical of the IFF. Chapters 3 and 4 do incorporate the throughflow, and therefore some aspects that relate to the IFF, but the absence of the frontal structure limits the results.

The dynamics in chapters 3 and 4 are robust, however, and the implications on the current downstream from the IFR, have sound basis, even in the case studied in chapter 2. This

is, eddies that generate from the IFF will experience barotropization as they recirculate and navigate the ridge, and merging of cyclonic eddies can result in larger cyclones that are more barotropic, as they are advected downstream from the ridge, into the nordic basin. The role of bottom friction on the Atlantic inflow, will largely depend on the bottom vertical shear relative orientation of the flow along f/H contours.

It would be very appealing to build upon chapters 3-4, by including convective overturning downstream. In the simplest, direct continuation to chapters 3 and 4, it would be very interesting to analyze the net meridional exchanges due to surface intensified eddies (no longer as constrained by bottom topography) and that of frictional spindown of the current (upwelling/downwelling favorable conditions). A question to ask would be, what is the net contribution by frictionally driven overflow waters along the ridge? How much of the transport is influenced by eddies? And, continuing with the results in chapters 3 and 4, what is the bottom pressure torque associated with each side of the ridge? Does the upslope transport still experiences less resistance than the downstream, downslope flow? What is the sensitivity to eddies and active bottom boundary layers? Do bottom intensified processes promote bottom mixed layer fronts?

Another potentially interesting question that I would like to address, is what is the role of the Faroe Bank channel overflow plume on the equilibration of the surface Atlantic inflow, as the overflow plume navigates the sloping bottom south of the IFR. Variability within the overflow plume, which depends on upstream conditions, may transfer momentum in the vertical through interfacial drag stresses, resulting in a modification of the net flow pattern of Atlantic waters into the IFR crest. Moreover, the variability of the transport and speed of the overflow plume over seasonal and decadal timescales may exert a net force of the upper ocean, therefore potentially modifying the character of the throughflow over such timescales.

An interesting approach to investigate the role of overflows on the net northward transport across the ridge would be to devise an modelling experiment in which overflow transport can be turn off and on, and the role of the transport, intensity and potential eddy variability of the overflow plume on the Atlantic inflow could be evaluated, from standard section along

the Faroe bank. While there has been some modeling efforts in this direction *i.e.* Spall [2004, 2010], such models focus on the dynamics of the convective basins without explicitly simulating the effect of overflows on the throughflow, nor exploring dynamics localized to the throughflow as it navigate a ridge.

BIBLIOGRAPHY

K. Aagaard and E. C. Carmack. The role of sea ice and other fresh water in the arctic circulation. *Journal of Geophysical Research: Oceans*, 94(C10):14485–14498, 1989.

J. Allen, D. Smeed, and A. Chadwick. Eddies and mixing at the iceland-færæ front. *Deep Sea Research Part I: Oceanographic Research Papers*, 41(1):51–79, 1994.

J. Badger and B. Hoskins. Simple initial value problems and mechanisms for baroclinic growth. *Journal of the atmospheric sciences*, 58(1):38–49, 2001.

P. G. Baines. *Topographic effects in stratified flows*. Cambridge University Press, 1998.

J. Barth. Stability of a coastal upwelling front: 1. model development and a stability theorem. *Journal of Geophysical Research: Oceans*, 94(C8):10844–10856, 1989.

N. Beaird, P. Rhines, and C. Eriksen. Overflow waters at the iceland–faroe ridge observed in multiyear seaglider surveys. *Journal of Physical Oceanography*, 43(11): 2334–2351, 2013.

N. Beaird, P. B. Rhines, and C. C. Eriksen. Observations of seasonal subduction at the iceland-faroe front. *Journal of Geophysical Research: Oceans*, 121(6):4026–4040, 2016.

J. Benthuysen and L. N. Thomas. Friction and diapycnal mixing at a slope: Boundary control of potential vorticity. *Journal of Physical Oceanography*, 42(9):1509–1523, 2012.

S. L. Blumsack and P. Gierasch. Mars: The effects of topography on baroclinic instability. *Journal of the Atmospheric Sciences*, 29(6):1081–1089, 1972.

G. Boccaletti, R. Ferrari, and B. Fox-Kemper. Mixed layer instabilities and restratification. *Journal of Physical Oceanography*, 37(9):2228–2250, 2007.

E. Boss, N. Paldor, and L. Thompson. Stability of a potential vorticity front: from quasi-geostrophy to shallow water. *Journal of Fluid Mechanics*, 315:65–84, 1996.

C. S. Bretherton and C. Schär. Flux of potential vorticity substance: A simple derivation and a uniqueness property. *Journal of the atmospheric sciences*, 50(12):1834–1836, 1993.

F. P. Bretherton. Critical layer instability in baroclinic flows. *Quarterly Journal of the Royal Meteorological Society*, 92(393):325–334, 1966.

C. Bringedal, T. Eldevik, Ø. Skagseth, M. A. Spall, and S. Østerhus. Structure and forcing of observed exchanges across the greenland–scotland ridge. *Journal of Climate*, 31(24):9881–9901, 2018.

K. H. Brink and S. J. Lentz. Buoyancy arrest and bottom ekman transport. part i: Steady flow. *Journal of Physical Oceanography*, 40(4):621–635, 2010.

J. Callies and R. Ferrari. Baroclinic instability in the presence of convection. *Journal of Physical Oceanography*, 48(1):45–60, 2018.

J. Callies, G. Flierl, R. Ferrari, and B. Fox-Kemper. The role of mixed-layer instabilities in submesoscale turbulence. *Journal of Fluid Mechanics*, 788:5–41, 2016.

L. Coachman and K. Aagaard. Transports through bering strait: Annual and interannual variability. *Journal of Geophysical Research: Oceans*, 93(C12):15535–15539, 1988.

S. A. Condie. Descent of dense water masses along continental slopes. *Journal of Marine Research*, 53(6):897–928, 1995.

B. Dickson, J. Meincke, and P. Rhines. Arctic–subarctic ocean fluxes: defining the role of the northern seas in climate. In *Arctic–Subarctic Ocean Fluxes*, pages 1–13. Springer, 2008.

E. T. Eady. Long waves and cyclone waves. *Tellus*, 1(3):33–52, 1949.

T. Eldevik and K. B. Dysthe. Spiral eddies. *Journal of Physical Oceanography*, 32(3): 851–869, 2002.

C. N. Flagg and R. C. Beardsley. On the stability of the shelf water/slope water front south of new england. *Journal of Geophysical Research: Oceans*, 83(C9):4623–4631, 1978.

A. D. Fox and S. J. Maskell. A nested primitive equation model of the iceland-faeroe front. *Journal of Geophysical Research: Oceans*, 101(C8):18259–18278, 1996.

C. Frankignoul, A. Czaja, and B. LHeveder. Air–sea feedback in the north atlantic and surface boundary conditions for ocean models. *Journal of climate*, 11(9):2310–2324, 1998.

A. Gill. Adjustment under gravity in a rotating channel. *Journal of Fluid Mechanics*, 77(3):603–621, 1976.

A. Gill. The hydraulics of rotating-channel flow. *Journal of Fluid Mechanics*, 80(4): 641–671, 1977.

J. Gula, M. J. Molemaker, and J. C. McWilliams. Gulf stream dynamics along the southeastern us seaboard. *Journal of Physical Oceanography*, 45(3):690–715, 2015.

R. Hallberg. Localized coupling between surface and bottom-intensified flow over topography. *Journal of physical oceanography*, 27(6):977–998, 1997.

R. Hallberg and A. Gnanadesikan. An exploration of the role of transient eddies in determining the transport of a zonally reentrant current. *Journal of Physical Oceanography*, 31(11):3312–3330, 2001.

R. Hallberg and P. B. Rhines. Boundary sources of potential vorticity in geophysical circulations. In *IUTAM Symposium on Developments in Geophysical Turbulence*, pages 51–65. Springer, 2000.

B. Hansen and J. Meincke. Eddies and meanders in the iceland-faroe ridge area. *Deep Sea Research Part A. Oceanographic Research Papers*, 26(9):1067IN11081–10801082, 1979.

B. Hansen and S. Østerhus. North atlantic–nordic seas exchanges. *Progress in Oceanography*, 45(2):109–208, 2000.

B. Hansen, S. Østerhus, H. Hátún, R. Kristiansen, and K. M. H. Larsen. The iceland–faroe inflow of atlantic water to the nordic seas. *Progress in Oceanography*, 59(4): 443–474, 2003.

B. Hansen, S. Østerhus, W. R. Turrell, S. Jónsson, H. Valdimarsson, H. Hátún, and S. M. Olsen. The inflow of atlantic water, heat, and salt to the nordic seas across the greenland–scotland ridge. In *Arctic–Subarctic Ocean Fluxes*, pages 15–43. Springer, 2008.

B. Hansen, H. Hátún, R. Kristiansen, S. Olsen, and S. Østerhus. Stability and forcing of the iceland-faroe inflow of water, heat, and salt to the arctic. *Ocean Science*, 6(4): 1013–1026, 2010.

P. Haynes and M. McIntyre. On the evolution of vorticity and potential vorticity in the presence of diabatic heating and frictional or other forces. *Journal of the Atmospheric Sciences*, 44(5):828–841, 1987.

P. Haynes and M. McIntyre. On the conservation and impermeability theorems for potential vorticity. *Journal of the atmospheric sciences*, 47(16):2021–2031, 1990.

E. Heifetz, P. Alpert, and A. Da Silva. On the parcel method and the baroclinic wedge of instability. *Journal of the atmospheric sciences*, 55(5):788–795, 1998.

K. R. Helfrich and L. J. Pratt. Rotating hydraulics and upstream basin circulation. *Journal of Physical Oceanography*, 33(8):1651–1663, 2003.

A. J. Hermann, P. B. Rhines, and E. Johnson. Nonlinear rossby adjustment in a channel: beyond kelvin waves. *Journal of Fluid Mechanics*, 205:469–502, 1989.

R. D. Hetland. Suppression of baroclinic instabilities in buoyancy-driven flow over sloping bathymetry. *Journal of Physical Oceanography*, 47(1):49–68, 2017.

P. E. Isachsen. Baroclinic instability and eddy tracer transport across sloping bottom topography: How well does a modified eady model do in primitive equation simulations? *Ocean Modelling*, 39(1):183–199, 2011.

P. K. Jakobsen, M. H. Ribergaard, D. Quadfasel, T. Schmith, and C. W. Hughes. Near-surface circulation in the northern north atlantic as inferred from lagrangian drifters: Variability from the mesoscale to interannual. *Journal of Geophysical Research: Oceans*, 108(C8), 2003.

S. Jónsson. Volume flux and fresh water transport associated with the east icelandic current. *Progress in Oceanography*, 73(3-4):231–241, 2007.

J. LaCasce, O. Nøst, and P. Isachsen. Asymmetry of free circulations in closed ocean gyres. *Journal of Physical Oceanography*, 38(2):517–526, 2008.

W. G. Large, J. C. McWilliams, and S. C. Doney. Oceanic vertical mixing: A review and a model with a nonlocal boundary layer parameterization. *Reviews of Geophysics*, 32(4):363–403, 1994.

R. J. LeVeque. *Finite difference methods for ordinary and partial differential equations: steady-state and time-dependent problems*, volume 98. Siam, 2007.

M. S. Lozier and M. S. Reed. The influence of topography on the stability of shelfbreak fronts. *Journal of physical oceanography*, 35(6):1023–1036, 2005.

P. MacCready. Frictional decay of abyssal boundary currents. *Journal of marine research*, 52(2):197–217, 1994.

P. MacCready and P. B. Rhines. Buoyant inhibition of ekman transport on a slope and its effect on stratified spin-up. *Journal of Fluid Mechanics*, 223:631–661, 1991.

P. MacCready and P. B. Rhines. Slippery bottom boundary layers on a slope. *Journal of Physical Oceanography*, 23(1):5–22, 1993.

P. MacCready and P. B. Rhines. Meridional transport across a zonal channel: Topographic localization. *Journal of physical oceanography*, 31(6):1427–1439, 2001.

G. E. Manucharyan and M.-L. Timmermans. Generation and separation of mesoscale eddies from surface ocean fronts. *Journal of Physical Oceanography*, 43(12):2545–2562, 2013.

J. Marshall and F. Schott. Open-ocean convection: Observations, theory, and models. *Reviews of Geophysics*, 37(1):1–64, 1999.

S. Maskell, A. Heathershaw, and C. Stretch. Topographic and eddy effects in a primitive equation model of the iceland-faeroes front. *Journal of marine systems*, 3(4-5):343–380, 1992.

A. J. Miller, P.-M. Poulain, A. Warn-Varnas, H. G. Arango, A. R. Robinson, and W. G. Leslie. Quasigeostrophic forecasting and physical processes of iceland-faroe frontal variability. *Journal of physical oceanography*, 25(6):1273–1295, 1995.

O. A. Nøst and P. E. Isachsen. The large-scale time-mean ocean circulation in the nordic seas and arctic ocean estimated from simplified dynamics. *Journal of Marine Research*, 61(2):175–210, 2003.

O. A. Nøst, J. Nilsson, and J. Nycander. On the asymmetry between cyclonic and anticyclonic flow in basins with sloping boundaries. *Journal of Physical Oceanography*, 38(4):771–787, 2008.

S. Østerhus, W. R. Turrell, S. Jónsson, and B. Hansen. Measured volume, heat, and salt fluxes from the atlantic to the arctic mediterranean. *Geophysical Research Letters*, 32(7), 2005.

J. Pedlosky. An overlooked aspect of the wind-driven oceanic circulation. *Journal of Fluid Mechanics*, 32(04):809–821, 1968.

J. Pedlosky. *Geophysical fluid dynamics*. Springer Science & Business Media, 2013a.

J. Pedlosky. *Waves in the ocean and atmosphere: introduction to wave dynamics*. Springer Science & Business Media, 2013b.

O. Phillips. On flows induced by diffusion in a stably stratified fluid. In *Deep Sea Research and Oceanographic Abstracts*, volume 17, pages 435–443. Elsevier, 1970.

R. A. Plumb and R. Ferrari. Transformed eulerian-mean theory. part i: Nonquasi-geostrophic theory for eddies on a zonal-mean flow. *Journal of Physical Oceanography*, 35(2):165–174, 2005.

M. D. Prater and T. Rossby. Observations of the faroe bank channel overflow using bottom-following rafos floats. *Deep Sea Research Part II: Topical Studies in Oceanography*, 52(3):481–494, 2005.

L. Pratt. On inertial flow over topography. part 1. semigeostrophic adjustment to an obstacle. *Journal of Fluid Mechanics*, 131:195–218, 1983.

L. Pratt. On inertial flow over topography. part 2. rotating-channel flow near the critical speed. *Journal of Fluid Mechanics*, 145:95–110, 1984.

L. Pratt and P. Lundberg. Hydraulics of rotating strait and sill flow. *Annual Review of Fluid Mechanics*, 23(1):81–106, 1991.

L. L. Pratt and J. A. Whitehead. *Rotating hydraulics: nonlinear topographic effects in the ocean and atmosphere*, volume 36. Springer Science & Business Media, 2007.

D. Quadfasel and R. Käse. Present-day manifestation of the nordic seas overflows. *Ocean Circulation: Mechanisms and Impacts-Past and Future Changes of Meridional Overturning*, pages 75–89, 2013.

M. K. Reszka, G. E. Swaters, and B. R. Sutherland. Instability of abyssal currents in a continuously stratified ocean with bottom topography. *Journal of physical oceanography*, 32(12):3528–3550, 2002.

P. Rhines. Edge-, bottom-, and rossby waves in a rotating stratified fluid. *Geophysical and Astrophysical Fluid Dynamics*, 1(3-4):273–302, 1970.

P. Rhines, S. Häkkinen, and S. A. Josey. Is oceanic heat transport significant in the climate system? In *Arctic–subarctic ocean fluxes*, pages 87–109. Springer, 2008.

P. B. Rhines. Geostrophic turbulence. *Annual Review of Fluid Mechanics*, 11(1): 401–441, 1979.

A. Roach, K. Aagaard, C. Pease, S. Salo, T. Weingartner, V. Pavlov, and M. Kulakov. Direct measurements of transport and water properties through the bering strait. *Journal of Geophysical Research: Oceans*, 100(C9):18443–18457, 1995.

T. Rossby and C. Flagg. Direct measurement of volume flux in the faroe-shetland channel and over the iceland-faroe ridge. *Geophysical Research Letters*, 39(7), 2012.

T. Rossby, M. Prater, and H. Søiland. Pathways of inflow and dispersion of warm waters in the nordic seas. *Journal of Geophysical Research: Oceans*, 114(C4), 2009.

X. Ruan and A. F. Thompson. Bottom boundary potential vorticity injection from an oscillating flow: A pv pump. *Journal of Physical Oceanography*, 46(11):3509–3526, 2016.

R. Samelson and D. Chapman. Evolution of the instability of a mixed-layer front. *Journal of Geophysical Research: Oceans*, 100(C4):6743–6759, 1995.

C. Schär. A generalization of bernoulli's theorem. *Journal of the atmospheric sciences*, 50(10):1437–1443, 1993.

T. Schneider, I. M. Held, and S. T. Garner. Boundary effects in potential vorticity dynamics. *Journal of the atmospheric sciences*, 60(8):1024–1040, 2003.

A. F. Shchepetkin and J. C. McWilliams. The regional oceanic modeling system (roms): a split-explicit, free-surface, topography-following-coordinate oceanic model. *Ocean Modelling*, 9(4):347–404, 2005.

A. J. Simmons and B. J. Hoskins. The life cycles of some nonlinear baroclinic waves. *Journal of the Atmospheric Sciences*, 35(3):414–432, 1978.

E. D. Skyllingstad and R. Samelson. Baroclinic frontal instabilities and turbulent mixing in the surface boundary layer. part i: Unforced simulations. *Journal of Physical Oceanography*, 42(10):1701–1716, 2012.

R. J. Small, J. Bacmeister, D. Bailey, A. Baker, S. Bishop, F. Bryan, J. Caron, J. Dennis, P. Gent, H.-m. Hsu, et al. A new synoptic scale resolving global climate simulation using the community earth system model. *Journal of Advances in Modeling Earth Systems*, 6(4):1065–1094, 2014.

Y. T. Song and D. G. Wright. A general pressure gradient formulation for ocean models. part ii: Energy, momentum, and bottom torque consistency. *Monthly Weather Review*, 126(12):3231–3247, 1998.

M. A. Spall. Frontogenesis, subduction, and cross-front exchange at upper ocean fronts. *Journal of Geophysical Research: Oceans*, 100(C2):2543–2557, 1995.

M. A. Spall. Boundary currents and watermass transformation in marginal seas. *Journal of physical oceanography*, 34(5):1197–1213, 2004.

M. A. Spall. Dynamics of downwelling in an eddy-resolving convective basin. *Journal of Physical Oceanography*, 40(10):2341–2347, 2010.

M. A. Spall, R. S. Pickart, P. S. Fratantoni, and A. J. Plueddemann. Western arctic shelfbreak eddies: Formation and transport. *Journal of Physical Oceanography*, 38(8): 1644–1668, 2008.

A. Stewart and A. Thompson. The neutral density temporal residual mean overturning circulation. *Ocean Modelling*, 90:44–56, 2015.

P. H. Stone. On non-geostrophic baroclinic stability. *Journal of the Atmospheric Sciences*, 23(4):390–400, 1966.

A. Tandon and C. Garrett. Mixed layer restratification due to a horizontal density gradient. *Journal of Physical Oceanography*, 24(6):1419–1424, 1994.

A. Tandon and C. Garrett. Geostrophic adjustment and restratification of a mixed layer with horizontal gradients above a stratified layer. *Journal of physical oceanography*, 25 (10):2229–2241, 1995.

S. A. Thorpe. Current and temperature variability on the continental slope. *Philosophical Transactions of the Royal Society of London. Series A, Mathematical and Physical Sciences*, 323(1574):471–517, 1987.

J. Trowbridge and S. Lentz. Asymmetric behavior of an oceanic boundary layer above a sloping bottom. *Journal of Physical Oceanography*, 21(8):1171–1185, 1991.

G. K. Vallis. *Atmospheric and oceanic fluid dynamics*. Cambridge University Press, 2017.

A. Wåhlin and G. Walin. Downward migration of dense bottom currents. *Environmental Fluid Mechanics*, 1(2):257–279, 2001.

J. O. Wenegrat, J. Callies, and L. N. Thomas. Submesoscale baroclinic instability in the bottom boundary layer. *Journal of Physical Oceanography*, 48(11):2571–2592, 2018.

J. Whitehead. Critical control by topography-deep passages, straits and shelf fronts. *Topographic Effects in the Ocean*, pages 141–156, 1995.

J. Whitehead, A. Leetmaa, and R. Knox. Rotating hydraulics of strait and sill flows. *Geophysical and Astrophysical Fluid Dynamics*, 6(2):101–125, 1974.

C. Wunsch. On oceanic boundary mixing. In *Deep Sea Research and Oceanographic Abstracts*, volume 17, pages 293–301. Elsevier, 1970.

J. Yang and J. F. Price. Water-mass formation and potential vorticity balance in an abyssal ocean circulation. *Journal of marine research*, 58(5):789–808, 2000.

J. Yang and J. F. Price. Potential vorticity constraint on the flow between two basins. *Journal of Physical Oceanography*, 37(9):2251–2266, 2007.

Appendix A

ANALYTICAL EXPRESSIONS FOR TOPOGRAPHY AND INITIAL TEMPERATURE CONDITIONS

A.0.1 Bottom Topography

Topography is constructed by matching two reference profiles in order to construct a symmetric ridge.

$$h(y) = h_{_{NA}}\mathcal{H}(y - y_0) + h_{_{NO}}\mathcal{H}(y + y_0) \tag{A.1}$$

where $\mathcal{H}$ is the Heaviside function centered at $y = y_0$, and $h_{_{NA}}, h_{_{NO}}$ are the topographic profiles on the southern and northern flanks, respectively. These are given by

$$h_{_{NA}} = \frac{H_0}{2} + \Delta h \left(1 - \tanh\left(\frac{y - y_1}{L_{_T}}\right)\right) \tag{A.2}$$

and

$$h_{_{NO}} = H_0 - \Delta h \left(1 - \tanh\left(\frac{y - y_2}{L_{_T}}\right)\right) \tag{A.3}$$

y_1, y_2 center the respective topographic profiles, with $y_1 < y_0 < y_2$. $L_{_T}$ sets the deformation scale of bottom topography at $y = y_1$ and $y = y_2$. $H_0 = 1000$m is the depth far away from the ridge and $\Delta h = 250$m represents half the topographic amplitude.

A.0.2 Temperature

The initial temperature is constructed by matching two reference temperature distributions, associated with the southern and the northern flank of the ridge respectively. That is

$$T(y,z) = T_{_{NA}}\mathcal{H}(y-y_0) + T_{_{NO}}\mathcal{H}(y+y_0) \tag{A.4}$$

$T_{_{NA}}$ represents the temperature on the southern flank. $T_{_{NA}}$ mimics bottom topography with the isotherms closely following the bottom sloping topography so that the slope parameter $\delta \longrightarrow 1^{-}$ (approaches 1 from negative values). T_{NA} is given by

$$T_{_{NA}} = T_0 + \Delta T \tanh\left(\frac{z+\mathcal{Z}_1(y)}{\delta h}\right) \tag{A.5}$$

$$\mathcal{Z}_1(y) = 1 - \beta \tanh\left(\frac{y-y_1^*}{L_f}\right) \tag{A.6}$$

On the northern flank, the temperature front outcrops at the surface over the sloping bottom so that the slope parameter $\delta \rightarrow -1^{+}$ (approaches -1 from positive values). On the Northern flank, the temperature distribution $T_{_{NO}}$ is given by

$$T_{_{NO}}(y,z) = T_{_0} + \Delta T \tanh\left(\frac{z+\mathcal{Z}_2(y)}{\delta h}\right) \tag{A.7}$$

$$\mathcal{Z}_2(y) = \frac{1}{2} - \tanh\left(\frac{y-y_2^*}{L_f}\right) \tag{A.8}$$

Appendix B

RELATIVE VORTICITY AND THE BAROTROPIC VORTICITY

In the presence of large amplitude topography (such that $|\nabla h| >> |\nabla \eta|$), the barotropic vorticity can be expressed in terms of the component of the vertically integrated vector vorticity that is perpendicular to the bottom surface (Fig. 3.1). This is

$$\Omega = -\mathbf{n}_{bot} \cdot \left[\int_z^0 \boldsymbol{\omega} d\xi \right] \Big|_{z=-h} \tag{B.1}$$

where $-\mathbf{n}_{bot} = \nabla h + \hat{\mathbf{k}}$ is the vector normal to bottom topography (upward pointing) and $\boldsymbol{\omega} = (-v_z, u_z, \zeta)$ is the vorticity vector in the primitive equations. Thus, in the case of flat bottom $-\mathbf{n}_{bot} = \hat{\mathbf{k}}$ and thus $\Omega = H_0 \zeta$, H_0 being the (constant) total depth. In such scenario, the barotropic vorticity and relative vorticity are proportional to each other.

In the primitive equations, the evolution of the barotropic vorticity is then given by

$$\frac{\partial \Omega}{\partial t} = -\mathbf{n}_{bot} \cdot \left[\frac{\partial}{\partial t} \int_z \boldsymbol{\omega} \, d\xi \right] \Big|_{z=-h} \tag{B.2}$$

or equivalently

$$\frac{\partial \Omega}{\partial t} = \left[\int_z \frac{\partial \zeta}{\partial t} d\xi - \frac{\partial \mathbf{u}_h}{\partial t} \times \nabla h \right] \Big|_{z=-h} \tag{B.3}$$

The first term on the right hand side of (B.3) can be obtained from the vertical component of the vorticity equation, while all the others are associated with the vertical integration of the horizontal vorticity equations, and can be obtained from the momentum equations. In the primitive equations, the horizontal momentum and vertical vorticity equations are given by

$$\frac{\partial \mathbf{u}_h}{\partial t} + (\omega_a \times \mathbf{u})_h = -\nabla_h B + \mathbf{F}_h \tag{B.4}$$

$$\frac{D\zeta}{Dt} = (\boldsymbol{\omega_a} \cdot \nabla)\, w + \nabla_h \times \mathbf{F}_h \tag{B.5}$$

where $\mathbf{F}_h$ represents dissipation of horizontal momentum, and $B = \frac{1}{2}\mathbf{u}_h^2 + g(\eta - z) + p'/\rho_0$ is the Bernoulli potential, with $p(x, y, z, t)$ the hydrostatic pressure due to interior stratification. As a result of the primitive equations not incorporating non-hydrostatic terms, only the horizontal component of the vortex force $(\omega_a \times \mathbf{u})_h$ appears in the momentum equations, and is no longer perpendicular to the absolute vorticity ($\boldsymbol{\omega}_a = \boldsymbol{\omega} + f\hat{\mathbf{k}}$, f being the Coriolis parameter), nor the velocity vector.

Writing (B.5) in flux form and then integrating in the vertical, we have

$$\frac{\partial <\zeta>}{\partial t} = -\nabla_h \cdot <\mathbf{J}_\zeta> + \left(\mathbf{J}_\zeta \Big|_{z=-h}\right) \cdot \nabla h \tag{B.6}$$

where the flux vector $\mathbf{J}_\zeta$ is given by

$$\mathbf{J}_\zeta = \underbrace{\mathbf{u}_h\,(f+\zeta) - [w\boldsymbol{\omega}_a]_h}_{\mathbf{J}_{\zeta_A}} + \underbrace{\hat{\mathbf{k}} \times \mathbf{F}_h}_{\mathbf{J}_{\zeta_{NA}}} \tag{B.7}$$

In the absence of stratification and vertical shear, $\mathbf{J}_\zeta \equiv \mathbf{u}_h(f+\zeta) + \hat{\mathbf{k}} \times \mathbf{F}_h$, the vorticity flux vector in the *shallow water equations* that is associated with conservation of potential vorticity substance ((Haynes and McIntyre, 1987, 1990)).

The contribution from the vertical integration of the horizontal vorticity vector is given by the cross-product between the time rate of change of the horizontal momentum and the gradient of the bottom terrain. Using (B.4) and (B.7), the cross-product (before evaluation) is

$$\frac{\partial \mathbf{u}_h}{\partial t} \times \nabla h = -\left(\hat{\mathbf{k}} \times \mathbf{J}_\zeta\right) \times \nabla h - \nabla_h B \times \nabla h \tag{B.8}$$

Expanding the triple cross product in (B.8), we have $(\hat{\mathbf{k}} \times \mathbf{J}_\zeta) \times \nabla h = -\mathbf{J}_\zeta \cdot \nabla h$. In addition, provided h is a smooth (continuously differentiable) function over the domain, $\nabla_h B \times \nabla h = -\nabla_h \cdot \left(\hat{\mathbf{k}} \times B \nabla h\right)$. Thus, we have

$$\frac{\partial \mathbf{u}_h}{\partial t} \times \nabla h = \mathbf{J}_\zeta \cdot \nabla h + \nabla_h \cdot \left(\hat{\mathbf{k}} \times B \nabla h\right) \tag{B.9}$$

Substracting (B.9) and (B.6), we get the equation

$$\frac{\partial \Omega}{\partial t} = \frac{\partial (B_{bot}, h)}{\partial (x, y)} - \nabla_h \cdot \mathbf{J}_\Omega \tag{B.10}$$

where the barotropic vorticity flux vector $\mathbf{J}_\Omega$ is

$$\mathbf{J}_\Omega = < \mathbf{J}_A > + \hat{\mathbf{k}} \times \left(< \mathbf{F}_h > + \frac{\boldsymbol{\tau}_s - \boldsymbol{\tau}_{bot}}{\rho_0} \right) \tag{B.11}$$

Appendix C

SUCCESIVE OVER RELAXATION

Solving for the streamfunction requires inverting the boundary value problem,

$$\nabla^2\psi = f(x,y) \tag{C.1}$$

with inflow (y=0) and outflow (y=M) boundary conditions

$$\psi(x,0) = \psi(0,0) + \int^x v(\xi,0)d\xi, \tag{C.2}$$

$$\psi(x,M) = \psi(0,M) + \int^x v(\xi,M)d\xi \tag{C.3}$$

Given that lateral walls are impermeable, then the reminding boundary conditions are

$$\psi(0,y) = 0, \quad \psi(L,y) = \int^L v(\xi,y)h(\xi,y)d\xi \tag{C.4}$$

Given the value of ψ at y=0 $\psi(L,0) = \psi(L,y) = (g\gamma/f)Lh(L,0) \approx 3$ Sv. With this, the method of inversion we use is the *Succesive Overrelaxation Method* ((LeVeque, 2007)), an iterative method that follows

$$\psi_{i,j}^{[k+1]} = \frac{\omega_{opt}}{2(\Delta_x^2+\Delta_y^2)}\left[\Delta_y^2\left(\psi_{i+1,j}^{[k]}+\psi_{i-1,j}^{[k]}\right)+\Delta_x^2\left(\psi_{i,j+1}^{[k]}+\psi_{i,j-1}^{[k]}\right)-(\Delta_x\Delta_y)^2 f_{i,j}\right]+(1-\omega_{opt})\psi_{i,j}^{[k]} \tag{C.5}$$

where ω_{opt} is a scalar *relaxation* parameter that for the Laplace operator $\omega_{opt} = 2/(1+\sin(\Delta\pi))$, where $\Delta = \max(\Delta_x,\Delta_y)$, with $\Delta_x = dx/L$ and $\Delta_y = dy/M$ the discretized distances.

Appendix D

INTEGRAL PV BALANCE

D.0.1 Integral Constrains

Consider a rectangular channel geometry with dimensions $(0 \leq x \leq L) \times (0 \leq y \leq M) \times (-h(y) \leq z \leq \eta)$, where $z = -h(y)$ is a finite-amplitude, meridionally isolated ridge, that is symmetric around $y = M/2$. A stratified flow across the ridge is driven by lateral boundary inflow/outflow that equivalent to a constant, large-scale surface pressure gradient across the ridge. We analyze the constrains the ridge has on the transport streamfunction and potential vorticity of the fluid. To better get a sense of the 3D character of the flow, we integrate the potential vorticity equation (4.1) over the channel domain, yielding an integral balance that incorporates both boundary sources and interior changes over a time interval. The time averaged integral equation is given by

$$\underbrace{\int_{A_I} \left[(\overline{\mathbf{J}} \cdot \hat{\mathbf{n}})\big|_{y=0} + (\overline{\mathbf{J}} \cdot \hat{\mathbf{n}})\big|_{y=M} \right] dA_I}_{\text{Net Northward PV flux}} + \underbrace{\int_{A_{II}} \left[(\overline{\mathbf{J}}_{NA} \cdot \hat{\mathbf{n}})\big|_{x=0} + (\overline{\mathbf{J}}_{NA} \cdot \hat{\mathbf{n}})\big|_{x=L} \right] dA_{II}}_{\text{Net Dissipative PV flux}} = -\frac{\Delta Q}{\Delta t} - \underbrace{\int_{A_{bot}} \overline{\mathbf{J}}_{bot} dA_{bot}}_{\text{Net Topographic PV flux}} \tag{D.1}$$

where the limits of integration on the left hand side are $A_I = (0 \leq x \leq L) \times (-h \leq z \leq \eta)$ and $A_{II} = (0 \leq y \leq M) \times (-h \leq z \leq \eta)$, the term ΔQ is the (mean) change of the volume integrated potential vorticity ($Q = \int_V q dV$) over time, and the integral term on the right hand side is taken over all variable bottom topography with area A_{bot}, where $\mathbf{J}_{bot} = \mathbf{J} \cdot \hat{\mathbf{n}}_{bot}$, with $\hat{\mathbf{n}}_{bot}$ the unit normal vector to bottom topography (outward-pointing). The integral

balance in (D.1) does not include surface PV fluxes due to the original assumption of no surface dissipative or diabatic forcing.

The time mean potential vorticity integral balance (D.1) states that as the flow moves across finite amplitude topography, a net flux of PV due to lateral fluxes must be balanced by a net change of volume integrated PV, or a net flux of potential vorticity through bottom topography. Net lateral flux PV fluxes can take place as a result of a net northward flux (first integral term in D.1), denoted from now on as $\Delta_y \overline{J}$, where $\overline{J} = \int_{A_I} \overline{\mathbf{J}} \cdot \mathbf{n} \; dA_I$ and $\Delta_y f = f(y = M) - f(y = 0)$, or a net dissipative PV flux through lateral walls, the second integral term on left hand side of (D.1), denoted as $\Delta_x \overline{J}_{NA}$.

The dissipative potential vorticity flux normal to a lateral wall is independent of horizontal stratification in the primitive equations, despite $b_y \neq 0$, resulting in the *net dissipative lateral PV flux* given by

$$\Delta_x \overline{J}_{NA} = \int_{A_{II}} \left[\left(\overline{b_z \mathbf{F}^y} \right) \Big|_{x=L} - \left(\overline{b_z \mathbf{F}^y} \right) \Big|_{x=0} \right] \; dA_{II} \tag{D.2}$$

where $\mathbf{F}^y$ is the northward (y) component of the dissipation term $\mathbf{F}$. We decompose the integrands in (D.2) into a lateral harmonic term and a term resulting from the divergence of the frictional stress, in order to isolate the effect of lateral and vertical boundary walls *i.e.* $\mathbf{F} = \mathbf{F}_h + \mathbf{F}_v = A_{_H} \nabla^2 \mathbf{u}_h + \partial_z \left(A_{_V} \partial_z \mathbf{u}_h \right)$, where $A_{_H}$ and $A_{_V}$ are the coefficients of horizontal and vertical viscous momentum dissipation respectively. With this, the horizontal and vertical dissipative contributions to the integral terms in (D.2) are

$$\int_{z=-h(y)}^{z=\eta} \overline{b_z \mathbf{F}_h^y} dz = H < \overline{N^2 \mathbf{F}_h^y} > \tag{D.3}$$

and

$$\int_{z=-h(y)}^{z=\eta} \overline{b_z \mathbf{F}_v^y} dz = \rho_0^{-1} \left(\overline{N^2 \tau^y} \right) \Big|_{z=-h(y)}^{z=0} - H < \overline{A_v v_z N_z^2} > \tag{D.4}$$

where we have used $\tau_b^y = \rho_0 (A_v v_z)$ at top and bottom boundaries. With this, the *net lateral dissipative flux of potential vorticity* is

$$\Delta_x \overline{J}_{NA} = \overline{J}_{NA_1} + \overline{J}_{NA_2} + \overline{J}_{NA_3} + \overline{J}_{NA_4} \tag{D.5}$$

where

$$\overline{J}_{NA_1} = \int_0^M H \left[(<\overline{N^2 \mathbf{F}_h^y}>)\big|_{x=L} - (<\overline{N^2 \mathbf{F}_h^y}>)\big|_{x=0} \right] dy \tag{D.6}$$

$$\overline{J}_{NA_2} = \int_0^M \left[\frac{(\overline{N^2 \tau^y})|_{x=L}}{\rho_0} - \frac{(\overline{N^2 \tau^y})|_{x=0}}{\rho_0} \right]_{z=0} dy \tag{D.7}$$

$$\overline{J}_{NA_3} = -\int_0^M \left[\frac{(\overline{N^2 \tau^y})|_{x=L}}{\rho_0} - \frac{(\overline{N^2 \tau^y})|_{x=0}}{\rho_0} \right]_{z=-h} dy \tag{D.8}$$

$$\overline{J}_{NA_4} = -\int_0^M H \left[< \overline{A_v v_z N_z^2} > \big|_{x=L} - < \overline{A_v v_z N_z^2} > \big|_{x=0} \right] dy \tag{D.9}$$

$\overline{J}_{NA_1}$ is associated with lateral (viscous) momentum dissipation, a contribution that becomes dominant in the presence of lateral boundary currents and strong vertical stratification. $\overline{J}_{NA_2}$ and $\overline{J}_{NA_3}$ are associated with surface wind stress and bottom frictional stress respectively, with non-vanishing contributions when these have non-zero (surface/bottom) curl, whereas the $\overline{J}_{NA_4}$ is associated with curvature in the vertical stratification.

As with the transport streamfunction, a trivial solution to (D.1) for a stratified flow past finite amplitude topography is that when each integral term vanishes, implying an equal amount of PV being fluxed into and out of the control volume. In the expression for net lateral PV fluxes, bottom topography does not appear explicitly, and thus the vanishing of each integral does not require the integrand to behave in any particular way as a function of distance from the ridge crest (in contrast with integral balances in 3.9). Nonetheless, the dissipative effects associated with lateral boundary currents will be localized to sloping bottom.

A resulting flow to consider is that in which the right hand side of (D.1) is zero, meaning the net circulation can be described by lateral PV integral balances, just as in Yang and Price ((2000)). This is the case of steady flow with vanishing *Net Topographic PV Flux*, and is equivalent to restricting bottom topography to play the passive role of promoting horizontal divergence.

VITA